



**Universidade do Minho**  
Escola de Engenharia

Sara Isabel Couto Cortez

**Procedures for Finite Element Mesh  
Generation from Medical Imaging.  
Application to the Intervertebral Disc**

Dissertação de Mestrado  
Ciclo de Estudos Integrados Conducentes ao  
Grau de Mestre em Engenharia Biomédica

Trabalho realizado sob a orientação de  
**Doutor José Luís Carvalho Martins Alves**  
**Universidade do Minho**

Outubro de 2011

## DECLARAÇÃO

Nome: Sara Isabel Couto Cortez

Endereço eletrónico: [a49951@alunos.uminho.pt](mailto:a49951@alunos.uminho.pt) Telefone: 00351 964 747 658

Número do Bilhete de Identidade: 13399554

Título da dissertação: Procedures for Finite Element Mesh Generation from Medical Imaging.  
Application to the Intervertebral Disc.

Ano de conclusão: 2011

Orientador: Professor Doutor José Luis Carvalho Martins Alves

Designação do Mestrado: Ciclo de Estudos Integrados Conducentes ao Grau de Mestre em  
Engenharia Biomédica

Área de Especialização: Biomateriais, Reabilitação e Biomecânica

Escola: de Engenharia

Departamento: de Engenharia Mecânica

DE ACORDO COM A LEGISLAÇÃO EM VIGOR, NÃO É PERMITIDA A REPRODUÇÃO DE QUALQUER  
PARTE DESTA TESE/TRABALHO.

Guimarães, \_\_\_\_/\_\_\_\_/\_\_\_\_\_

Assinatura: \_\_\_\_\_

## Acknowledgments

Firstly, I would like to thank my mentor Professor José Luis Alves, for his availability, knowledge, experience, constant support, timely guidance and suggestions throughout this project. His words made me grow professionally.

I am grateful to Professor J.C. Pimenta Claro for his support.

I would also like to express my sincere gratitude to Manuel Pinheiro, for all the support and encouragement throughout this work.

I gratefully acknowledge the support of the European Project: *NP Mimetic - Biomimetic Nano-Fiber Based Nucleus Pulposus Regeneration for the Treatment of Degenerative Disc Disease*, funded by the European Commission under FP7 (grant NMP3-SL-2010-246351).

I am grateful to CT2M - Centre for Mechanical and Materials Technologies, to Mechanical Engineering Department and to University of Minho, as well as to all their collaborators, for sponsoring my research and providing an excellent work environment.

I would like to thank all my friends, especially to Sara Tribuzi, Maria Martins and Ravi Patel for their unconditional help.

Finally, I would like to thank to my parents, my brother and Diogo for their continued support and guidance and for believing in my capabilities.

Sara Cortez



## **Abstract**

### **Procedures for Finite Element Mesh Generation from Medical Imaging. Application to the Intervertebral Disc.**

The paramount goal of this ‘half-year’ work is the development of a set of methodologies and procedures for the geometric modelling by a finite element (FE) mesh of the bio-structure of a motion segment (or functional spinal unit), i.e., two vertebrae and an intervertebral disc, from segmented medical images (processed from medical imaging).

At an initial stage, a three-dimensional voxel-based geometric model of a goat motion segment was created from magnetic resonance imaging (MRI) data. An imaging processing software (ScanIP/Simplewire) was used for imaging segmentation (identification of different structures and tissues), both in images with lower (normal MRI) and higher (micro-MRI) resolutions. It shall be noticed that some soft-tissues, such as annulus fibrosus or nucleus pulposus, are very hard to isolate and identify given that the interface between them is not clearly defined. At the end of this stage, images with different resolutions allowed to generate different 3D voxel-based geometric models.

Thereafter, a procedure for the FE mesh generation from the aforementioned voxelized data should be studied and applied. However, as the original geometry was only approximately known from real medical imaging, it was difficult to objectively quantify the quality of the FE meshing procedure and the accuracy between source geometry and target FE mesh. In order to overcome such difficulties, and due to the lack of quality of the available medical imaging, a “virtualization” procedure was developed to create a set of segmented 2D medical images from a well-defined geometry of a motion segment. The main idea was to create the conditions to quantify the quality and the accuracy of the developed FE meshing procedure, as well to study the effect of imaging resolution.

Starting from the virtually generated 2D segmented images, a 3D voxel-based structure was achieved. Given that initial domains are now clearly defined, there is no need for further image processing. Then, a two-step FE mesh generation procedure (generation followed by simplification) allows to create an optimized tetrahedral FE mesh directly from 3D voxelized data. Finally, because the virtualization procedure allowed to know the initial geometry, one is able to objectively quantify

the quality and the accuracy of the final simplified tetrahedral FE mesh, and thus to understand and quantify: a) the role of the medical image resolution on the FE geometrical reconstruction, b) the procedure and parameters of the FE mesh generation step, and c) the procedure and parameters of the FE mesh simplification step, and thus to give a clear contribution in the definition of the procedure for the FE mesh generation from medical imaging in case of an intervertebral disc.

## Resumo

### **Procedimentos de Geração de Malha de Elementos Finitos a partir de Imagem Médica. Aplicação ao Disco Intervertebral.**

O objetivo fundamental deste trabalho de seis meses é o desenvolvimento de um conjunto de metodologias e procedimentos para a modelação geométrica, através de uma malha de elementos finitos (EF) de uma bio-estrutura de um *motion segment* (ou unidade funcional da coluna), ou seja, duas vértebras e um disco intervertebral, a partir de imagens médicas segmentadas (processadas a partir de imagiologia médica).

Numa fase inicial, um modelo geométrico tridimensional baseado em voxels de um *motion segment* de uma cabra foi criado a partir de informação de imagens médicas de ressonância magnética (RM). Um *software* de processamento de imagem (*ScanIp/Simplewire*) foi usado para segmentação de imagens (identificação de diferentes estruturas e tecidos), em imagens de menor (RM normal) e maior (micro-RM) resolução. Deve ser referido que alguns tecidos moles, como o anel fibroso e o núcleo pulposo são muito difíceis de isolar e identificar, dado que as fronteiras destes não estão claramente definidas. No final desta etapa, as imagens com diferentes resoluções permitiram gerar diferentes modelos geométricos 3D baseados em voxels.

Posteriormente, um procedimento para geração de malha de EF, a partir da informação voxelizada acima mencionada, deveria ser estudado e aplicado. No entanto, como a geometria original era aproximadamente conhecida a partir de imagens médicas reais, foi difícil quantificar objetivamente a qualidade do procedimento de geração de malha de EF e a precisão entre a geometria de origem e a malha de EF de destino. A fim de superar tais dificuldades, e devido à falta de qualidade de imagens médicas disponíveis, um procedimento de “virtualização” foi desenvolvido para criar um conjunto de imagens médicas 2D segmentadas a partir de uma geometria de um *motion segment* bem conhecida. A principal ideia foi criar as condições para quantificar a qualidade e a precisão do procedimento de geração de malha de EF desenvolvido, bem como estudar o efeito da resolução da imagem médica.

A partir das imagens 2D segmentadas, geradas virtualmente, uma estrutura de voxels 3D pode ser conseguida. Dado que os domínios iniciais estão agora claramente definidos, não há necessidade de processamento de imagem adicional. Por conseguinte, um procedimento de

geração de malha de EF de duas etapas (geração seguida por simplificação) permite criar uma malha de EF tetraédrica otimizada diretamente a partir de informação 3D voxelizada.

Por fim, como o procedimento de virtualização permitiu conhecer a geometria inicial, é possível quantificar objetivamente a qualidade e exatidão da malha de EF tetraédrica final simplificada, e assim, compreender e quantificar: a) o papel da resolução da imagem médica na reconstrução geométrica de EF; b) o procedimento e os parâmetros da etapa de geração de malha de EF; c) o procedimento e os parâmetros da etapa de simplificação de malhas de EF, e assim, dar uma contribuição clara na definição do procedimento para a geração de malha de EF a partir de imagem médica, no caso de um disco intervertebral.



# Contents

Acknowledgments .....	iii
Abstract.....	v
Resumo .....	vii
Contents .....	ix
Acronyms .....	xi
List of Figures .....	xiii
List of Tables .....	xvii
Chapter 1. Introduction .....	1
1.1. Motivation and Scope.....	1
1.2. Aim .....	5
1.3. Limitation of the study .....	6
1.4. Organization of thesis .....	6
Chapter 2. The Human spine system.....	9
2.1. Anatomy.....	9
2.2. Intervertebral disc.....	11
2.2.1. Nucleus Pulposus .....	13
2.2.2. Annulus Fibrosus .....	13
2.2.3. Cartilaginous Endplate .....	14
2.3 Biomechanics and degenerative diseases of the IVD.....	14
Chapter 3. Medical Image Techniques.....	17
3.1. Introduction .....	17
3.1.1. Plain radiography.....	17
3.1.2. X-ray computed tomography.....	19
3.1.2.1. Micro-computed tomography .....	22
3.1.3. Magnetic Resonance Image.....	22
3.1.4. Other medical image techniques .....	24
3.2. Comparison of medical image resolution.....	24
Chapter 4. Three-dimensional reconstruction from medical imaging.....	27
4.1. Introduction .....	27
4.2. 3D reconstruction of a real goat motion segment.....	29

4.3. Segmentation Algorithms .....	30
4.3.1. Thresholding .....	31
4.3.2. Clustering methods .....	36
4.3.3. Deformable model-based methods.....	38
4.4. Case Study: segmentation of a goat intervertebral disc.....	39
4.5. Scheme of the segmentation procedure of an IVD.....	41
Chapter 5. Finite Element Mesh Generation .....	43
5.1. Introduction .....	43
5.2. Procedure for Virtual Voxel-based Model Generation.....	44
5.2.1. Voxel ID searching algorithm.....	47
5.2.2. Voxel's Dimensions .....	50
5.2.3. Analysis and Validation Tests.....	51
5.3. Mesh Generation Procedure .....	57
5.3.1. Analysis and Validation Tests.....	61
Chapter 6. Finite Element Mesh Simplification .....	79
6.1. Absolute/relative edge sizing.....	85
Chapter 7. Conclusion .....	91
Chapter 8. Future Work .....	95
References.....	97
Appendix A.....	101
A.1. Newton-Raphson Method .....	101

## **Acronyms**

2D – two-dimensional

3D – three-dimensional

AF – annulus fibrosus

BCC – body-centred cubic lattice

CEP – cartilaginous endplate

CT – X-ray computed tomography

DICOM - Digital Imaging and Communications in Medicine

DDD – degenerative disc disease

FE – finite element

FEA – finite element analysis

FOV – field of view

HU – Hounsfield units

IVD – intervertebral disc

NP – nucleus pulposus

MRI – magnetic resonance image

ROI – region of interest



## List of Figures

Figure 2.1 – The Human spine.....	9
Figure 2.2 – The vertebral structure [Daavittila, 2007].....	10
Figure 2.3 – The motion segment consisting of two vertebral bodies and a normal IVD between them [adapted from [Raj, 2008].....	12
Figure 2.4 - The components of the intervertebral disc (adapted from [Postacchini, 1999]).....	12
Figure 2.5 – Mid-sagittal sections of intervertebral discs showing the biochemical appearance of ageing (A) a disc typical of ages 20–30 years and (B) a disc typical of ages 50–60 years [Adams <i>et al.</i> , 2010].....	15
Figure 2.6 – Compression loading (A) a normal non-degenerated and (C) degenerated disc. Outer annulus layers have a large tension stress along the fibres and also in the tangential peripheral direction. The inner annulus fibres have stresses of smaller magnitude (B). Annulus fibres show outer layers are subjected to increased amount of tensile stress. The inner annulus fibres have a high compressive stress (D) [Jensen, 1980]. .....	15
Figure 3.1 – Plain radiographs showing the following: (A) Narrowing of the L5-S1 disc space with mild osteophyte formation demonstrating mild DDD at this single level. (B) Disc space narrowing, endplate sclerosis, and osteophytes at L1-L2, L2-L3, L4-L5, and L5-S1 in this patient with marked multi-level DDD. Retrolisthesis of L3 on L4 is also seen [Wills <i>et al.</i> , 2007]. .....	18
Figure 3.2 – Principle of the plain radiography technique (adapted from [Butler <i>et al.</i> , 2007]) .....	18
Figure 3.3 – CT scan showing complete loss of the L5-S1 disc space with severe endplate sclerosis and development of osteophytes. [Wills <i>et al.</i> , 2007]. .....	19
Figure 3.4 – Principle of different generations of CT scanner. First (A), Second (B), Third (C), Fourth (D) and modern (E) generation scanner (adapted from [Zeng, 2010]).....	20
Figure 3.5 – The principle of attenuation. ....	21
Figure 3.6 – The tiny bar magnets (A) before and (B) after the tissues being placed within a strong magnetic field. ....	23
Figure 3.7 – T1-weighted (A) and T2-weighted (B) sagittal MRI demonstrating a disc herniation at L4-L5 [Wills <i>et al.</i> , 2007]......	23
Figure 4.1– The pixel and the voxel representation. ....	28
Figure 4.2 – The three main imaging plans of the human body: sagittal (YZ), coronal (XZ) and axial (XY) (adapted from [Dougherty, 2009])......	29

Figure 4.3 – The (A) MR and (B) micro-MR images of the lumbar goat motion segment in different planes (sagittal, axial and coronal, respectively). .....	29
Figure 4.4 – The thresholding algorithm applied to the (A) MR and (B) micro-MR images.....	33
Figure 4.5 – The gradient magnitude filter applied to the (A) MR and (B) micro-MR images.....	34
Figure 4.6 – The Canny Operator applied to the (A) MR and (B) micro-MR images after thresholding.....	35
Figure 4.7 – The region growing algorithm applied to the (A) MR and (B) micro-MR images. ....	36
Figure 4.8 – The segmentation of the IVD with the geodesic active contour applied to the (A) MR and (B) micro-MR images. ....	39
Figure 4.9 – Two different 3D models based on (A) 0.3x0.3x3.3 mm <sup>3</sup> and (B) 0.12x0.12x0.12 mm <sup>3</sup> of MR image resolution.....	39
Figure 4.10 – Two examples of micro-MR images of the IVD converted into colour images.....	40
Figure 4.11 – Data flow diagram of the segmentation procedure applied to a motion segment based on micro-MR images. ....	41
Figure 5.1 – Reference FE mesh of the human lumbar motion segment (from the ISB Finite Element Repository). ....	45
Figure 5.2 - - A two-dimensional illustration of the (three-dimensional) creation of the grid of pixels (voxels). ....	46
Figure 5.3 – Schematic representation of the equivalence between Cartesian and canonical spaces of a given finite element. ....	47
Figure 5.4 – Example of a 8-node hexahedron drawn in the canonical frame.....	47
Figure 5.5 – Schematic of the virtual segmentation process on the pixels matrix. ....	49
Figure 5.6 – Schematic of three different dimensions of pixels.....	50
Figure 5.7 – Sagittal sectioning (X=2) of the motion segment with a) 0.3x0.3x3.3 b) 0.12x0.12x0.12 and c) 0.3x0.3x0.3 mm <sup>3</sup> of the voxel size. ....	52
Figure 5.8 - Coronal sectioning (Y=2) of the motion segment with a) 0.3x0.3x3.3 b) 0.12x0.12x0.12 and c) 0.3x0.3x0.3 mm <sup>3</sup> of the voxel size. ....	53
Figure 5.9 - Axial sectioning (Z= -5) of the motion segment with a) 0.3x0.3x3.3 b) 0.12x0.12x0.12 and c) 0.3x0.3x0.3 mm <sup>3</sup> of the voxel size.....	54
Figure 5.10 - Axial sectioning (Z=0) of the motion segment with a) 0.3x0.3x3.3 b) 0.12x0.12x0.12 and c) 0.3x0.3x0.3 mm <sup>3</sup> of the voxel size.....	55
Figure 5.11 – Schematic of the mesh generation parameters.....	59

Figure 5.12 – A two-dimensional illustration of the (three-dimensional) FE mesh generation algorithm.....	60
Figure 5.13 – Sagittal cross section ( $X=2.0$ mm) of the initial geometry (coloured domains) and the contour of the FE mesh for the resolution of $0.3 \times 0.3 \times 3.3$ mm <sup>3</sup> . The parameters used were a grid size of 2.0 mm (and $N$ of 1.04) and $\sigma$ of a) 0.52 b) 1.04 c) 2.08.....	62
Figure 5.14 - Sagittal cross section ( $X=2.0$ mm) of the initial geometry (coloured domains) and the contour of the FE mesh for the resolution of $0.12 \times 0.12 \times 0.12$ mm <sup>3</sup> . The parameters used were a grid size of 2.0 mm (and $N$ of 16.67) and $\sigma$ of a) 8.33 b) 16.67 c) 33.33. ....	63
Figure 5.15 – Sagittal cross section ( $X=2.0$ mm) of the initial geometry (coloured domains) and the contour of the FE mesh for the resolution of $0.3 \times 0.3 \times 0.3$ mm <sup>3</sup> . The parameters used were a grid size of 2.0 mm (and $N$ of 6.67) and $\sigma$ of a) 3.33 b) 6.67 c) 13.33.....	64
Figure 5.16 – Sagittal cross section ( $X=2.0$ mm) of the initial geometry (coloured domains) and the contour of the FE mesh for the resolution of $0.3 \times 0.3 \times 3.3$ mm <sup>3</sup> . The parameters used were a grid size of 1.0 mm (and $N$ of 0.52) and $\sigma$ of a) 0.26 b) 0.52 c) 1.04.....	65
Figure 5.17 - Sagittal cross section ( $X=2.0$ mm) of the initial geometry (coloured domains) and the contour of the FE mesh for the resolution of $0.12 \times 0.12 \times 0.12$ mm <sup>3</sup> . The parameters used were a grid size of 1.0 mm (and $N$ of 8.33) and $\sigma$ of a) 4.17 b) 8.33 c) 16.67.....	66
Figure 5.18 – Sagittal cross section ( $X=2.0$ mm) of the initial geometry (coloured domains) and the contour of the FE mesh for the resolution of $0.3 \times 0.3 \times 0.3$ mm <sup>3</sup> . The parameters used were a grid size of 1.0 mm (and $N$ of 3.33) and $\sigma$ of a) 1.67 b) 3.33 c) 6.67.....	67
Figure 5.19 – Sagittal cross section ( $X=2.0$ mm) of the initial geometry (coloured domains) and the contour of the FE mesh for the resolution of $0.3 \times 0.3 \times 0.3$ mm <sup>3</sup> . The parameters used were a grid size of 0.5 mm (and $N$ of 0.26) and $\sigma$ of a) 0.26 b) 0.52.....	68
Figure 5.20 – Sagittal cross section ( $X=2.0$ mm) of the initial geometry (coloured domains) and the contour of the FE mesh for the resolution of $0.12 \times 0.12 \times 0.12$ mm <sup>3</sup> . The parameters used were a grid size of 0.5 mm (and $N$ of 4.17) and $\sigma$ of a) 2.08 b) 4.17 c) 8.33. ....	69
Figure 5.21 – Sagittal cross section ( $X=2.0$ mm) of the initial geometry (coloured domains) and the contour of the FE mesh for the resolution of $0.3 \times 0.3 \times 0.3$ mm <sup>3</sup> . The parameters used were a grid size of 0.5 mm (and $N$ of 1.67) and $\sigma$ of a) 0.83 b) 1.67 c) 3.33.....	70
Figure 5.22 – FE mesh obtained for the resolution of $0.3 \times 0.3 \times 3.3$ mm <sup>3</sup> , grid size of 0.5 mm and $\sigma$ value of 0.52. ....	74

Figure 5.23 - FE mesh obtained for the resolution of 0.12x0.12x0.12 mm <sup>3</sup> , grid size of 0.5 mm and $\sigma$ value of 8.33.....	74
Figure 5.24 - FE mesh obtained for the resolution of 0.3x0.3x0.3 mm <sup>3</sup> , grid size of 0.5 mm and $\sigma$ value of 3.33.....	74
Figure 6.1 – FE mesh simplification by edge contraction.....	79
Figure 6.2 - Sagittal sectioning (X=2) of the FE mesh based on the resolution of 0.12x0.12x0.12 mm <sup>3</sup> for a) simplification 1: 100 000; b) simplification 2: [-t0.05] 100 000; c) simplification 3: [-t0.05] [-g] 100 000.....	82
Figure 6.3 - Sagittal sectioning (X=2) of the FE mesh based on the resolution of 0.3x0.3x0.3 mm <sup>3</sup> for a) simplification 1: 100 000; b) simplification 2: [-t0.05] 100 000; c) simplification 3: [-t0.05] [-g] 100 000.....	83
Figure 6.4 - FE mesh obtained based on simplification 2 from voxel size of 0.12x0.12x0.12 mm <sup>3</sup> with sizing parameters of (left) 0.5 and 10 (right) 1.0 and 10 for max edge length inside the IVD and max edge length outside the IVD, respectively.....	86
Figure 6.5 - FE mesh obtained based on simplification 2 from voxel size of 0.3x0.3x0.3 mm <sup>3</sup> with sizing parameters of (left) 0.5 and 10 (right) 1.0 and 10 for max edge length inside the IVD and max edge length outside the IVD, respectively.....	86
Figure 6.6 - Sagittal sectioning (X=2) of the FE mesh based on simplification 2 from voxel size of 0.12x0.12x0.12 mm <sup>3</sup> for a) 0.5 and 10 b) 1.0 and 10 of the edge length in IVD and edge length outside of the IVD, respectively.....	87
Figure 6.7 –Sagittal sectioning (X=2) of the FE mesh based on simplification 2 from voxel size of 0.3x0.3x0.3 mm <sup>3</sup> for a) 0.5 and 10 b) 1.0 and 10 of the edge length.....	88
Figure 6.8 – Meshes from simplification with relative sizing of 1:20 (upper mesh) and 1:10 (lower mesh).....	90
Figure 7.1 - Proposed FE mesh generation procedure developed in this study.....	93
Figure 8.1 – Characterization of the porcine lumbar motion segment using a destructive serial-sectioning technique.....	95
Figure A.1 - A geometric interpretation of the Newton-Raphson method.....	101



## List of Tables

Table 1.1 – Summary of the most relevant publications about FE mesh generation of a motion segment. ....	2
Table 3.1 – Resolution and some characteristics of images from different medical imaging techniques.....	25
Table 4.1 – Comparison between the two types of MRI images used in this work. ....	30
Table 5.1 – Three different resolutions (voxel's dimension) of the voxel used in this study. ....	50
Table 5.2 – Number of elements and volumes of the voxel and the initial geometry of different materials with 0.3x0.3x0.3 mm <sup>3</sup> of the voxel dimension. ....	56
Table 5.3 - Number of elements and volumes of the voxel and the initial geometry of different materials with 0.12x0.12x0.12 mm <sup>3</sup> of the voxel dimension. ....	56
Table 5.4 - Number of elements and volumes of the voxel and the initial mesh for different materials with 0.3x0.3x0.3 mm <sup>3</sup> of the voxel dimension. ....	56
Table 5.5 – Different parameters used in FE mesh generation. ....	58
Table 5.6 – Volumes of the different materials of the generated FE meshes with a voxel dimension of 0.3x0.3x0.3 mm <sup>3</sup> . ....	71
Table 5.7 – Volumes of the different materials of the final FE mesh with a voxel dimension of 0.12x0.12x0.12 mm <sup>3</sup> . ....	72
Table 5.8 – Volumes of the different materials of the final FE mesh with a voxel dimension of 0.3x0.3x0.3 mm <sup>3</sup> . ....	73
Table 6.1 – Description of the different refinement criteria of the mesh simplification procedures. ....	80
Table 6.2 – Simplification case studies.....	81
Table 6.3 – Number of nodes and elements and the dihedral angles for different simplification tests. ....	84
Table 6.4 – Sizing tests performed with absolute parameter. ....	85
Table 6.5 - Number of elements and nodes and the dihedral angles for different simplification tests with two different edges length. ....	88
Table 6.6 – Sizing tests performed with relative parameter for a non-simplified mesh.....	89



---

# Chapter 1. Introduction

---

## 1.1. Motivation and Scope

The Degenerative Disc Diseases (DDD) is a relatively common problem of the spine, particularly in the lumbar region [Rannou *et al.*, 2001]. The low back pain is an important disease pertaining to human health as it may limit mobility and affect normal functions of the spine. Its incidence tends to increase every year and to affect a large portion of the population [Urban *et al.*, 2003]. Biomechanics and several biomechanical tests and studies have given essential contributions to find the causes and solutions for this problem.

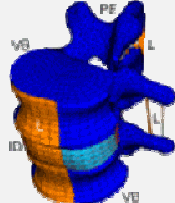
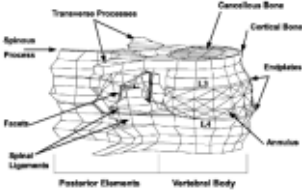
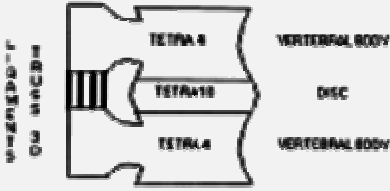
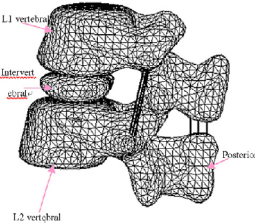
The Finite Element Analysis (FEA) is an essential tool to study the behaviour of the spine, especially to investigate the bio-mechanisms of the intervertebral disc (IVD). The benefits of using FEA in biomechanical studies are obvious and this method has definitely contributed to improve our understanding on the biomechanics of the spine. In most cases biological structures are not easy to study *in vivo*, and only computational models and numerical simulations are easily accessible allowing to have an “inside” view. IVDs are no exception, as they are hardly accessible. Around the world, research groups have devoted attention to this subject and have applied FE modelling to study the biomechanics of the IVD.

Virtual 3D models, such as 3D FE meshed, can be used to “virtualize” the internal structures of the Human body, and thus contributing to medical diagnosis of pathologies; to decide rehabilitation strategies; to virtualize surgeries and *a priori* evaluation of surgical strategies. However, the 3D reconstruction process of a patient-oriented data is somewhat tricky and is known to have some problems that cause a number of difficulties in the FE analysis, such as the identification of tiny or too complex geometric details. The accuracy of the FE computation increases if the geometry of model resembles the real structure.

In general, a FE model can be created from a solid voxel-based 3D model obtained from 3D reconstruction of a set of 2D medical images. Medical images are usually obtained from any

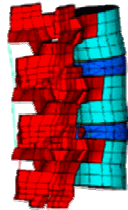
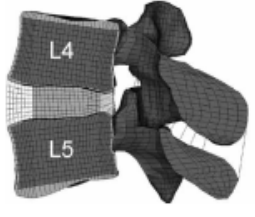

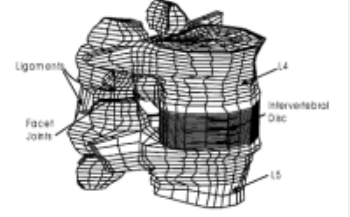
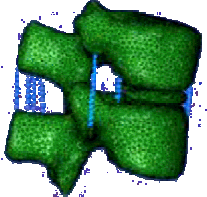
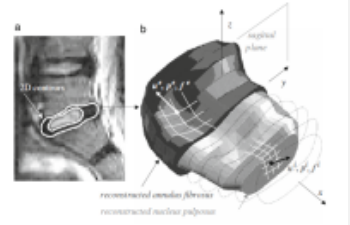
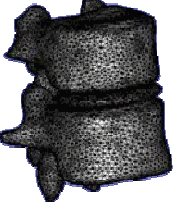
medical imaging technique, such as radiography, X-Ray Computer Tomography (CT), Magnetic Resonance Imaging (MRI), or other. In fact, most of these models are based on CT images, MRI images or a combination of CT and MRI images and some of them are even created by algorithms using “standard” dimensions mentioned in literature [Tyndyka *et al.*, 2007]. Table 1.1 shows some of the most relevant 3D models of a motion segment based on different protocols and data, as was found in literature.

**Table 1.1 – Summary of the most relevant publications about FE mesh generation of a motion segment.**

Authors, Year	Image Data	Motion Segment	Model Representation
<b>[Kakol <i>et al.</i>, 2003]</b>	NMR <sup>1</sup> and CT images	L4 - L5	
<b>[Natarajan <i>et al.</i>, 2003]</b>	CT images	L3 – L4	 <p data-bbox="1026 1294 1313 1312">Fig. 1. Finite element model of a L3-L4 motion segment.</p>
<b>[Wong <i>et al.</i>, 2003]</b>	CT images (Slice thickness: 1 mm; Pixel size: 0.33 mm)	L4 – L5	
<b>[Li <i>et al.</i>, 2006]</b>	CT images (Slice thickness: 0.8 mm; Pixel size: 0.33 mm)	L1 – L2	

<sup>1</sup> NMR - nuclear magnetic resonance

(continued) Table 1.1 - The studies of the 3D motion segment models.

<b>[Zhong <i>et al.</i>, 2006]</b>	CT images	L1 – L3	
<b>[Schmidt <i>et al.</i>, 2007]</b>	CT images (Slice thickness: 0.75 mm; Pixel size: 0.49 mm) and MRI images	L4 – L5	
<b>[Renner <i>et al.</i>, 2007]</b>	CT images	L1 – S1	
<b>[Natarajan <i>et al.</i>, 2007]</b>	CT images	L4 – L5	
<b>[Meng <i>et al.</i>, 2009]</b>	CT images (Slice thickness: 1 mm)	L4 – L5	
<b>[Swider <i>et al.</i>, 2010]</b>	MRI images	L5 – S1	
<b>[Bao <i>et al.</i>, 2010]</b>	CT images (Slice thickness: 0.75 mm)	L1 – L2	

Despite all 3D models are based on specific and real data (essentially CT), significantly different geometries can be seen. Such big differences when dealing with similar real structures reveal basically the lack of robustness of the 3D reconstruction process, and not simply real differences on medical images and/or anatomical information and histological observations. However, it is also known that both the type of medical imaging technique and image resolution have a key role in the 3D reconstruction process. Sometimes these geometrically-based models do not provide complete information about the different structures due to the low resolution of most medical images, i.e., very tiny details and tiny structures are very probably lost “inside” resolution. On the other hand, some soft tissues of IVD, especially nucleus pulposus and annulus fibrosus, have similar density and constitution, what makes 3D reconstruction even more difficult and imaging segmentation a very user-dependent task. CT images has proved to be a good tool to aid in the segmentation of bone structures but turned out to be less efficient than MRI images in the detection of soft tissues such as the ones in the intervertebral disc.

The resolution of medical images, i.e., pixel size and slice thickness, plays also an important role in the accuracy of 3D geometrical reconstruction of anatomical structures from 2D images, and consequently of final FE meshes. Resolution provides information regarding which technique can or shall not be used for 3D reconstruction. The aim of this work is to establish an optimized procedure for the generation of a 3D FE mesh of a motion segment in general, and an intervertebral disc in particular, in order to allow the development of new biomechanical simulations of intervertebral discs. It will be shown that the original imaging resolution plays a paramount role on the quality and accuracy of the generated FE meshes. Besides, such requirements for the biomechanical studies can drive the specifications for future improved medical imaging equipments.

Although a multi-segment FE model have many advantages and have contributed significantly to quantify the biomechanics of the spine, in this work, a motion segment (L4 – L5) FE mesh originally created by T.H. Smit (available on the web from the ISB Finite Element Repository<sup>2</sup>) was re-worked and used as a reference geometry to allow an objective comparison with the final FE meshes obtained from the newly proposed FE mesh generation procedure.

---

<sup>2</sup>(available at <http://biomch-l.isbweb.org/forum.php>, last consulted on April 2011)

## 1.2. Aim

The paramount goal of this study is the development of a set of methodologies and procedures for the 3D geometrical/anatomical modelling by a finite element mesh of the bio-structure of a motion segment, i.e., two vertebrae and an intervertebral disc, from images acquired by any medical imaging technique. A simplified and optimized finite element mesh must be generated in order to couple the patient-oriented data acquisition from medical imaging with computational FEA of the biomechanics of the human spine.

To investigate the influence of medical imaging resolution on the final quality of the generated geometric model by finite elements, an algorithm for the generation of a set of 2D virtual and segmented medical images is developed and implemented. Then, a procedure allowing the generation of a tetrahedral FE mesh from 3D reconstructed and segmented medical imaging is applied. The main purpose behind the abovementioned idea is to allow establishing some objective criteria for the evaluation and quantification of the impact of the reconstruction parameters and FE mesh generation procedure by comparing objectively the final geometrical reconstruction by finite elements and the well-defined and initial geometry of a lumbar motion segment, in order to understand the role of the medical image resolution and FE mesh generation procedure and parameters on the geometrical reconstruction by finite elements from medical imaging data.

In summary, once the 2D image scanning data of an intervertebral motion segment are obtained, one shall be able to:

- a) produce a 3D voxel-based model from the 2D medical images;
- b) study the influence of the medical imaging parameters (resolution, segmentation, etc.) over the FE meshing technique of a lumbar motion segment;
- c) generate a good quality and optimized finite element mesh, with a special emphasis on an accurate modelling of the biological and anatomical features and surrounding tissues and bones of a motion segment in general, and the intervertebral disc in particular.

This study is framed under an on-going European project denominated “***NPmimetic - Biomimetic Nano-Fibre-Based Nucleus Pulposus Regeneration for the Treatment of Degenerative Disc Disease***”, which seeks to develop a biomimetic strategy for the IVD regeneration. Under this framework, the primary goal of the present study is to develop a procedure to obtain a simplified and optimized FE mesh describing geometrically a patient-oriented

intervertebral motion segment based on medical images, which can be used for future computational analysis of the biomechanics of the IVD, numerical analysis of the rehabilitation procedures and specification of the mimetic materials to be developed.

### **1.3. Limitation of the study**

The primary idea behind this work was to use real medical imaging data, which should be processed and segmented in order to allow a 3D geometrical reconstruction. These 3D voxel-based geometric models should be hereafter used for the FE mesh generation in order to obtain the final 3D geometrical reconstruction by finite elements. However, some obstacles appeared along this way, which made mandatory to update the initially proposed flowchart. In brief, the most common problems were the lack of resolution of the medical images, the ambiguous definition of tissues' boundaries, what made difficult to isolate and identify soft tissues like annulus fibrosus or nucleus pulposus and thus to attain a reliable segmentation, and a clear and unambiguous identification of the reference geometry for comparison purposes. On the other hand, for very low resolution images it was hard to define the boundaries between two different anatomic regions with a similar density and constitution, and any user-decision could drive to a non-negligible variation of the initial geometry. Real images were not used to study the influence of resolution on the FE mesh generation procedure.

### **1.4. Organization of thesis**

Chapter 1 briefly presents the main framework of this thesis, main problems of the spine, the motivation, aims and some limitations faced during the development of this work.

Chapter 2 gives a brief description of the main features of the Human spine system and its constituents (in particular the IVD). It also provides a brief description of the biomechanics of the IVD and related degenerative disc diseases.

The main medical imaging techniques are briefly presented in Chapter 3. Only the most relevant techniques used in the diagnostic of degenerative diseases of the lumbar spine are detailed, such as plain radiography, computed tomography (CT), magnetic resonance imaging (MRI), micro-CT and micro-MRI.

Chapter 4 focuses on the procedures for three-dimensional reconstruction from medical imaging. 3D voxel-based geometrical models, obtained after denoising, smoothing and sampling of



2D medical images, are the starting point for FE mesh generation procedures. Thus, this Chapter addresses several questions such as 2D image properties, segmentation algorithms used for image processing and procedures for generation of the 3D voxel-based geometric model. The image resolution and its influence on accuracy geometric model are also discussed in this Chapter, and illustrated with the 3D reconstruction of a goat IVD from real medical imaging data.

In Chapter 5 the procedure for the FE mesh generation from 3D voxel-based geometric models is discussed. An algorithm for the construction of a set of virtual and segmented 2D images is introduced and described. Finally, the influence of each parameter of the mesh generation procedure on the final FE mesh is presented and discussed.

Chapter 6 presents a comparison between final geometry described by the optimized and simplified FE mesh and the initial geometry of the motion segment. Such comparison allows the definition of several quality criteria to classify the FE mesh generation procedure.

Finally, main conclusions and FE mesh generation guidelines are drawn in Chapter 7 whereas future work, which is already in development, is covered in chapter 8.



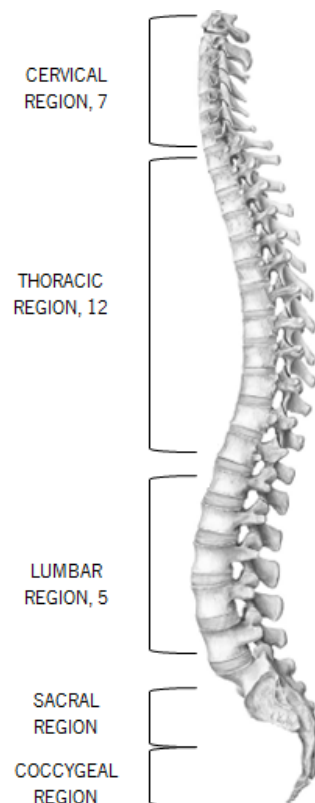
---

## Chapter 2. The Human spine system

---

### 2.1. Anatomy

The Human spine (or vertebral column) has some important functions such as: to provide the body structural support, to protect the spinal cord, nerve roots, and many internal organs, to enable trunk movements (e.g., flexion, extension, lateral bending, and axial rotation). These spine capabilities depend essentially of its constitution [Niosi *et al.*, 2004; Jongeneelen, 2006; Shankar *et al.*, 2009].

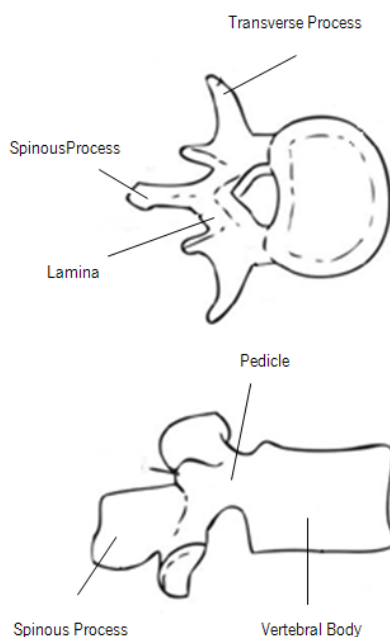


**Figure 2.1 – The Human spine.**

The spine is fundamentally composed of vertebral bodies and intervertebral discs. It extends from the base of the skull, passes through the neck, trunk and goes all the way to the

pelvis (Figure 2.1). The spine consists of 33 separated vertebrae: five of them are sacral vertebrae, which are fused to form the sacrum, and four are coccygeal vertebrae, which are fused to form the coccyx. In adult persons, there are 24 motion segments named according to their location in the intact column, seven cervical (C1 to C7), twelve thoracic (T1 to T12), five lumbar (L1 to L5) and ending with the sacral vertebrae (S1 to S5). One motion segment is composed of two vertebral bodies and one disc. The surfaces of the vertebral body are enclosed by a thin layer of hyaline cartilage, called endplates, and the nutrition of the intervertebral discs is done through these structures by diffusion process [Naegel, 2007; Shankar *et al.*, 2009].

The vertebra size varies along in spine, cervical being the smallest and lumbar the largest. Nevertheless, the basic structure of the vertebral body remains the same. Each vertebra consists of an anterior vertebral body and a posterior arch. The body is the thick zone of the vertebra composed of spongy medullary bone surrounded by a dense bony cortex. The neural arch has a pair of pedicles on its sides and two laminae. The laminae are broad flat plates of bone that are extended from the pedicles and, when they fuse with the lamina of the vertebra below, form the roof of the vertebral foramen, thus forming a canal to protect the spinal cord [Daavittila, 2007]. The vertebral arch also supports one spinous, two transverse and four articular processes. A spinous process is typically palpable through the skin. Superior and inferior articular facets on each vertebra act to restrict the vertebral column movement. Figure 2.2 shows the constitution of one vertebra.



**Figure 2.2 – The vertebral structure [Daavittila, 2007].**

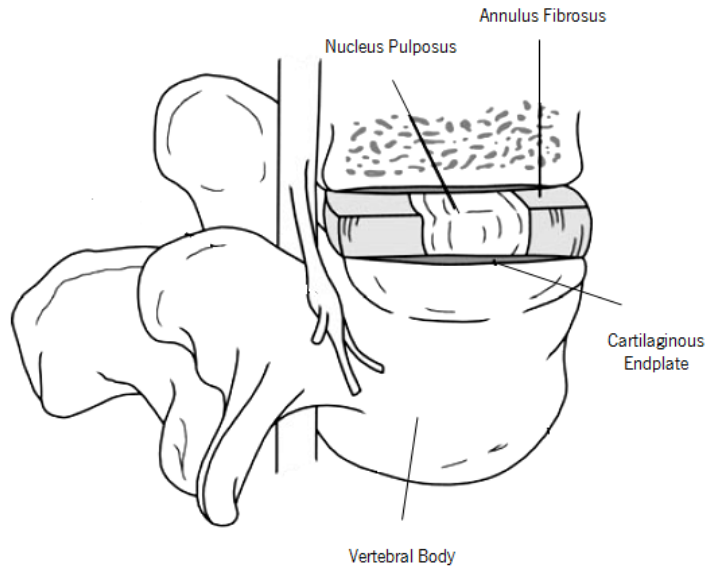
Furthermore, the vertebrae are also connected to each other by paired facet joints between the articular processes and by strong anterior and posterior longitudinal ligaments, which extend the length of the whole vertebral column and are attached to the intervertebral discs and vertebral bodies.

The anterior longitudinal ligament is a strong, broad fibrous band covering and connecting the anterior features of the vertebral bodies and intervertebral discs. Their fibres are firmly bound to the surface of the intervertebral discs, and the periosteum of the vertebral bodies is thickest on the front side of the discs. The posterior longitudinal ligament runs along the posterior side of the vertebral column within the vertebral canal. It has a characteristic appearance with extensions over to intervertebral discs, narrowing as it passes each vertebral body. The posterior longitudinal ligament narrows down caudally. Additionally, the flavum, supraspinous and interspinous ligaments can also help to stabilize the spine [Ebraheim *et al.*, 2004].

## **2.2. Intervertebral disc**

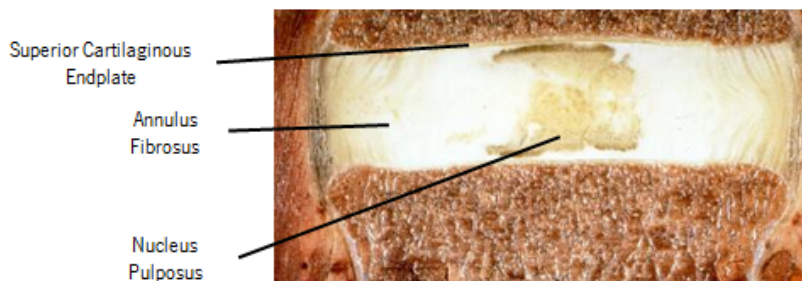
The intervertebral disc is a cartilaginous structure that contributes to flexibility and weight support in the spine. The IVDs are the most important structural links between adjacent vertebrae. They are exposed to a considerable variety of mechanical loadings (forces and moments), such as compressive loads arising from body weight and muscle activation, and connect one vertebral body to the next one [Urban *et al.*, 2000].

There are 23 intervertebral discs along the whole spine, and their heights differ between vertebrae (approximately 8-10 mm in height and 4 cm in diameter). In young persons, the IVDs between the bodies of sacral and coccygeal vertebrae are present but will eventually disappear while ageing [Raj, 2008]. Additionally, the IVD's height comprises approximately 25% of the total height of the vertebral column. The different curvatures of the spine, particularly in the cervical and lumbar region, are associated with the different height of the intervertebral disc (Figure 2.3). In the cervical region, the IVD geometry tends to be oval, while in the thoracic region it resembles a heart-like and in the lumbar region it looks like a kidney.



**Figure 2.3 – The motion segment consisting of two vertebral bodies and a normal IVD between them [adapted from [Raj, 2008].**

Each IVD is composed of an outer laminated and densely annulus fibrosus surrounding an inner gelatinous nucleus pulposus. Its structure is located between the cartilaginous endplates of the vertebrae as shown in the Figure 2.4. An apparent boundary between nucleus pulposus and annulus fibrosus can be identified in this image. The intervertebral disc has its own unique structural and metabolic properties. Its composition changes significantly during development, growth, ageing and degeneration, what changes the way how discs respond to changes in mechanical loadings [Adams *et al.*, 2010]. Recently, with the development of magnetic resonance imaging (MRI) techniques, the nutrition supply of the IVD has been investigated *in vivo* in animals and humans [Haughton, 2006]. It has been suggested that the loss of nutrient supplies may lead to disc degeneration.



**Figure 2.4 - The components of the intervertebral disc (adapted from [Postacchini, 1999]).**

### **2.2.1. Nucleus Pulposus**

The nucleus pulposus (NP) is the soft and hydrophilic part of the IVD and it is located within the central zone of the disc (Figure 2.4). The NP contains fibrocytes as well as chondrocytes, and an isotropic tissue based on fibres organized randomly and arranged radially. The fibres are substantially collagen and elastin fibres, which may be more than 150  $\mu\text{m}$  in length. They are embedded in a highly hydrated proteoglycan-water gel. The role of the proteoglycan is to attract water and to give the nucleus its swelling capacity, and thus developing an osmotic pressure. Its extracellular matrix is gelatinous and the cells of the NP are originally derived from the notochord [Raj, 2008]. The boundary between nucleus and annulus is not well defined as collagen fibres (nucleus) are linked with the inner annulus laminae.

The nucleus comprises approximately 40% of the cross-sectional area of IVDs and its composition of water (70 to 90%) is higher at birth and tends to decrease with age. The size of the nucleus and its capacity to swell are greater in the cervical and lumbar regions [Bibby *et al.*, 2001]. Nowadays, the water inside the disc can be measured *in vivo* with the help of some medical imaging techniques [Haughton, 2006]. Nutrition takes place mainly through passive diffusion and nutrients (essentially oxygen, glucose, amino acids, and sulphate) are supplied to the disc by the blood supply at the IVD margins. These nutrients move from the surrounding capillaries to the disc cells [Raj, 2008].

### **2.2.2. Annulus Fibrosus**

The annulus fibrosus (AF) is a zone of the intervertebral disc that consists in series of 15 to 25 concentric rings (or lamellae) and gradually becomes differentiated from the non-defined border of the nucleus and forms the outer boundary of the disc. The lamellae contains collagen fibres lying about  $\pm 60^\circ$  parallel within each lamellae, alternating to the left and right of it in adjacent lamellae [Shankar *et al.*, 2009]. Elastin fibres lie between the lamellae and may possibly allow the disc to return to its original position following flexion or extension. As elastin fibres extend radially from one lamella to the next, they may also play a role in binding the lamellae together.

The cells of the AF, particularly in the outer region, tend to be fibroblast-like, elongated, thin, and aligned parallel to the collagen fibres, which may be more than 30 mm long. The inner annulus cells tend to become more oval as one moves inside the nucleus pulposus and the collagen fibres tend to become less dense and more loosely organized. The outermost layers

of the AF tend to be more dense and resistant to tensile forces. These layers are firmly attached to the endplates and to the vertebral bodies, and are reinforced by the posterior and anterior longitudinal ligaments [Shankar *et al.*, 2009].

### **2.2.3. Cartilaginous Endplate**

The cartilaginous endplate (CEP) is a hyaline cartilage layer, with approximately 1 mm thickness and it allows to junction between annulus and vertebral body. The composition of the CEP varies slightly in the vicinity of the annulus. It is composed mainly of collagen fibres connected to the IVD. Though, the area immediately adjacent to the osseous vertebral body is made up of primarily hyaline cartilage and is less adherent and more susceptible for separation during trauma. The CEP is highly vascularised until the first year of life, and then there are essentially no blood vessels, increasing the tendency to disc degeneration [Shankar *et al.*, 2009].

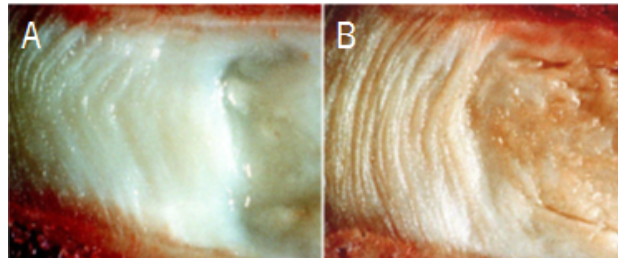
These three components of the IVD – annulus, nucleus and endplates – have an essential function on the IVD biomechanical behaviour. In the next section some of the most relevant issues related with disc degeneration and their mechanical properties are briefly addressed.

## **2.3 Biomechanics and degenerative diseases of the IVD**

Back pain is one of the symptoms of degenerative disc diseases (DDD). Disc degeneration can be associated with sciatica, disc herniation or prolapse. [Urban *et al.*, 2003]. The causes of the DDD are still unknown but many studies have been developed in order to understand them, especially those that cause disc herniation. The number of patients with intervertebral disc herniation is increasing every year and the lumbar disc herniation is the most common musculoskeletal disorder (in most of cases, at the L4-L5 and L5-S1 levels) [Rannou *et al.*, 2001; Shankar *et al.*, 2009].

It is known that degenerative changes of the IVD occur as a natural part of biological contributions of ageing (Figure 2.5) and genetics, but also as the result of an environmental contribution to disc degeneration and its biomechanical failure [Iida *et al.*, 2002].

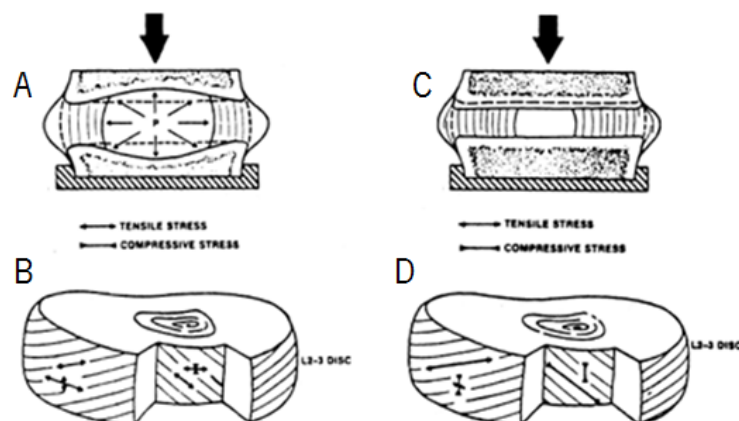




**Figure 2.5 – Mid-sagittal sections of intervertebral discs showing the biochemical appearance of ageing (A) a disc typical of ages 20–30 years and (B) a disc typical of ages 50–60 years [Adams *et al.*, 2010].**

As mentioned earlier (Chapter 2), the IVD works biomechanically to maintain the flexibility and mobility of the spine due to the relative motion (displacements and rotations) of adjacent vertebrae. The disc is always under loadings from body weight and muscle activity, and mainly during sleep (minimum-loading bearing state) it can recover and restore its properties. It is known that the biomechanical responses of the disc depend on its macromolecular composition. The disc is a set of isotropic and anisotropic soft-tissues and, depending on the fibres orientation, it allows to deal with a great complexity and intensity of loadings resulting from our daily activities.

In a normal lumbar disc, the nucleus carries the compressive loadings and the annulus the tensile stresses. When the disc is degenerated this loading capacity diminishes. It happens because the amount of water retained inside the disc diminishes, and thus the tensile stresses in the collagen fibres (annulus fibrosus) become compressive loads because they are not any more activated by the nucleus [Jensen, 1980]. Figure 2.6 represents schematically the behaviours of the normal and degenerated disc under a compression loading.



**Figure 2.6 – Compression loading (A) a normal non-degenerated and (C) degenerated disc. Outer annulus layers have a large tension stress along the fibres and also in the tangential peripheral direction. The inner annulus fibres have stresses of smaller magnitude (B). Annulus fibres show outer layers are subjected to increased amount of tensile stress. The inner annulus fibres have a high compressive stress (D) [Jensen, 1980].**

The nucleus herniation leads to a loss in the mechanical loading capacity, a decrease in the disc height and to the disc degeneration. The loss of the hydraulic and elastic properties in the disc depends on the decrease of the water's content and therefore in a lessening of the preload effect of the nucleus; a decrease in the elastic collagen tissue in the annulus with replacement of large fibrous inelastic bands and cartilage degeneration in the end-plates [Jensen, 1980].

The disc degeneration can be identified in five different grades, and the usage of some imaging techniques analysis can help the clinical diagnosis. Non-invasive medical techniques, such as radiography, computed tomography (CT) and magnetic resonance imaging (MRI), are commonly used in medicine for the diagnosis of DDD [Wills *et al.*, 2007].

Studies with animal discs, for example ovine discs [Reid *et al.*, 2002], are essential due to the difficulties in obtaining and working with human specimens. Although Smit, [2002] had shown that a quadruped can be a representative animal model for Human spine, *in vitro* tests have shown that the mechanical properties of the disc cannot be restored, especially if the physiological limits of the tissues are exceeded, during the tests. Consequently, with this difficulty to correlate the disc responses to *in vivo* and *in vitro* loadings, there is a necessity to create models that allow to virtually studying such mechanisms. The FE analysis is an important tool for simulation and to understand the stress distributions inside the disc. Knowing the different behaviours of the disc (native and degenerated) could help improve some strategies to understand the degenerative disc diseases. Obviously both the accuracy of geometrical modelling and mechanical behaviour characterization play a paramount role to ensure the reliability and significance of numerical analysis when compared with *in vivo* studies.

---

## Chapter 3. Medical Image Techniques

---

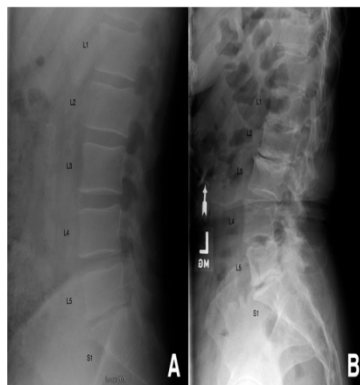
### 3.1. Introduction

Nowadays, the diagnosis based on medical imaging provides an effective way to non-invasively represent the anatomy of the Human body. Several imaging techniques are available to help in the diagnosis of DDD, therapy and research of the back pain [Wills *et al.*, 2007]. Depending on the patient's problem, different techniques can be used to evaluate DDD.

This chapter summarizes most common patient *in vivo* non-invasive data acquisition techniques of the Human lumbar spine. Plain radiography can show bones of lumbar spine, CT depicts images of the vertebrae and, to a certain extent, images of the muscles, vessels and nerves, while MRI can provide images of the shape and internal structure of bones, disc, joints, muscles, vessels and nerves [Wills *et al.*, 2007]. These techniques offer the possibility to produce a set of transverse slice 2D images. Consequently these images can be used to reconstruct the 3D model after applying several imaging processing procedures and numerical methods such as denoising, smoothing, segmentation and, finally, 3D reconstruction and sampling.

#### 3.1.1. Plain radiography

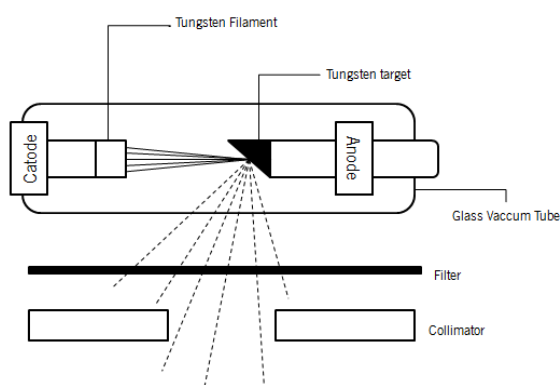
Generally, the plain radiographs are the first diagnosis technique used to obtain information about the back pain. Essentially, this technique allows examining bones structure. Disc space narrowing, development of endplate sclerosis and osteophytes and, occasionally, gas formation in the disc can be seen through radiography (Figure 3.1). Despite all of this, radiographs are not able to identify any damage in soft tissues (e.g., in the case of disc herniation) [Wills *et al.*, 2007].



**Figure 3.1 – Plain radiographs showing the following: (A) Narrowing of the L5-S1 disc space with mild osteophyte formation demonstrating mild DDD at this single level. (B) Disc space narrowing, endplate sclerosis, and osteophytes at L1-L2, L2-L3, L4-L5, and L5-S1 in this patient with marked multi-level DDD. Retrolisthesis of L3 on L4 is also seen [Wills *et al.*, 2007].**

X-ray system consists of a vacuum tube which contains a cathode that directs a stream of electrons into a vacuum, and an anode, which collects the electrons thus forming a beam of electrons. X-ray photons are produced by this electron beam and are accelerated at high speed towards patient [Suetens, 2009].

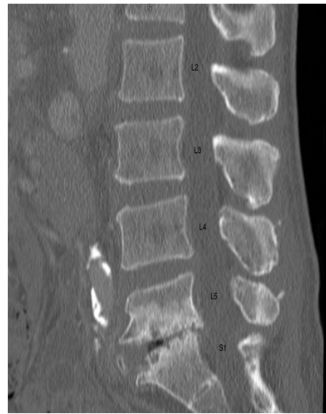
2D representation image is obtained as the result of this interaction between the X-ray photons and the patient. Interaction between X-ray and the patient depends on the density and composition of the different body areas. The image contrast is the intensity difference in adjacent regions of the image and it depends on the attenuation coefficients, the spectrum beam, and on the thicknesses of the different tissue layers. Another important factor that influences the contrast is the absorption efficiency of the detector, which is the fraction of the total radiation hitting the detector that is actually absorbed by it. Higher absorption efficiency yields a higher contrast [Butler *et al.*, 2007].



**Figure 3.2 – Principle of the plain radiography technique (adapted from [Butler *et al.*, 2007])**

### 3.1.2. X-ray computed tomography

The first computed tomography (CT) scanner was presented by Godfrey Hounsfield [Hounsfield, 1973]. Since then, new and improved scanners have been developed. CT has the advantage to provide a quick and non-invasive method of assessing patients. This procedure is particularly suited to high X-ray contrast structures, such as bones, and is limited in the analysis of soft-tissues like intervertebral discs and ligaments. As opposed to plain radiographies, computed tomography images allow to diagnose problems and to reveal marginal osteophytes, foraminal stenosis, disc space (vacuum phenomenon) arising and endplate sclerosis [Wills *et al.*, 2007].



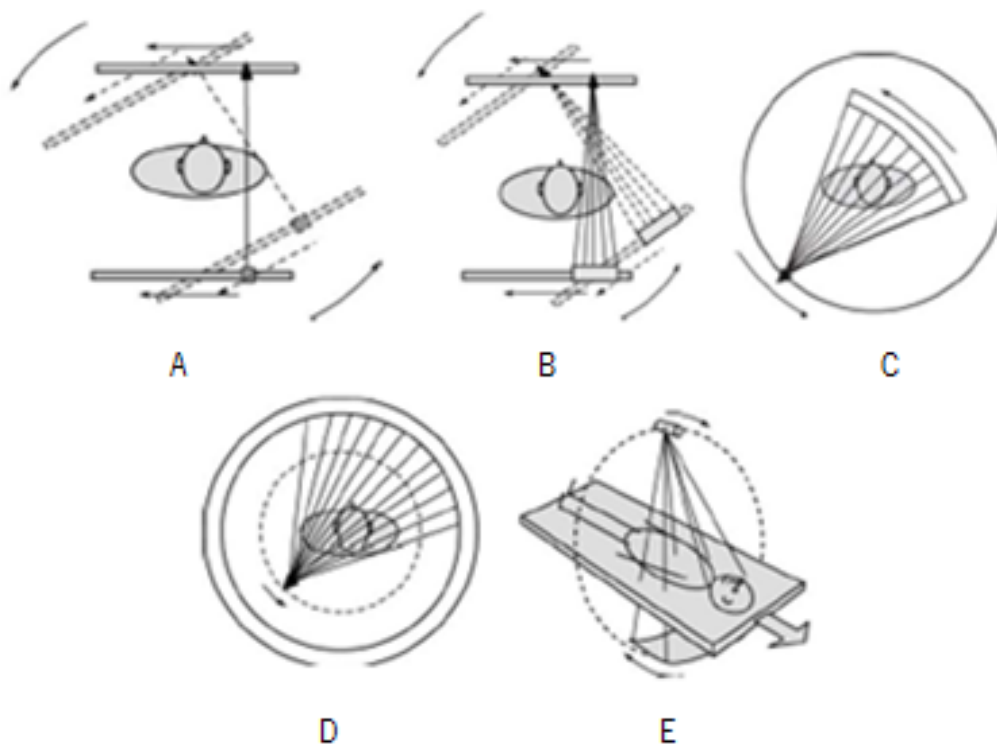
**Figure 3.3 – CT scan showing complete loss of the L5-S1 disc space with severe endplate sclerosis and development of osteophytes. [Wills *et al.*, 2007].**

The CT system is simple and uses X-rays as the radiography technique. In conventional CT, the X-ray tube and the detector rotate around the stationary table<sup>3</sup>. A source that emits an X-ray beam with very high energy can be rotated around one axis while the patient is translated parallel to that axis. This beam is attenuated by absorption and scatters as it passes through the patient body with the detector measuring transmission. A computer reconstructs the image for this single slice. The patient and the table are then moved to the next slice position and the next image is obtained. This way, X-ray images of each section are digitally recorded from many angles [Butler *et al.*, 2007; Suetens, 2009].

---

<sup>3</sup> This table is where the patient is lying.

There are different generations of CT technique and Figure 3.4 shows these five types of CT scanners. In the first-generation CT scanner, the X-ray source and the detector have two motions: linear translation and rotation. The X-ray beam is narrow and the scanning time to obtain parallel-beam projections are approximately 25 minutes. The second-generation CT used narrow fan-beam geometry with 12 detectors. This scanner has two motions as first-generation: linear translation and rotation but the scanning time is too short (about 1 minute). The third-generation CT uses a fan-beam geometry but with 1000 detectors. The difference in this scanner is that no linear translation motion is necessary. The scanning time is approximately 0.5 seconds and this CT scanner is frequently used in medical imaging. The fourth-generation CT has a stationary ring detector and the X-ray source rotates around the patient. This scanning method is very fast but it is subjected of a high scattering level and it is impossible to collimate the X-rays on the detector [Zeng, 2010]. Nowadays, modern CT scanners perform a helical scanning. The X-ray source and the detectors rotate while the table has linear translation in the axial direction. This type of scanner has a 2D multi-row detector and it acquires cone beam data.

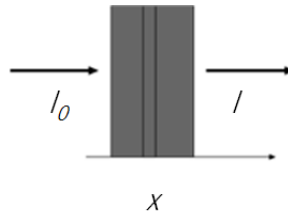


**Figure 3.4 – Principle of different generations of CT scanner. First (A), Second (B), Third (C), Fourth (D) and modern (E) generation scanner (adapted from [Zeng, 2010]).**

The principle of this technique is based on a monochromatic X-ray beam which crosses the body and it can be absorbed. This phenomenon is described by Beer's Law:

$$I = I_0 e^{-\mu x} \quad (3.1)$$

where  $I_0$  and  $I$  are the initial and final X-ray intensity,  $\mu$  is the material's linear attenuation coefficient (units 1/length) and  $x$  is the length of the X-ray path [Suetens, 2009].



**Figure 3.5 – The principle of attenuation.**

Similarly to the case of radiography, the attenuation of the X-ray beam is directly proportional to tissues density. This attenuation can be “measured” by the level of grey attributed to each pixel of a given image. The level of grey of each pixel is usually expressed by CT numbers in Hounsfield scale, defined as

$$HU = \frac{\mu_x - \mu_{water}}{\mu_{water} - \mu_{air}} \times 1000 \quad (3.2)$$

where  $\mu$  (water) = 0 HU and  $\mu$  (air) = -1000 HU [Butler *et al.*, 2007; Suetens, 2009].

These values can be used to differentiate tissues in agreement with their attenuation, on a scale from +3071 (higher attenuation) to -1024 (lower attenuation) on Hounsfield scale, i.e., on 4096 levels of attenuation. The contrast resolution of CT images depends on the differences between Hounsfield values of neighbouring tissues, the larger the better. For example, bone and calcified structures have values of 200–900 HU. Some clinical applications look at air–tissue or tissue–bone contrasts on the order of 1000 HU, but other clinical exams focus on smaller soft tissue contrasts of a few HU. An optimal perception requires a suitable grey level transformation. Although better than plain X-ray in differentiating soft tissue types, CT is not as good as magnetic resonance imaging (MRI).

CT is mainly suited for bones. One of the most important advantages of this technique is the ability to reproduce a 3D structure and to represent a 2D cross-section with high accuracy. In CT, this process depends on some technological characteristics that affect image quality, such as spatial resolution, contrast resolution, linearity, noise and artefacts.

### **3.1.2.1. Micro-computed tomography**

Micro-computed tomography (or micro-CT) is a new and innovative field of non-invasive imaging technique. The main advantage of this scanning technique is its micro scale. Recently, several studies [Holdsworth *et al.*, 2002; Ritman, 2004] have been carried out with small animals using this technique to obtain high-resolution 3D models with application on, for instance, monitoring efficacies of drugs in disease treatment, among others.

Micro-CT is based on the same principle of conventional CT, but with a much higher resolution than the one in conventional clinical scanners. Clinical tomography scanners have resolutions around one millimetre, while micro-CT scanners may have resolutions below five microns [Ritman, 2004].

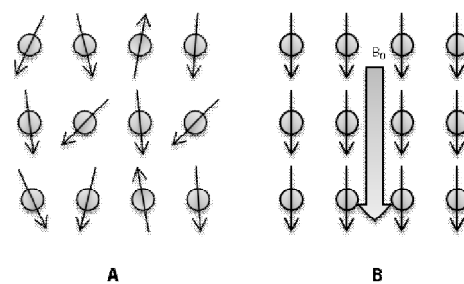
### **3.1.3. Magnetic Resonance Image**

Magnetic resonance imaging (MRI) is another medical imaging technique frequently used both in medical diagnosis and as surgery supporting tool, with the ability to produce high quality images. Usually, MRI provides detailed information about changes associated with DDD. In case of soft tissues, the contrast is better than within CT, what shall allow an easier and more effective identification of the most relevant tissue's domains, for instance inside an intervertebral disc. MRI also allows a better visualization of the vertebral marrow, the ligaments and contents of the spinal canal [Fujiwara *et al.*, 1999]. In cases such as infections or tumours, the MRI provides information about the source of the pain. However, in cases where the pain is due to mechanical causes (most common cases) the MRI does not provide any additional information.

MRI is a medical imaging technique based on a magnetic field ( $B_0$ ) and pulses of radio waves to produce images of internal organs and structures. MRI uses non-ionizing radio frequency (RF) signals to acquire its images and it is best suited for non-calcified tissues. MRI depends on protons mobility in tissues, and since most protons in biological tissues are in water, normal clinical applications involve the imaging of hydrogen nuclei (protons). One can assume that the



protons in the patient tissues behave like tiny bar magnets, which are normally randomly oriented in space. When the patient is placed within a strong magnetic field, some of the atomic nuclei are aligned with respect to such external magnetic field (Figure 3.6). The protons behave like miniature magnets and spin at a specific frequency. When the protons are back to their equilibrium position (i.e., relax to a lower energy state), they release energy like a small radio transmitter. These radio signals are detectable (by an aerial) and electronically amplified, in order to create a magnetic resonance image. Human spine MRI exams, used to identify back disorders, IVD diseases and spinal cord disorders, are usually performed using clinical magnetic fields (1.5 and 3 Tesla), with specific phased-array coils for spinal MRI exams.



**Figure 3.6 – The tiny bar magnets (A) before and (B) after the tissues being placed within a strong magnetic field.**

When the proton relaxes, there are two processes before it emits radio waves: the longitudinal recovery (which has a recovery time, T1) and the transverse relaxation (with a relaxation time, T2). The relative proportions of T1 and T2 varies for different tissues. In MRI studies of IVD degeneration, the qualitative analysis of T1-weighted and T2-weighted images in the sagittal and axial planes are used. As showed in Figure 3.7, these processes may highlight the disc degeneration through the modification of the signal intensity.



**Figure 3.7 – T1-weighted (A) and T2-weighted (B) sagittal MRI demonstrating a disc herniation at L4-L5 [Wills *et al.*, 2007].**

Generally, the T1-weighted imaging is used to study the abnormalities of the spine. However, lower signal intensity (T2-weighted) images are associated with degenerative IVDs and a loss of water content of the disc. By measuring the disc height, the signal intensity alteration and the signal-to-noise ratio it is possible to complete these exams [Wills *et al.*, 2007].

### **3.1.3.1. Micro Magnetic Resonance Imaging**

Nowadays, with the recent advances in medical imaging techniques, it is possible to obtain MRI images with higher resolution via micro-MRI scanners [Majumdar *et al.*, 1997]. This technique allows to distinguish different types of tissues with higher detail due to its micro-scale ( $\mu\text{m}$ ) resolution. Nevertheless, the low signal-to-noise ratio and the inhomogeneous signal becomes an obstacle during model reconstruction from micro-MRI images [Strolka *et al.*, 2003].

Recently, several studies with micro-MRI techniques have been developed. Among others, Uffen and co-workers evaluated the detection capacity of different tissues with micro-MRI in nine animals that were part of a goat spinal fusion study [Uffen *et al.*, 2008]. Liu and co-workers demonstrated the importance of micro-MRI technique for *in vivo* trabecular bone morphometry [Liu *et al.*, 2010]. Bonny and co-workers demonstrated that the high-quality can be achieved at 9.4 T using micro-MRI images of an *in vivo* mouse spinal cord. The increasing availability of clinical high resolution MRI scanners will support the spread on many clinical application of this technology in a near future [Bonny *et al.*, 2004]. The micro-MRI technique is a valuable tool to aid in future clinical evaluations and decisions.

### **3.1.4. Other medical image techniques**

Ultrasound, discography and CT-myelography, are also commonly used in clinical diagnosis of the low back pain. However, these techniques present some restrictions - for example, the use of contrast agents that are invasive and do not provide good exam conditions for the patient or their low image resolution, which does not allow to clearly distinguish the different anatomical regions of interest in the images.

## **3.2. Comparison of medical image resolution**

The resolution of a medical image depends on the imaging method, the characteristics of the equipment, and the imaging values selected by the operator. These values will influence the image resolution and, consequently, the visibility of specific body features. The following table presents a

synthesis of the different and most typical resolutions of the medical imaging techniques addressed in this chapter, as well as their main characteristics and applications.

**Table 3.1 – Resolution and some characteristics of images from different medical imaging techniques.**

	<b>X-radiography</b>	<b>X-ray CT</b>	<b>Micro-CT</b>	<b>MRI</b>	<b>Micro-MRI</b>	<b>References</b>
<b>Spatial resolution</b> [mm]	≈ 0.1	≈ 0.1 - 0.5	≈ 0.05 - 0.1	≈ 0.7 - 1.0	≈ 0.1 – 0.3	[Ritman, 2004]; [Higgins <i>et al.</i> , 2006]; [Hitchon <i>et al.</i> , 1995]; [Henke, 2007]
<b>Temporal resolution</b> [ms]	≈ 10	≈ 500	≈ 10	≈ 10	undefined	[Higgins <i>et al.</i> , 2006]
<b>Slice thickness</b> [mm]	undefined	≈ 1.0 – 5.0	≈ 0.05 – 0.06	≈ 1.0 – 3.0	≈ 0.3 – 0.6	[Henke, 2007; Wills <i>et al.</i> , 2007]
<b>Soft Tissues</b>	--	-	-	++	++	[Wills <i>et al.</i> , 2007]
<b>Bone</b>	+	++	++	-	-	[Wills <i>et al.</i> , 2007]
<b>Diseases</b>	Disc spacing narrowing; Spondylarthrosis	Disc herniation; Spondylolisthesis; Spinal Canal Stenosis; Trauma;	Disc herniation; Spondylolisthesis; Spinal Canal Stenosis; Trauma;	Disc herniation; Spondylolisthesis; Spinal Canal Stenosis	Disc herniation; Spondylolisthesis; Spinal Canal Stenosis	[Krämer, 2008]; [Wills <i>et al.</i> , 2007]



---

## Chapter 4. Three-dimensional reconstruction from medical imaging

---

The starting point for the 3D geometrical modelling by finite elements of a motion segment is the generation of a 3D voxel-based geometrical model, obtained after denoising, smoothing and segmentation of a set of 2D medical images. This chapter addresses and describes the procedures for 3D reconstruction from 2D medical imaging obtained from computed tomography (CT), micro-CT, magnetic resonance imaging (MRI) or micro-MRI, 3D reconstruction techniques and some segmentation algorithms. Advantages and drawbacks of the main reconstruction algorithms and procedures are illustrated with the 3D reconstruction of a goat IVD from real medical imaging data obtained from MRI and micro-MRI using the image processing software ScanIP (Simpleware Ltd, Exeter, UK).

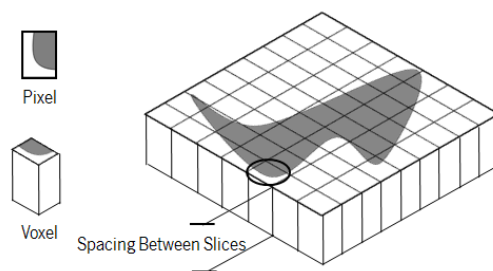
### 4.1. Introduction

Medical imaging techniques (detailed in Chapter 3) enable one to create a set of related 2D images, where each 2D image represents a thin "slice" of the body. This set of 2D images one shall be able to reconstruct a 3D voxel-based model. Nevertheless, the 3D model reconstruction process is not linear and the images shall be, in most of cases, subjected to image processing. The fundamentals of image processing are based on parameters that are inherent to images, such as image resolution. The image resolution is the level of detail of an image and a measurement of its quality, i.e., resolution defines pixel size. Higher resolution means more image detail, which is affected by interrelated factors (e.g., matrix size, pixel size, field-of-view, voxel size, slice thickness, focal spot size and blur) [Suetens, 2009].

In an imaging acquisition, a so-called matrix is used to break the image into columns and rows of tiny squares. Each elemental unit, called pixel, is known to be the smallest component of an image. Thus, a given amount of pixels gives rise to an image. The matrix size refers to how many pixels are used in the definition of the grid. For example, a 512 matrix will have 512 pixels

across the rows and 512 pixels down the columns. The most common matrix sizes used in medical images are 256, 512 and 1024. Another image parameter is the field-of-view (FOV) which represents the maximum size occupied by the object in the matrix. One of the most common problems that an image may present is a high FOV, which may cause a blur image and low resolution images [Suetens, 2009].

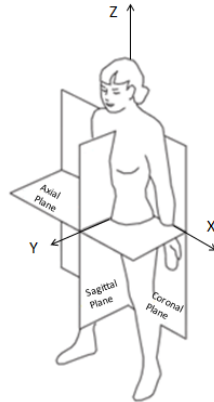
During the 3D reconstruction procedure from 2D images, each pixel is converted into a voxel (3D unit that represent a 2D pixel unit), giving a kind of depth to the image, as shown in Figure 4.1. A voxel represents a volume of patient's data. The length of the voxel correlates to the operator selection of slice thickness. Therefore, the slice thickness plays an even larger role in volume averaging (as well as the subsequent spatial resolution or slice spacing) than either display FOV or matrix size.



**Figure 4.1– The pixel and the voxel representation.**

Generally, a voxel has a parallelepiped shape, which can be reduced to a cube in special cases. Each voxel has a defined volume and a level of grey resultant from medical imaging acquisition process. Thus, this level of grey is the paramount property attributed to each voxel, given its physical meaning. This grey scale is defined by a large spectrum of representations of shades ( $2^{16}$ ) between white and black. The grey scale created especially for tomographic images has a unit of measure called Hounsfield (see section 3.1.2 - X-ray computed tomography). The tomographic image consists in more than 2000 tonalities, but the human eye is only able to distinguish between 10 to 60 grey tonalities. Because of this, and to make the differentiation between structures easier, computational resources (such as feature called *window*) enable to narrow the values of the grey scale. This works as an alteration in the grey tones of the image accordingly to the human vision of the tomography data. However, it is not possible to use at the same time different sets of *window* (i.e., bone, fat, soft tissue) [Suetens, 2009].

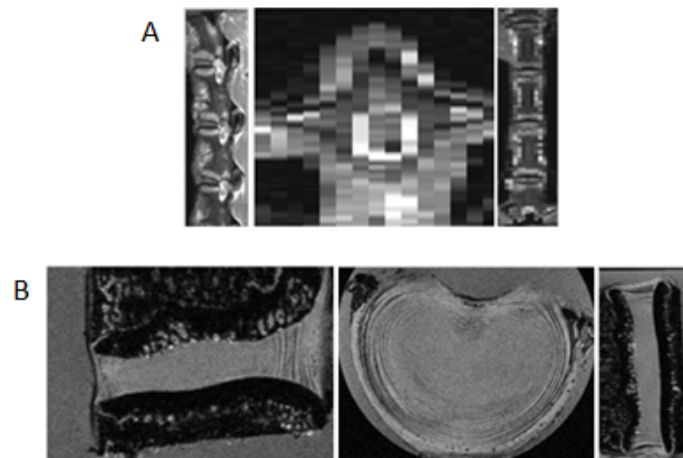
Fundamentally, imaging techniques deal with 3D model reconstruction from a series of 2D images (projections) taken at various angles around the body. Three different plans of the image can usually be obtained through tomography techniques: sagittal, coronal and axial planes (Figure 4.2) which, in this work, were also defined as X, Y and Z axes for three different planes, respectively.



**Figure 4.2 – The three main imaging plans of the human body: sagittal (YZ), coronal (XZ) and axial (XY) (adapted from [Dougherty, 2009]).**

#### **4.2. 3D reconstruction of a real goat motion segment**

In this study two sets of medical images of two different goat motion segments were used. The medical images were obtained from two different techniques: MRI and micro-MRI. The first set of images consists of 14 sagittal, 336 axial and 83 coronal slices with 3 mm of thickness and 3.3 mm of spacing between slices (voxel size:  $0.3 \times 0.3 \times 3.3 \text{ mm}^3$ ). The second set (micro-MRI images) has 250 sagittal, 124 axial and 185 coronal slices with 0.12 mm of slice thickness and 0.12 mm of spacing between slices (voxel size:  $0.12 \times 0.12 \times 0.12 \text{ mm}^3$ ).



**Figure 4.3 – The (A) MR and (B) micro-MR images of the lumbar goat motion segment in different planes (sagittal, axial and coronal, respectively).**

Figure 4.3 shows clearly the huge difference of resolution between both sets of images. In the first set, Figure 4.3(A), it is difficult to distinguish the different tissues and domains, such as discs and vertebrae. On the other hand, in Figure 4.3(B) is evident that micro-MRI images allow a much easier and accurate identification of these structures.

**Table 4.1 – Comparison between the two types of MRI images used in this work.**

<b>Image Data</b>	<b>MRI</b>	<b>Micro-MRI</b>
<b>Equipment</b>	Siemens	Bruker BioSpin MRI GmbH
<b>Institution</b>	MRI Centrum Amsterdam, Netherlands	University Eindhoven, Netherlands
<b>Slice Thickness</b> [mm]	3	0.12
<b>Spacing Between Slices</b> [mm]	3.3	0.12
<b>Rows</b>	384	256
<b>Columns</b>	168	256
<b>Pixel Spacing</b> [mm]	0.30/0.30	0.12/0.12
<b>Voxel size</b> [mm <sup>3</sup> ]	0.3x0.3x3.3	0.12x0.12x0.12

Bearing in mind the main purpose of this work, i.e., the 3D geometrical modelling by a FE mesh, both sets of medical images must be processed in order to obtain denoised, smoothed and segmented 2D images, the first step for the 3D FE mesh generation procedure. Thus, segmentation algorithms play a paramount role on the reconstruction procedure and drive the reconstruction procedure accuracy. Segmentation algorithms will be briefly addressed on the next section, and their application exemplified making use of the real medical imaging data of the goat motion segments above mentioned.

### **4.3. Segmentation Algorithms**

Segmentation can be understood as a decision algorithm to select, from all voxels of a 3D voxel-based geometrical model, all the ones that belong to, and define, a given domain and/or 3D region of a hard or soft-tissue of the bio-structure under analysis. In the case of a motion segment, the segmentation algorithm must be able to identify, at least, the domains of bone, annulus fibrosus and nucleus pulposus, simply based on 2D image data and 3D reconstruction (level of grey of each pixel/voxel and spatial voxels organization and gradients, among others). Thus, usage of computational algorithms to identify/define anatomical structures and other regions



of interest (ROI) shown to be an important task of 3D reconstruction and accuracy of 3D geometrical modelling by finite elements.

The process of decomposition of a 3D domain reconstructed from 2D medical images into its different regions (segments) is called segmentation. There is an increasing need to develop algorithms able to segment anatomical structures. However, these structures are often non-regular and not always the existing methodologies allow an automatic and user-free segmentation process. Conventionally, most of the image segmentation techniques use large types of image (CT, MR, ultrasound, PET, SPECT, and others). Nevertheless, the performance of these techniques can be improved by combining algorithms to make the segmentation more effective. Manual, semi-automated or fully automated segmentation in anatomical imaging such as CT and MR are nowadays a very hot topic under intense research.

Several methods for segmentation have been proposed in literature, but their application depends mainly on the main images' features and properties. Until now there is not an optimum algorithm to solve and eliminate all imaging artefacts, such as image noise and patients' motion. The choice of the segmentation method is a difficult task. The segmentation algorithms play a vital role in several biomedical imaging applications such as: quantification of tissues' volumes, diagnosis, localization and amplitude of pathologies, study of anatomical structures, treatment planning, partial volume correction of functional imaging data, computer integrated surgery and, also, on geometrical reconstruction for further analysis.

A large number of segmentation algorithms can be found in literature. Many authors differ in the classification of the segmentation algorithms [Pal *et al.*, 1993; Pham *et al.*, 1998; Bankman, 2000; Lakare, 2000; Ma *et al.*, 2010]. In this work, the algorithms that will be described hereafter are based on the work of Ma *et al.*, 2010. This author divides the segmentation methods into three categories: thresholding, clustering and deformable methods. These algorithms will be briefly introduced, and their application exemplified making use of the two sets of MRI and micro- MRI based images of a goat lumbar motion segment.

#### **4.3.1. Thresholding**

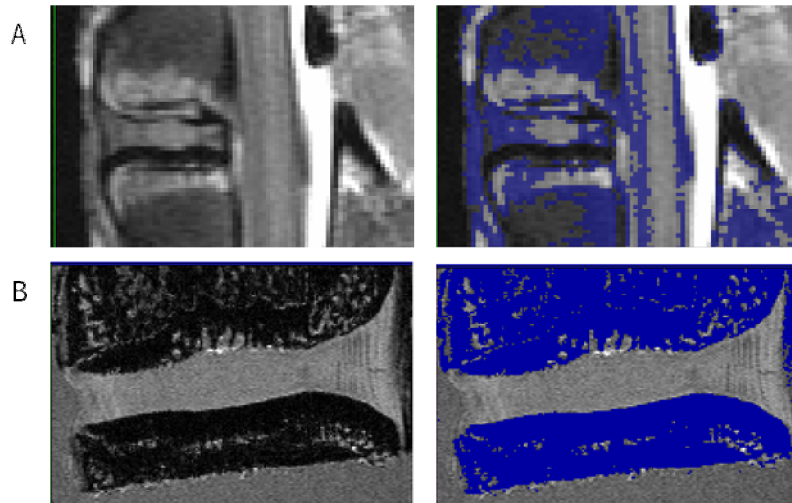
Thresholding is the first semiautomatic method applied in any segmentation approach given its simplicity [Bankman, 2000]. The most intuitive approach is global thresholding algorithm, in which

one threshold value is selected for the entire image based on the image histogram (bimodal). If the threshold value depends on local properties of some image regions (for example, local average grey value), it is called local, and if the local thresholding is selected independently for each pixel (or groups of pixels), it is called dynamic or adaptive thresholding.

In global thresholding, a predefined threshold value ( $T$ ) is selected and an image is divided into groups of pixels, to which values greater or equal than the threshold or values less than the threshold are assigned. The object and the background pixels are defined in two different grey levels. A binary image  $g(x, y)$  with pixels with value 1 correspond to the ROI, while pixels with value 0 correspond to the background. The next equation defines the global thresholding method.

$$g(x, y) = \begin{cases} 1 & \text{if } f(x, y) > T \\ 0 & \text{if } f(x, y) \leq T \end{cases} \quad (4.1)$$

This algorithm is simple and computationally very fast and effective. Commonly used method is the Otsu's method. This algorithm assumes that the image has two classes of pixels - foreground and background – and then calculates the optimum threshold separating these two classes [Dougherty, 2009]. It works better when the image contains regions of interest with homogeneous intensity, or the contrast of these is high. However, with the increasing number of regions (multi-level thresholding) or noise levels, or when the contrast of the image is low, global or local thresholding is difficult [Bankman, 2000]. Figure 4.4 shows the thresholding result (blue) in the two different sets of images. It is possible to see in Figure 4.4A the different grey values of the nucleus pulposus. However, in Figure 4.4B the difference between grey values is essentially between the bone and soft tissues' level of grey.



**Figure 4.4 – The thresholding algorithm applied to the (A) MR and (B) micro-MR images.**

In adaptive thresholding, a different threshold is used for different regions in the image. As the global thresholding, a binary image  $g(x, y)$  is formed, where pixels with value 1 correspond to the ROI, while pixels with value 0 correspond to the background and the only difference is the T value that changes with the coordinates of the image [Pal *et al.*, 1993; Bankman, 2000]. Equation 4.2 formally presents this algorithm.

(4.2)

One disadvantage of these two thresholding methods is that they only consider the intensity. In image processing, the relationship between the pixels is essential to guarantee that the pixels identified by the segmentation methods are adjacent. Hence, the thresholding methods can be classified into three different classes: edge-based, region-based and hybrid-based methods.

### **Edge-based methods**

The edge-based segmentation method consists in finding boundaries between different image regions and to segment these regions. Generally, an edge filter is applied during this segmentation process. The image and its pixels are classified as edge or non-edge depending on the filter output. Pixels which are not separated by an edge are classified as having the same category.

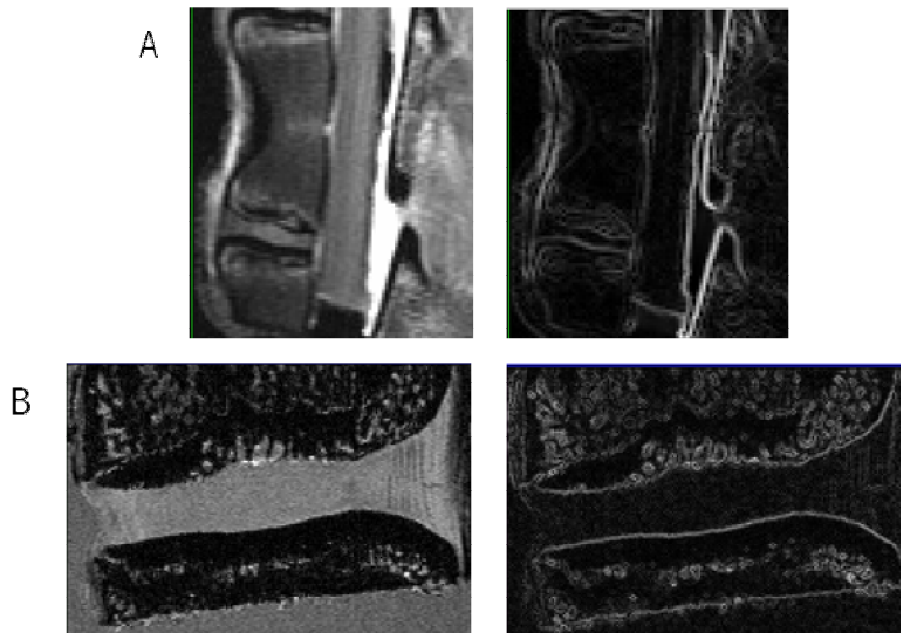
The local pixel intensity gradient may define an edge in the image. This gradient is an approximation to the first-order derivative of the image function [Bankman, 2000]. For a given image  $f(x, y)$ , we can define the edge strength (magnitude of the gradient) as:

$$\sqrt{\left(\frac{\partial f}{\partial x}\right)^2 + \left(\frac{\partial f}{\partial y}\right)^2} \quad (4.3)$$

and the direction of the gradient as:

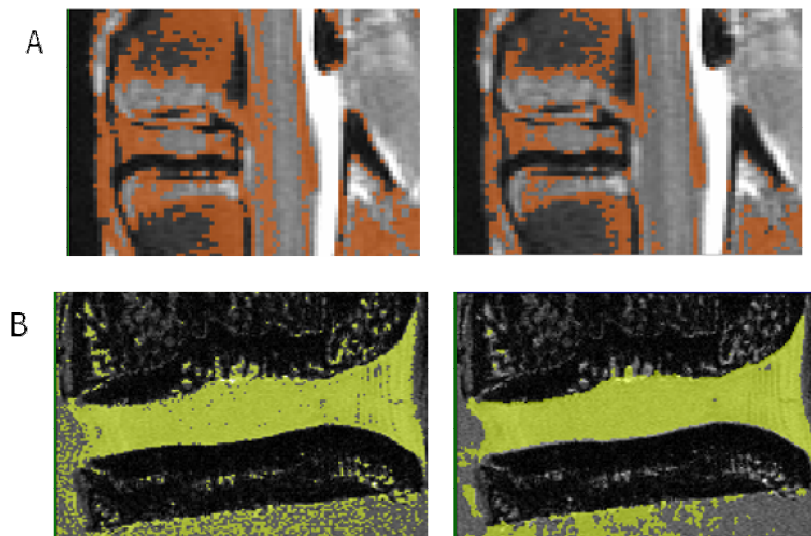
$$\arctan\left(\frac{\partial f / \partial y}{\partial f / \partial x}\right) \quad (4.4)$$

A gradient magnitude filter was applied to the images of the motion segment. The result can be seen in Figure 4.5.



**Figure 4.5 – The gradient magnitude filter applied to the (A) MR and (B) micro-MR images.**

There are several edge detectors such as Prewit, Roberts, Sobel, Laplacian and Canny which are used in this segmentation [Ma *et al.*, 2010; Barroso *et al.*, 2011]. In this study only the Canny edge detector was applied. It is the most common algorithm used in medical image analysing. Figure 4.6 shows an original image of the motion segment from micro- and MRI techniques used to test the performance of the Canny operator in the segmentation of the nucleus pulposus and the annulus fibrosus.

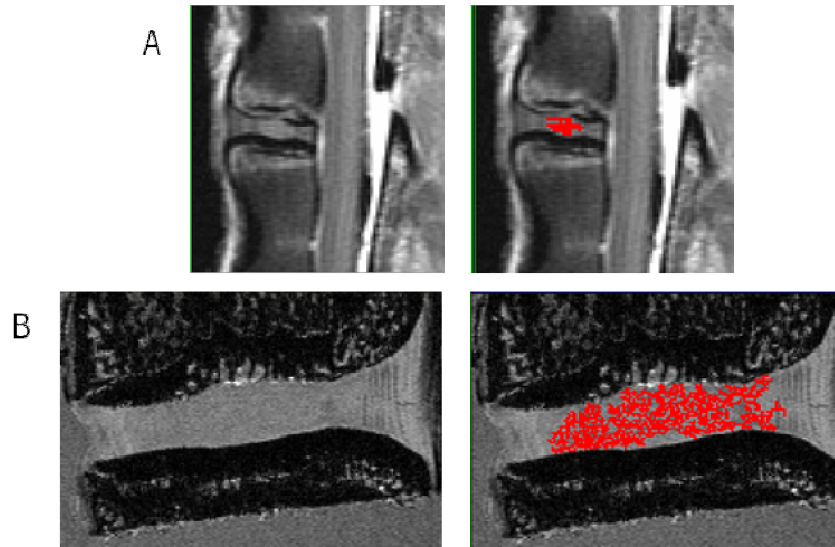


**Figure 4.6 – The Canny Operator applied to the (A) MR and (B) micro-MR images after thresholding.**

Occasionally, the Canny operator produces an opened contour of the regions and disconnected edges in the image. However, this segmentation method presents an important advantage as it is a simple and very fast method although it is very sensitive to noise, and the usage of another segmentation method as pre-processing is necessary to smooth the images (for example, the use of Gaussian filter) [Pham *et al.*, 1998].

### **Region-based methods**

Region-based segmentation techniques are based on grouping pixels that present uniform properties (for example, grey scale). These pixel groups are defined as a ROI of the image. Region growing is the most referred region-based method in literature. This method is based on intensity information (grey values) starting with a pixel or a group of pixels (called seeds) that belong to the region of interest. Seeds can be manually selected by an user or provided by an automatic seed finding procedure. Subsequently, these seeds are merged with their neighbour pixels that have similar intensities and these pixels are grouped in the same region (red in Figure 4.7) [Adams *et al.*, 1994]. When no more pixels can be added, the algorithm stops. The object is then represented by all pixels that have been selected during the growing procedure.



**Figure 4.7 – The region growing algorithm applied to the (A) MR and (B) micro-MR images.**

The advantage of region growing algorithm is its ability to perform a good segmentation of regions having the same properties and to detect connected regions. On the other hand, the main disadvantage is that a manual seeding process is usually needed.

### **Hybrid-based methods**

Hybrid algorithms employ other techniques to carry out segmentation. One example of a hybrid algorithm is the watershed, which combines the two methods mentioned above. As suggested by the name, this method uses the intensity values (grey scale) as reliefs and the gradient as elevation thus defining the boundaries between different structures. However, an over segmentation may occur with this method. It occurs when the image is segmented into an unnecessarily large number of regions [Ma *et al.*, 2010; Barroso *et al.*, 2011]. Therefore, hybrid methods using watershed algorithm shall be generally subject to post-processing.

### **4.3.2. Clustering methods**

Pixel classification techniques are pattern recognition methods that can be further subdivided into three groups: supervised, semi-supervised or unsupervised methods [Lakare, 2000].

Classifiers belong to the supervised methods category. These methods require (manual) segmentation training (pre-segmentation), which is used as reference for automatically segmenting new data [Lakare, 2000]. It is a very fast computationally method because it is non-iterative. However, this method has an extensive processing time in the training process and it is very sensitive to the initial conditions. Another disadvantage is the fact that supervised methods use the same training set for a large number of scans which can lead to biased results. Supervised methods incorporate the k-nearest neighbour (kNN), the artificial neural networks, the active shapes models (ASM), the maximum likelihood, the support vector machines (SVM), and the active appearance models (AAM) algorithms [Pham *et al.*, 1998; Bankman, 2000; Lakare, 2000; Ma *et al.*, 2010].

Semi-supervised algorithms use marks to guide the segmentation. It not only focuses on obtaining tight clusters but also on satisfying constraints with respect to a small set of pre-classified objects. Objects belonging to different classes belong to different clusters while objects belonging to the same class belong to the same cluster.

The clustering algorithm is considered to be an unsupervised classification algorithm. Unlike classifiers, this algorithm runs without using training data, i.e., it trains itself using the available data. This method consists in the segmentation of sets or clusters of pixels of the image with similar properties. The main advantage is that it takes low processing time because it does not require training data. However, this algorithm requires an initial segmentation (initial parameters) and it should not be used when the regions are very distinct. The most commonly used unsupervised clustering methods are the k-means, the fuzzy c-means and the maximum likelihood. Other unsupervised algorithms include the Iterative Self-organizing Data Analysis Technique Algorithm - ISODATA and the unsupervised neural network algorithm [Pal *et al.*, 1993; Bankman, 2000; Ma *et al.*, 2010].

Image registration techniques represent another type of pattern recognition algorithms. The template matching algorithms and the atlas-guided algorithms are also frequently used in medical image segmentation.

### 4.3.3. Deformable model-based methods

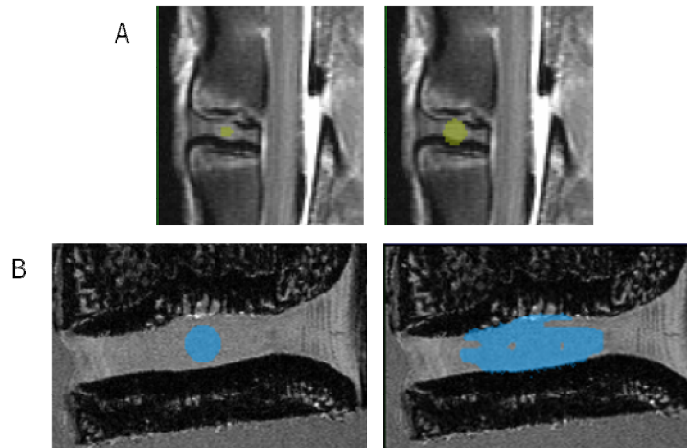
Deformable models are based on the definition of the region boundaries. These methods can be divided into parametric and geometric models, depending on the approach that is used for tracking the moving contour [Ma *et al.*, 2010].

Parametric deformable models consist in adapting a deformable model of an image using energy minimization. The curves/surfaces in this kind of methods are explicitly parameterized during the deformation. These models need to use closed parametric curves (or surfaces) which are deformed by internal and external forces. These forces derive of the local gradients of the grey scale. A parametric closed curve is initially placed in the vicinity of the region boundary to be identified. Then, and following an iterative energy minimization procedure, the parametric curve is successively corrected and approximated to be boundary to be identified. The internal forces keep it smooth throughout the deformation. However, the external forces are usually derived from the image/data to move the curve toward the desired feature of interest. Usually, the snake is the most popular algorithm of deformable models. It is used as an active contour which presents a high control in the smoothing and the adjustment of the convergence property in the curves. Also, this method is useful when the boundaries are slightly opened or with small dimensions. Generally, this algorithm is used when the structures are complex [McInerney *et al.*, 1996; Lakare, 2000; Ma *et al.*, 2010].

On the other hand, geometric deformable models are based on the theory of evolution of the curve and on level-set methods. They include the following models: Mumford-Shah, Chan and Vese e Malladi. The main advantages of the deformable models are: to be robust to noise and boundary gaps and to offer a coherent and consistent mathematical description. However, this method requires a manual interaction to input the initial parameters and to place the initial curve. Moreover, the deformable model algorithm is performed image by image [Lakare, 2000].

Other approach for structure segmentation is the geodesic deformable-based model. This method allows to connect the classical snakes based on energy minimization with the geometric active contours based on the theory of curve evolution (level-sets). Figure 4.8 shows an example of the application of this model to an micro-MR motion segment image. The active region is initialized with a square and the nucleus pulposus is segmented [Caselles *et al.*, 1997].

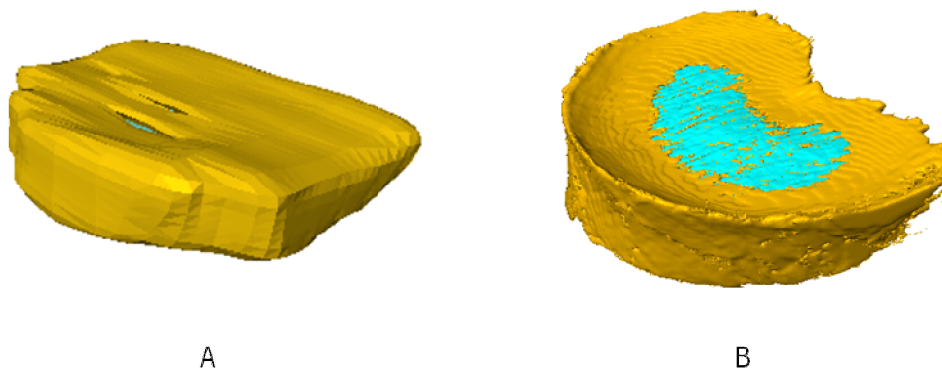




**Figure 4.8 – The segmentation of the IVD with the geodesic active contour applied to the (A) MR and (B) micro-MR images.**

#### **4.4. Case Study: segmentation of a goat intervertebral disc**

After segmentation of the sets of images of a goat lumbar IVD, two 3D anatomical voxel-based models were generated. Figure 4.9 shows two different models based on the aforementioned medical images with two different resolutions, acquired respectively by MRI and micro-MRI techniques.

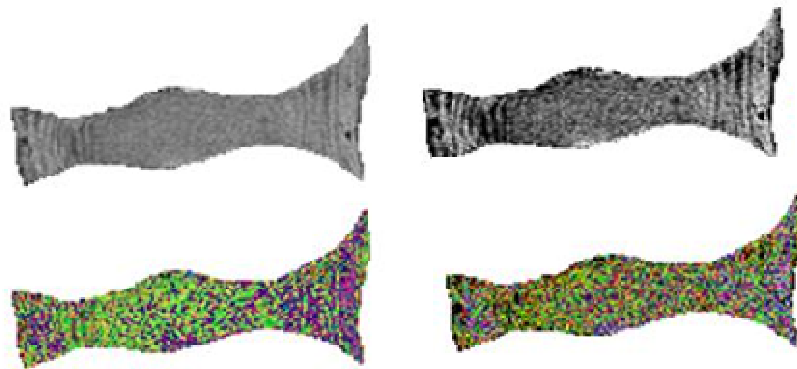


**Figure 4.9 – Two different 3D models based on (A) 0.3x0.3x3.3 mm<sup>3</sup> and (B) 0.12x0.12x0.12 mm<sup>3</sup> of MR image resolution.**

It is possible to observe that the 3D model generated from high resolution MRI images (Figure 4.9B) shows more accurate geometric details regarding the expected structures of an IVD. Unlike the previous model, the model shown in Figure 4.9A only roughly looks like an IVD, being really very inaccurate regarding the anatomical structures. However, it shall be noticed that even in the case of the most accurate model, it is observable the existence of tiny details and a

non-manifold domain, i.e., there exist several sub-domains that are not connected to the manifold domain.

Segmentation of structures is particularly difficult when the image contrast is too low, i.e., the grey levels are very similar among sub-structures, and sometimes the perceptible differences are smaller than the noise level. In such cases, a new strategy was employed to analyse the difference of contrast in the images. This process consists in converting the grey scale into a colour scale (coloured images) in order to find any more visible pattern detectable by the Human eye. It is based on information that characterizes a DICOM (Digital Imaging and Communications in Medicine) image type. The result of this procedure seems to put in evidence that a pattern for the different structures does not exist, as can be seen on Figure 4.10.



**Figure 4.10 – Two examples of micro-MR images of the IVD converted into colour images.**

Therefore, it is possible to conclude that the resolution and contrast of the images, rather than the used segmentation methods, has a great influence on the geometry of the reconstructed segmented 3D models, and consequently will affect the generated FE meshes.

In this study several segmentation algorithms were presented and applied on a goat motion segment. As shown, these algorithms did not allow to achieve an automatic segmentation of the structures of the motion segment, especially regarding the intervertebral disc due to the low images resolution, lack of contrast between domains/structures and level of noise. Such difficulties made completely impossible to obtain a high level of confidence of the initial (real) geometry of the motion segment. Thus, a new procedure will be (Chapter 5) drawn and implemented in order to allow the analysis of the influence of the medical imaging resolution and

the FE mesh generation procedure on the quality and accuracy of the final 3D geometrical modelling by finite elements.

#### 4.5. Scheme of the segmentation procedure of an IVD

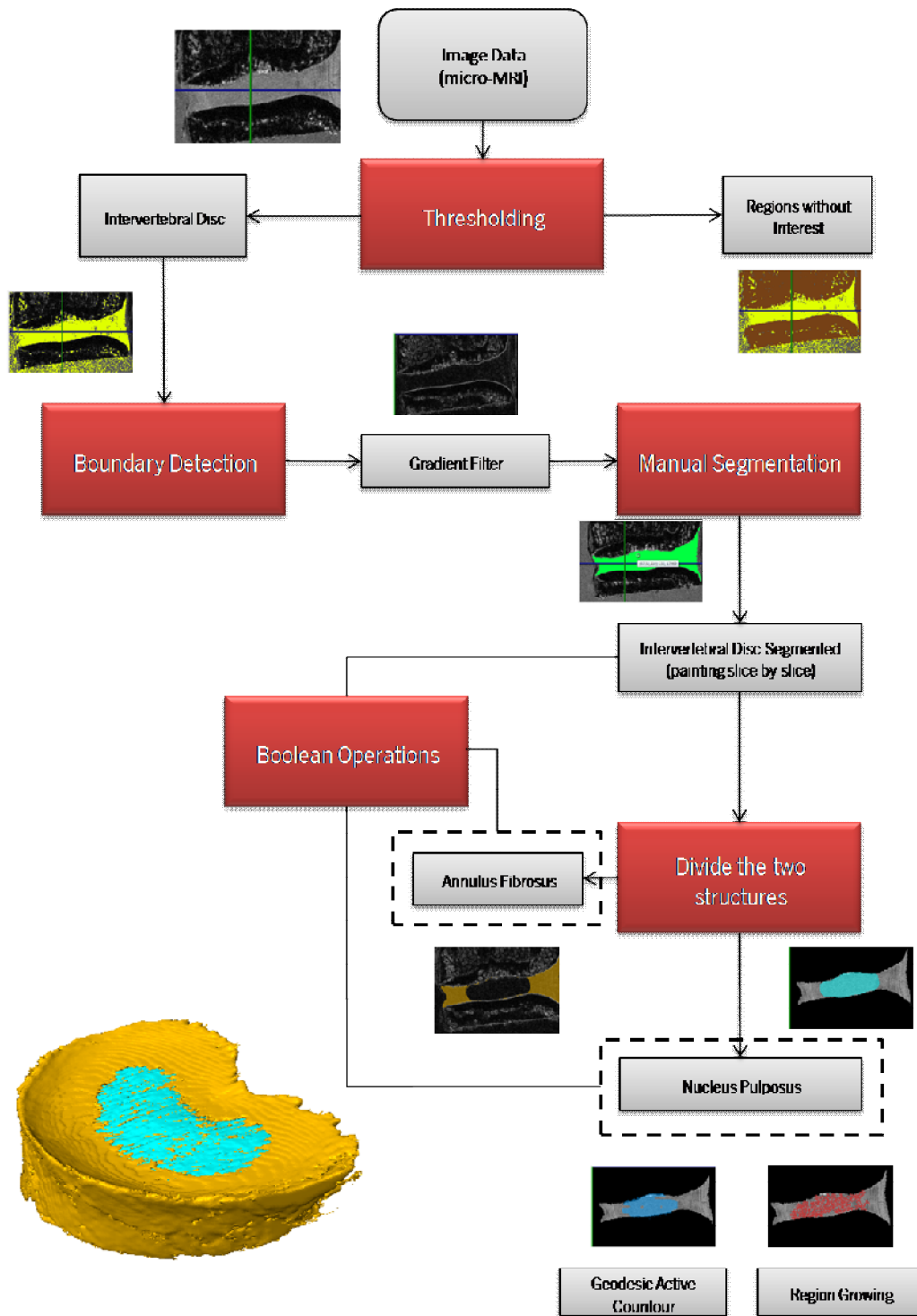


Figure 4.11 – Data flow diagram of the segmentation procedure applied to a motion segment based on micro-MR images.



---

## Chapter 5. Finite Element Mesh Generation

---

### 5.1. Introduction

The FE method is a powerful numerical technique often used to describe a huge variety of physical phenomena and solve practical cases, for which there is no analytical solution. Formulation of FE method requires the existence of an integral equation over a continuum medium, which is replaced by the sum of the elemental integrals over finite, simpler and discrete volumes, i.e., over finite elements.

An important requirement for the usage of the FE analysis is the existence of a FE mesh, which shall be representative of the continuum medium to be simulated and, simultaneously, have good quality, i.e., the finite elements shall be geometrically "healthy".

Thus, the FE mesh generation of an arbitrary domain involves the discretization of the multidimensional domain of the problem into small elements of simple geometry (finite elements), such as tetrahedral or hexahedral, for 3D problems. FE discretization allows achieving an accurate representation of complex geometries and solutions for each element, thus enabling processing multi-material domains and local geometrical enhancement, having in mind the improvement of gradients and the numerical solution obtained.

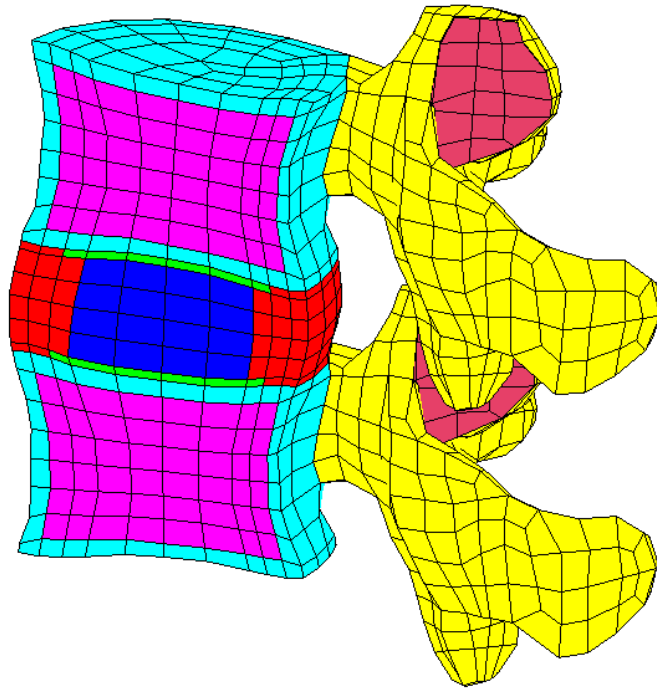
FE analysis (FEA) has been used in lumbar spine research (Table 1.1). It allows to examine the biomechanical behaviour of a healthy spine; to access the spinal performance when affected by a disease, degenerative changes, trauma, ageing or surgery; to investigate the influence of various spinal devices on spine behaviour and to assist in the design and development of new spinal implants. In most studies, tetrahedral finite elements are the most used in the automatic mesh generation procedures because they are compatible with all complex geometries of anatomical structures, i.e., any geometry can be decomposed in tetrahedral, what is not completely true in the case of other FE topologies. Generally, fine meshing is carried out at the edges near the surface with large curvature in order to closely resemble actual geometry.

The challenging point of this work is to generate an optimized FE mesh of a motion segment from a 3D voxel-based data, i.e., when the initial geometry is already discretized by voxels. The voxel-based 3D geometry is already an approximation of the real domain, which usually is not objectively known. From now on, an approach for automatic generation of tetrahedral FE meshes from 3D voxel-based models is presented in this chapter, and optimum procedure parameters investigated. The procedure for the final FE meshes generation of a motion segment involves three main steps: voxel-based geometric definition, application of a specific tetrahedral FE meshing procedure and FE mesh simplification.

The segmentation procedure described on the previous section should give origin to the voxel-based geometrical models from which the FE mesh generation should be applied. However, the aforesaid segmentation procedure, which was applied to a real goat medical imaging data, has a very important drawback as the real geometry of the characterized motion segment is not known. In this case, it is hard or even impossible to objectively quantify the quality of the FE mesh generation procedure, both in terms of quality of the FE mesh and mainly in terms of the approximation between the real geometry and the one described by the FE model. Thus, in order to overtake such difficulty, it was decided to generate a virtual set of already segmented medical images from a well-known initial geometry of a Human motion segment (available on the web from the ISB Finite Element Repository). Such virtualization procedure, which is briefly described in the next section, allowed a more objective evaluation of the FE mesh generation procedure from voxel-based geometrical models, the ultimate goal of this work.

## **5.2. Procedure for Virtual Voxel-based Model Generation**

The starting point for the generation of a virtual voxel-based segmented 3D geometrical model is the selection of a “real” geometry of a motion segment. In this study, a reference hexahedral FE mesh of a Human lumbar motion segment (Figure 5.1) was used. This mesh consists of seven different materials: the vertebral arches (yellow), the cortical bone (cyan), the cancellous bone (pink), the ligaments (dark pink), the annulus fibrosus (red), the nucleus pulposus (blue) and the cartilaginous endplate (green).

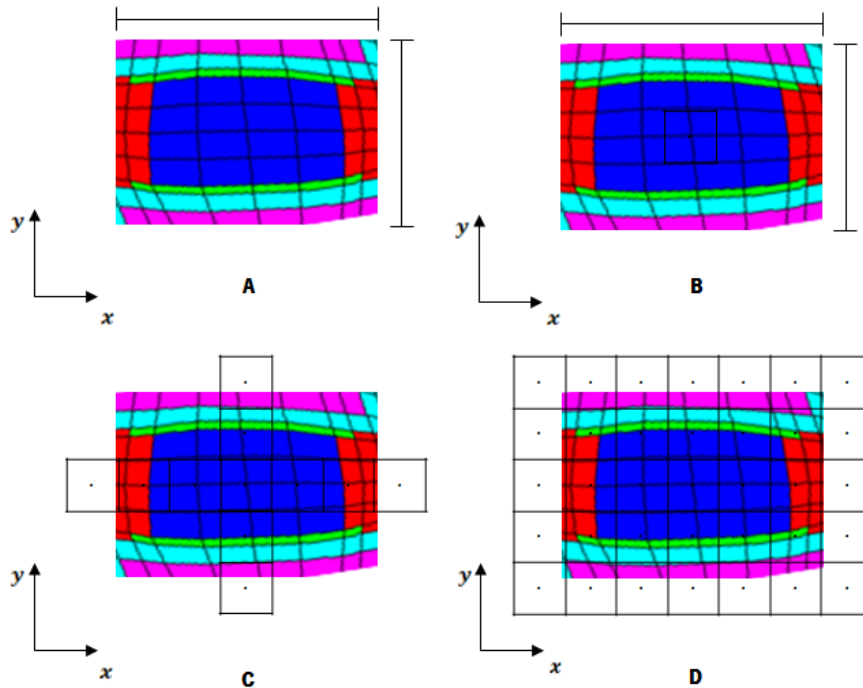


**Figure 5.1 – Reference FE mesh of the human lumbar motion segment (from the ISB Finite Element Repository).**

Assuming this geometry as being representative of a real motion segment, a FORTRAN code was developed to virtually generate the segmented 2D medical images. Such 2D segmented images were then used to carry out the 3D reconstruction of the voxel-based geometric model, which will be used for the FE mesh generation procedure.

In resume, this procedure consists of virtualization of medical images based on a known FE mesh to reconstruct a 3D model. Such virtualization technique has several advantages that shall be noticed. Among others, this technique allows to study the influence of some data acquisition parameters, such as image resolution and slice thickness and spacing between slices: 3D modelling virtualization was also used to study and understand the influence of image resolution on FE mesh generation procedures.

The virtualization procedure runs as follows: firstly the global  $(x, y, z)$  dimensions of the initial hexahedral FE mesh are determined. For this, the minimum and maximum coordinates are determined for each axis. The next step is to define the size of the voxel (dimensions in X, Y and Z), which will depend on the resolution specified by the 2D images. Given a 2D example, where a pixel corresponds to a voxel in 3D, a mesh domain and pixel size is defined and then a first pixel is generated in the centre of domain. Subsequently, the pixels and voxels structure is created for the entire 3D domain as shown in Figure 5.2.

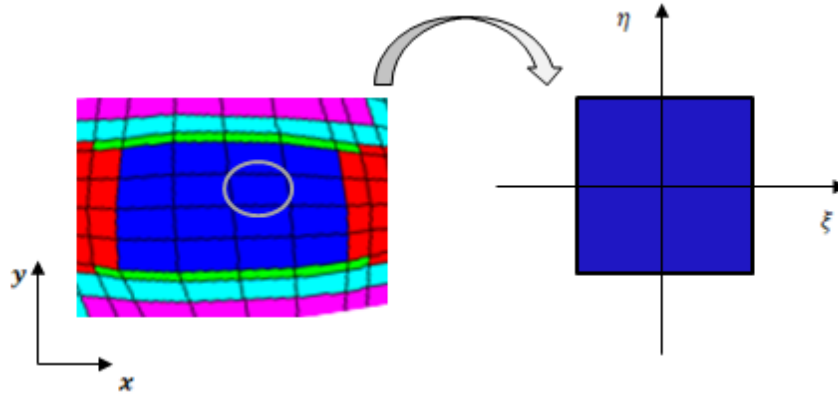


**Figure 5.2 - – A two-dimensional illustration of the (three-dimensional) creation of the grid of pixels (voxels).**

At this point one has the initial FE mesh and a 3D matrix of voxels. Next step is to determine the segmentation data of each voxel, i.e., the material ID to be assigned to each voxel. In order to identify the material ID to be assigned to each voxel, it is necessary to find the original finite element to which the centre of a given voxel belongs to. Once found, the material ID of the finite element is automatically assigned to the voxel, and so on for all voxels. At the end of this virtual imaging processing, a voxel-based 3D reconstructed geometrical model is obtained.

However, to find the material ID of each voxel is not straightforward. Each FE mesh consists on the following data: nodes and their spatial coordinates, finite elements and their connectivity and material ID assigned to each finite element. Since the original FE mesh is a hexahedral mesh, each element is defined by eight nodes, and each node has a given spatial organization inside the finite element. For the sake of simplicity, each finite element is formulated in a canonical (or natural) frame (Figure 5.3), and then the equivalence between Cartesian and canonical frame is derived from interpolation functions also known as shape functions which will allow to design the mathematical procedure to identify within each finite element a given voxel is. The developed algorithm is briefly outlined in the next section.



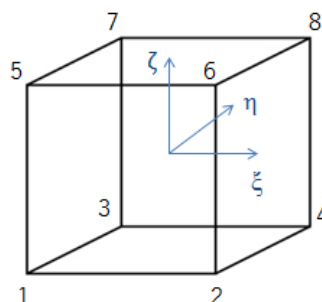


**Figure 5.3 – Schematic representation of the equivalence between Cartesian and canonical spaces of a given finite element.**

### 5.2.1. Voxel ID searching algorithm

Being  $\mathbf{x}$  the Cartesian coordinates of the central point of a given voxel, the mathematical problem can be shortened in order to find if this point is or is not inside of a given finite element of the original FE mesh. To solve this problem it is necessary to formulate the hexahedral finite element by defining its shape functions.

In finite elements theory, a finite element is formulated in canonical frame, and shape functions allow interpolating the nodal variables inside the spatial domain defined by the finite element. The challenge to postulate shape functions for plane quadrilaterals and three-dimensional hexahedra can be adequately met by bi-linear or tri-linear functions defined on a unit square or a unit cube for two- or three-dimensions, respectively, in  $(\xi_i, \eta_i)$  and  $(\xi_i, \eta_i, \zeta_i)$  canonical coordinates, as seen in Figure 5.4. A spatial mapping between canonical  $(\xi_i, \eta_i, \zeta_i)$  and Cartesian  $(x, y, z)$  frames is then locally defined at the finite element level, using the so-called isoparametric formulation.



**Figure 5.4 – Example of a 8-node hexahedron drawn in the canonical frame.**

In case of 8-noded hexahedron finite element, shape functions for each node are given by:

$$N_i(\xi, \eta, \zeta) = \frac{1}{8}(1 + \xi\xi_i)(1 + \eta\eta_i)(1 + \zeta\zeta_i) \quad (5.1)$$

where  $N_i$  is the shape function of the node  $i$ ,  $i = 1, 2 \dots 8$  is the node number,  $(\xi_i, \eta_i, \zeta_i)$  are the canonical coordinates of node  $i$ , and  $(\xi, \eta, \zeta)$  are the canonical coordinates of any point inside the finite element, i.e., within the condition  $-1 \leq \xi, \eta, \zeta \leq 1$ . The shape function of a given node assumes value of 1 in itself and 0 on the other ones.

From the nodal Cartesian coordinates of a given finite element it is possible to interpolate inside the element simply by using a shape function, such that:

$$\mathbf{x}(\xi, \eta, \zeta) = \sum_{i=1}^8 N_i(\xi, \eta, \zeta) \mathbf{x}^i \quad (5.2)$$

where  $\mathbf{x}^i$  is the Cartesian coordinates of node  $i$  and 8 the number of nodes of the 8-node hexahedron finite element.

Another interesting feature of finite elements theory is that one is able to determine the internal gradients by computing the derivatives of shape functions with respect to spatial position. Let  $P$  be an arbitrary property, with the following gradient:

$$\frac{\partial P}{\partial \mathbf{x}} = \frac{\partial P}{\partial \xi} \cdot \frac{\partial \xi}{\partial \mathbf{x}} \quad (5.3)$$

where

$$\frac{\partial P}{\partial \xi} = \frac{\partial}{\partial \xi} \left( \sum_{i=1}^8 N_i(\xi, \eta, \zeta) P^i \right) = \sum_{i=1}^8 \frac{\partial N_i(\xi, \eta, \zeta)}{\partial \xi} P^i \quad (5.4)$$

being the partial derivatives of the shape function with respect to natural coordinates defined as

$$\frac{\partial N_i}{\partial \xi}(\xi, \eta, \zeta) = \frac{1}{8} \xi_i (1 + \eta\eta_i)(1 + \zeta\zeta_i) \quad (5.5)$$

$$\frac{\partial N_i}{\partial \eta}(\xi, \eta, \zeta) = \frac{1}{8} \eta_i (1 + \xi\xi_i)(1 + \zeta\zeta_i) \quad (5.6)$$

$$\frac{\partial N_i}{\partial \zeta}(\xi, \eta, \zeta) = \frac{1}{8} \zeta_i (1 + \xi\xi_i)(1 + \eta\eta_i) \quad (5.7)$$

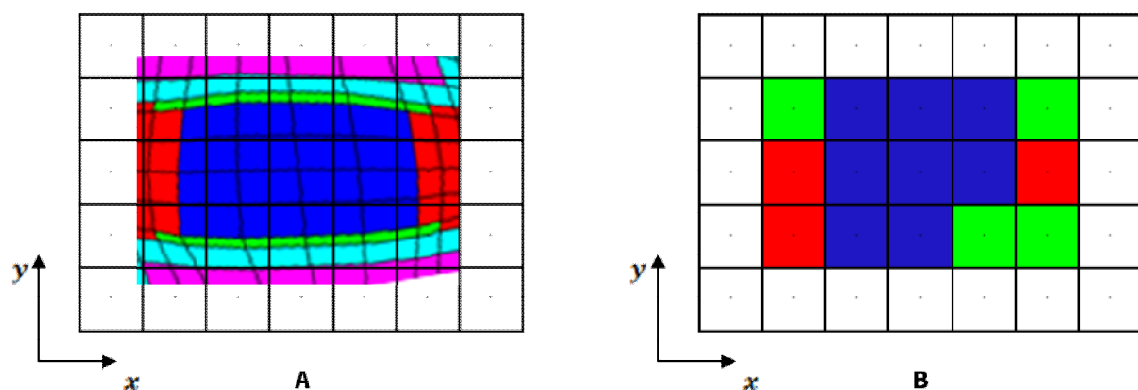
As mentioned initially, the mathematical problem of the voxel ID finding algorithm consists in finding if the central point of a given voxel is inside or outside of a given finite element of the original FE mesh. Being  $(x_c, y_c)$  the Cartesian coordinates of the central point of a given voxel, the mathematical problem can be reduced to solve the following nonlinear problem,

$$f(x, y) = 0 \quad (5.8)$$

which unknowns are the canonical coordinates  $(x, y)$ . However, since the relationship between  $f(x, y)$  and  $(x, y)$  is nonlinear, it is necessary to use an iterative numerical method, such as the Newton-Raphson method (see Appendix A). After determining the solution of the abovementioned problem, it is just needed to decide if point  $(x_c, y_c)$  is or is not inside the finite element under analysis, i.e., point  $(x_c, y_c)$  is inside the finite element if and only if

$$f(x_c, y_c) < -1 \quad (5.9)$$

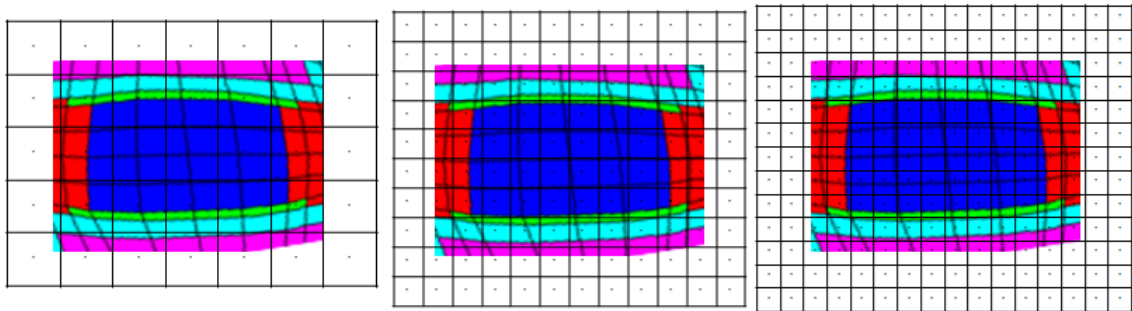
Finally, after finding that a given voxel is inside a given finite element, the next step is to identify the material ID of the element in order to assign the same ID to the voxel. An example of this procedure is shown in Figure 5.5. A matrix of pixels is superposed on the real domain, and the 2D medical images are virtually generated and segmented slice-by-slice. At the end of this procedure, the generated 3D voxel-based geometry will be used for the 3D FE mesh generation procedure.



**Figure 5.5 – Schematic of the virtual segmentation process on the pixels matrix.**

### 5.2.2. Voxel's Dimensions

The voxel's dimensions are one of the most important parameters regarding the quality of 3D geometrical reconstruction and later the representativeness and geometrical accuracy of generated 3D FE meshes. Voxel's dimensions are driven by the in-plane pixel's size and slice spacing, and shall depend on the geometry of anatomical regions under analysis. It is necessary to identify the tiniest geometrical detail to be taken into account, and thus to choose a voxel's dimensions small enough to capture such geometrical details. In the case of a motion segment and in particular in case of the Human motion segment under analysis the tiniest geometrical feature to be captured is the cartilaginous endplate (1 mm of thickness). As an example, different pixel's dimensions and respective matrices of pixels are shown in Figure 5.6.



**Figure 5.6 – Schematic of three different dimensions of pixels.**

In this work, three different voxel's dimensions were selected for analysis. The first two were selected based on the resolution of the two MRI image sets discussed in section 4.2, and the third one, a special case of the first one (cubic voxel assumption), was selected as control, in order to study the effect of the voxel's in-plane versus thickness ratio on the FE mesh generation procedure.

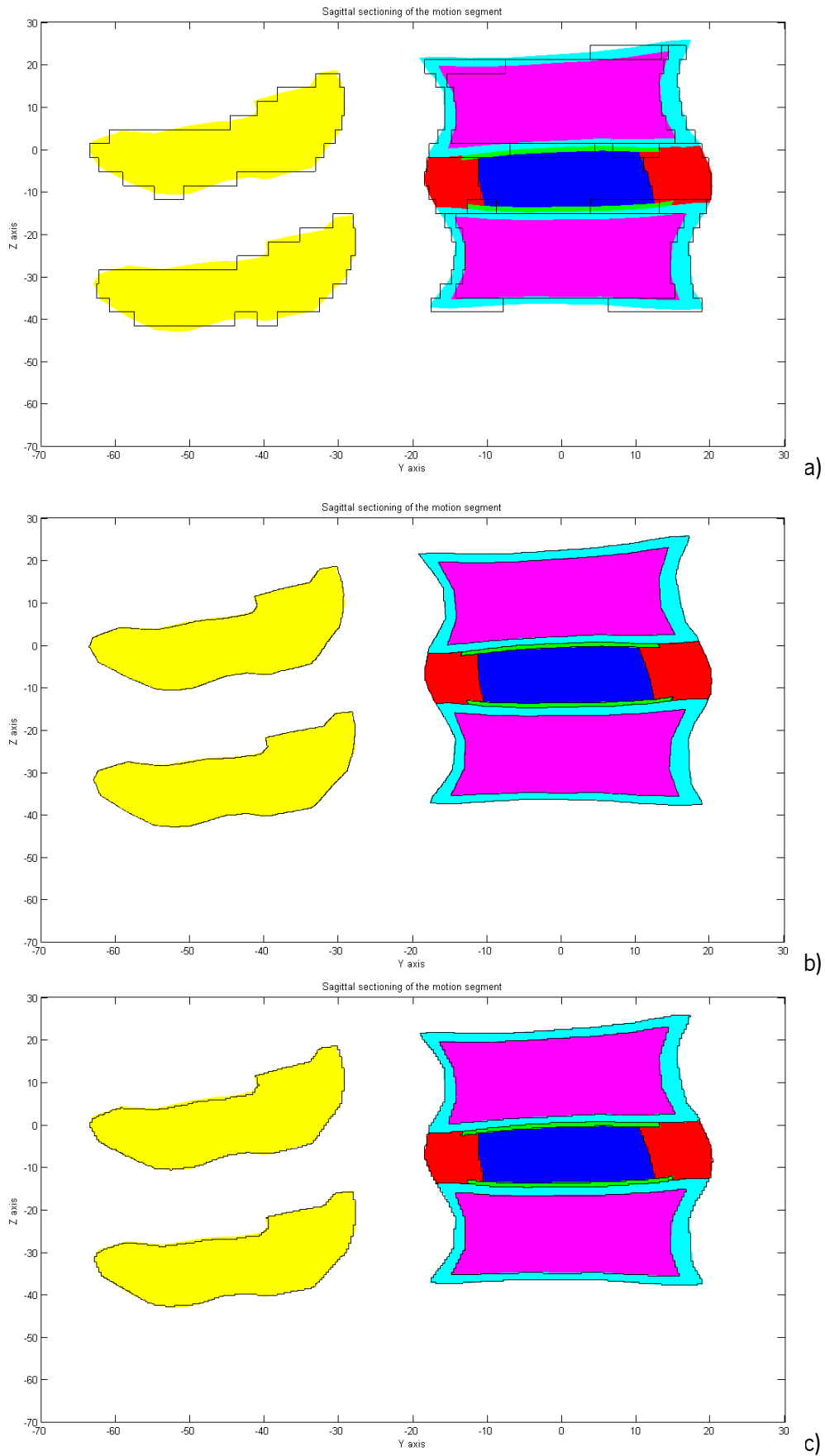
**Table 5.1 – Three different resolutions (voxel's dimension) of the voxel used in this study.**

Test	Resolution Type	Voxel's dimension [mm <sup>3</sup> ]
1	Low resolution (MR images)	0.3x0.3x3.3
2	High resolution (micro- MR images)	0.12x0.12x0.12
3	Control (cubic voxel)	0.3x0.3x0.3

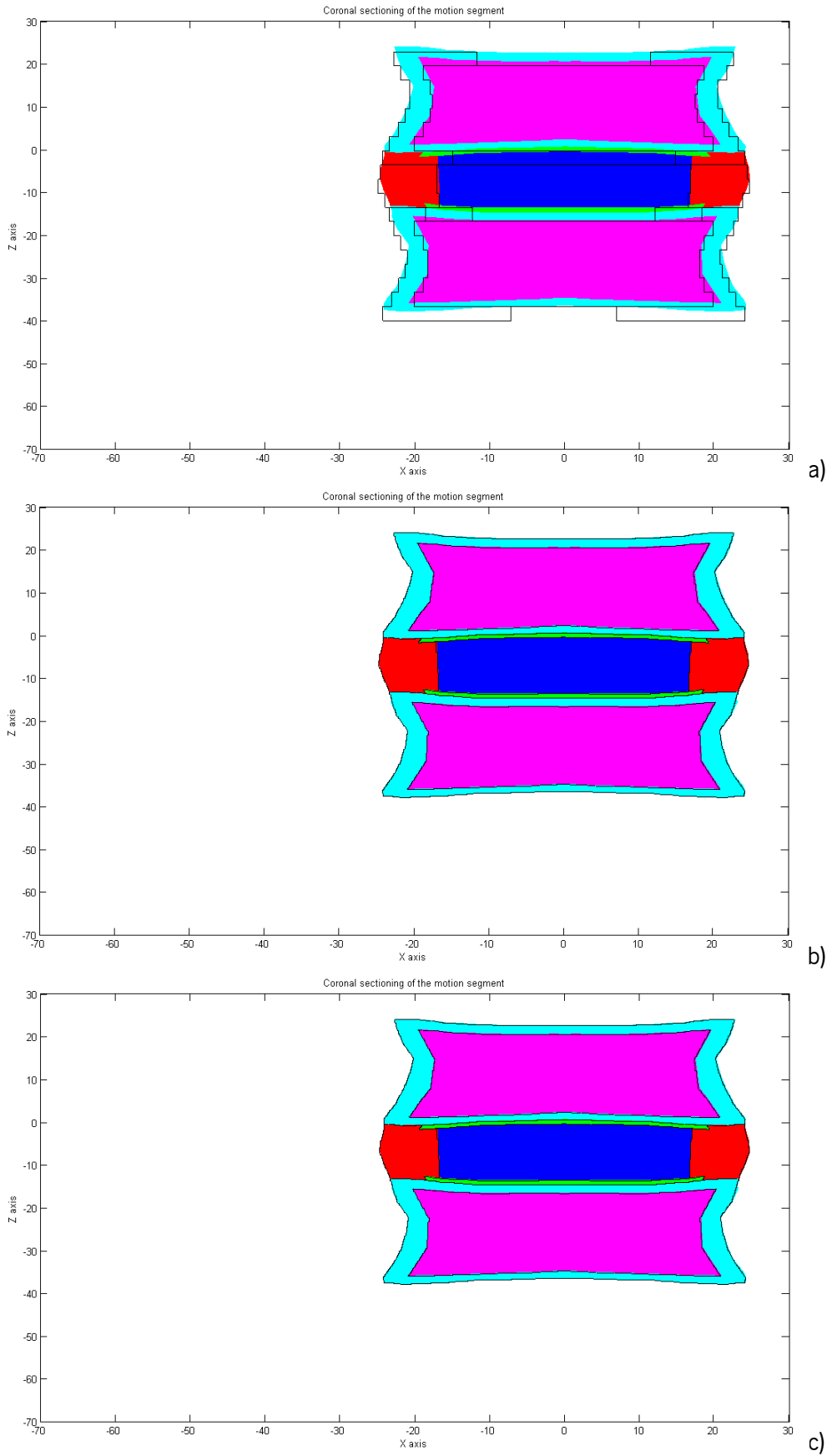
The first resolution is characterized by a very elongated voxel, while the other two resolutions are perfect cubic voxels. This may have some influence on the final 3D FE meshes generated regarding the study of data resolution on geometrical accuracy.

### **5.2.3. Analysis and Validation Tests**

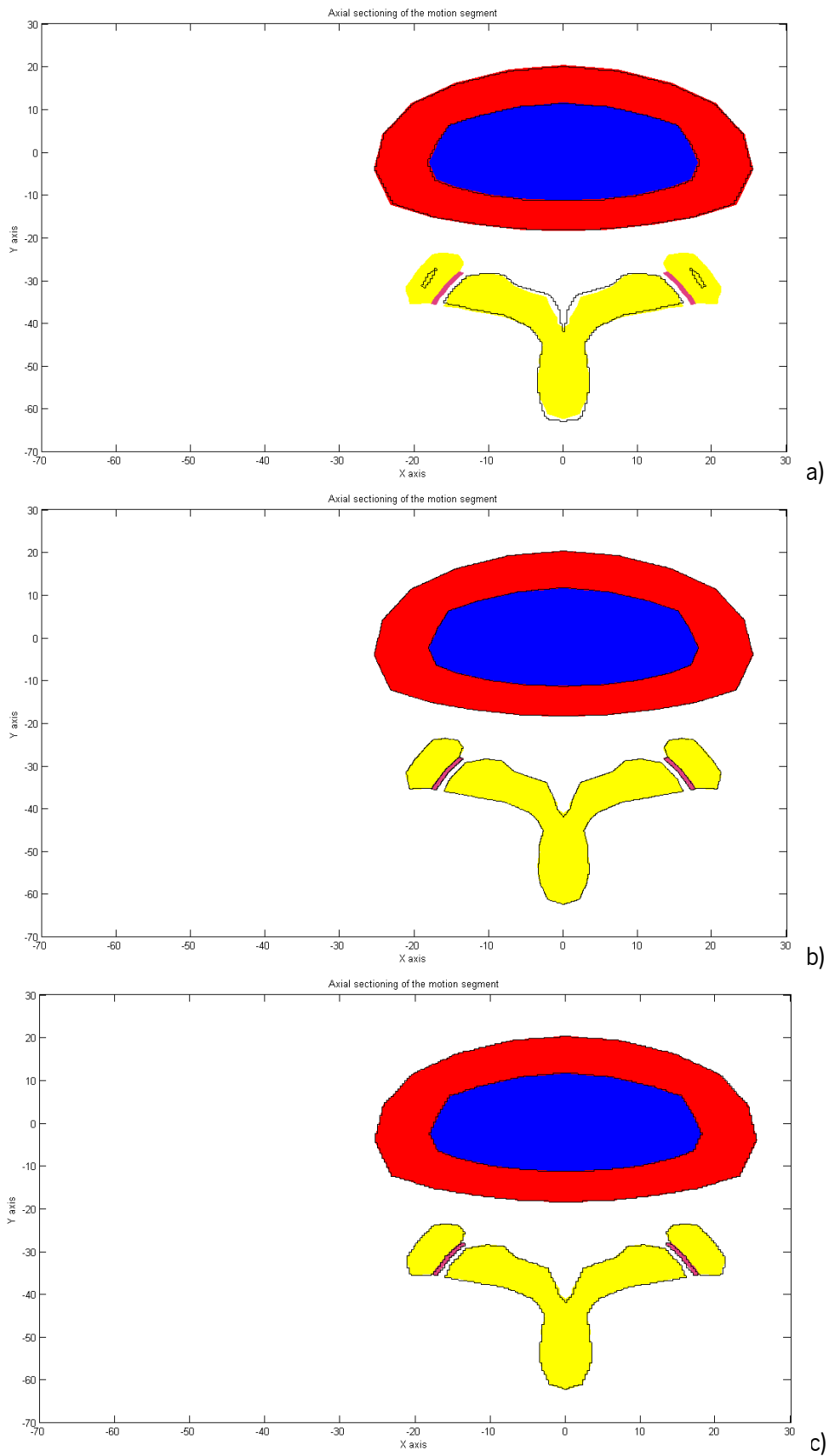
Using Matlab (Mathworks Inc., Natick, MA), a plane sectioning procedure was implemented in order to allow a visual analysis of the influence of image resolution on the 3D geometrical reconstruction by voxels. The next images show a comparison between the initial geometrical domain (the FE mesh shown in Figure 5.1) and the 3D voxel-based models obtained from the virtual voxel-based model generation procedure described previously. Figure 5.7, Figure 5.8, Figure 5.9 and Figure 5.10 show the results from the planes  $X=2$ ,  $Y=2$ ,  $Z=0$  and  $Z=-5$ , respectively.



**Figure 5.7 – Sagittal sectioning (X=2) of the motion segment with a) 0.3x0.3x3.3 b) 0.12x0.12x0.12 and c) 0.3x0.3x0.3 mm<sup>3</sup> of the voxel size.**

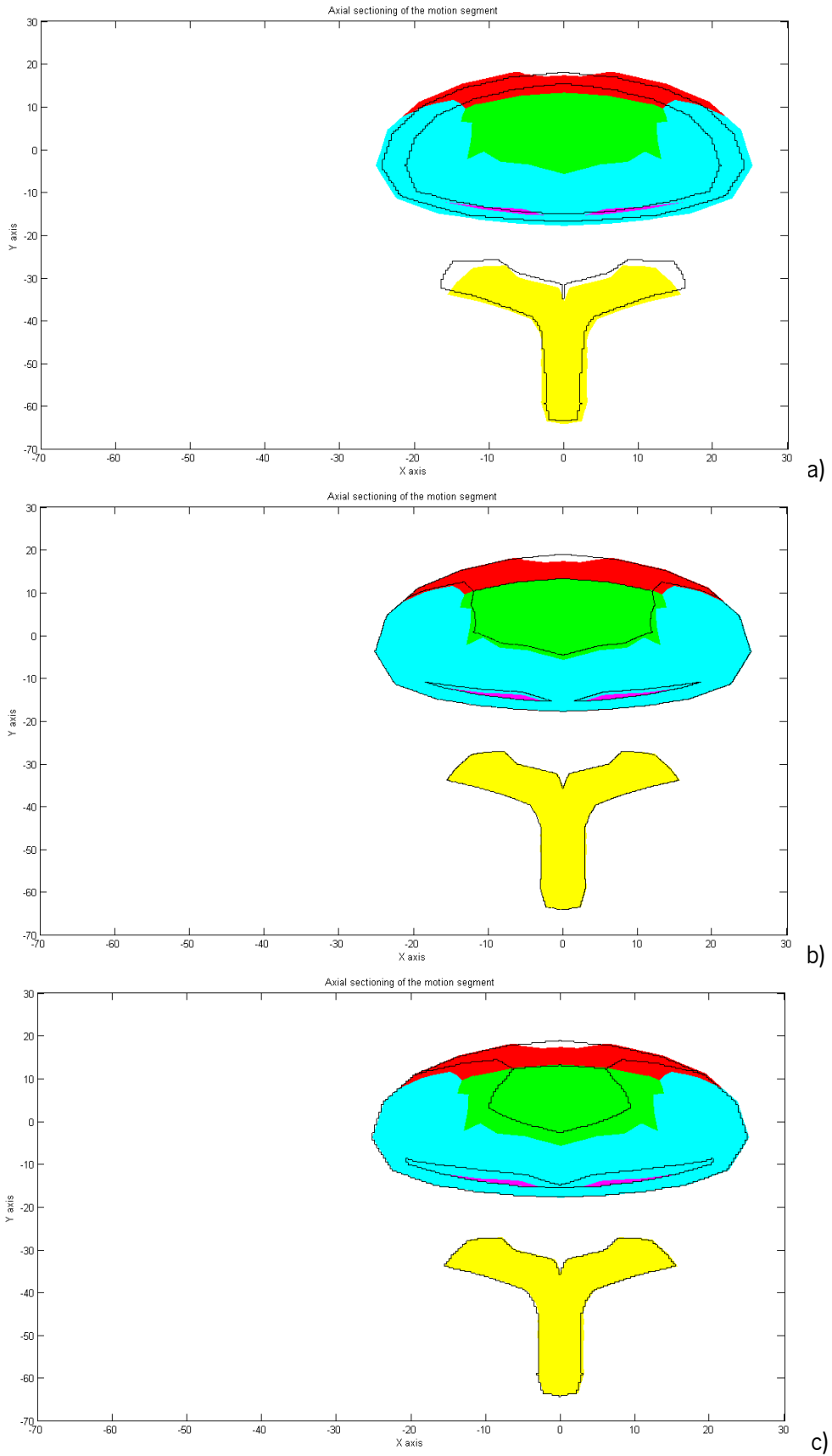


**Figure 5.8 - Coronal sectioning (Y=2) of the motion segment with a) 0.3x0.3x3.3 b) 0.12x0.12x0.12 and c) 0.3x0.3x0.3 mm<sup>3</sup> of the voxel size.**



**Figure 5.9 - Axial sectioning (Z= -5) of the motion segment with a) 0.3x0.3x3.3 b) 0.12x0.12x0.12 and c) 0.3x0.3x0.3 mm<sup>3</sup> of the voxel size.**





**Figure 5.10 - Axial sectioning ( $Z=0$ ) of the motion segment with a)  $0.3 \times 0.3 \times 3.3$  b)  $0.12 \times 0.12 \times 0.12$  and c)  $0.3 \times 0.3 \times 0.3 \text{ mm}^3$  of the voxel size.**

Table 5.2, Table 5.3 and Table 5.4 show the number of voxels and the volumes of the voxel and the initial geometries for different materials with the three different resolutions.

**Table 5.2 – Number of elements and volumes of the voxel and the initial geometry of different materials with 0.3x0.3x3.3 mm<sup>3</sup> of the voxel dimension.**

<b>Voxel dimension 0.3x0.3x3.3 mm<sup>3</sup></b>					
<b>Material</b>	<b>Number of Voxels</b>	<b>Vv, Volume of voxel [mm<sup>3</sup>]</b>	<b>Vi Volume of initial geometry [mm<sup>3</sup>]</b>	<b>Ratio Vv/Vi</b>	<b>Error</b>
Nucleus	25 537	7 584	8 154	0.930	-7%
Annulus	35 014	10 399	10 678	0.974	-3%
Endplate	11 156	3 313	1 552	2.135	113%
Cortical Bone	79 369	23 573	25 149	0.937	-6%
Cancellous bone	118 953	35 329	34 331	1.029	3%
Vertebrae	137 105	40 720	41 069	0.992	-1%
Ligaments	1 874	557	560	0.993	-1%
<b>TOTAL</b>	409 008	121 475	121 493	1.000	0%
<b>TOTAL IVD</b>	71 707	21 297	20 384	1.045	4%

**Table 5.3 - Number of elements and volumes of the voxel and the initial geometry of different materials with 0.12x0.12x0.12 mm<sup>3</sup> of the voxel dimension.**

<b>Voxel dimension 0.12x0.12x0.12 mm<sup>3</sup></b>					
<b>Material</b>	<b>Number of Voxels</b>	<b>Vv, Volume of voxel [mm<sup>3</sup>]</b>	<b>Vi Volume of initial geometry [mm<sup>3</sup>]</b>	<b>Ratio Vv/Vi</b>	<b>Error</b>
Nucleus	4 721 782	8 159	8 154	1.001	0%
Annulus	6 179 904	10 679	10 678	1.000	0%
Endplate	895 486	1 547	1 552	0.997	0%
Cortical Bone	14 563 557	25 166	25 149	1.001	0%
Cancellous bone	19 864 602	34 326	34 331	1.000	0%
Vertebrae	23 778 971	41 090	41 069	1.001	0%
Ligaments	324 258	560	560	1.000	0%
<b>TOTAL</b>	70 328 560	121 528	121 493	1.000	0%
<b>TOTAL IVD</b>	11 797 172	20 386	20 384	1.000	0%

**Table 5.4 - Number of elements and volumes of the voxel and the initial mesh for different materials with 0.3x0.3x0.3 mm<sup>3</sup> of the voxel dimension.**

<b>Voxel dimension 0.3x0.3x0.3 mm<sup>3</sup></b>					
<b>Material</b>	<b>Number of Voxels</b>	<b>Vv, Volume of voxel [mm<sup>3</sup>]</b>	<b>Vi Volume of initial geometry [mm<sup>3</sup>]</b>	<b>Ratio Vv/Vi</b>	<b>Error</b>
Nucleus	302 119	8 157	8 154	1.000	0%
Annulus	395 854	10 688	10 678	1.001	0%
Endplate	57 122	1 542	1 552	0.994	-1%
Cortical Bone	932 794	25 185	25 149	1.001	0%
Cancellous bone	1 270 592	34 306	34 331	0.999	0%
Vertebrae	1 521 782	41 088	41 069	1.000	0%
Ligaments	20 756	560	560	1.000	0%
<b>TOTAL</b>	4 501 019	121 528	121 493	1.000	0%
<b>TOTAL IVD</b>	755 095	20 388	20 384	1.000	0%

In Figure 5.7 (the sagittal plane) it is possible to observe that, when analysed the contours of the 3D voxel-based models, the elongated voxels ( $0.3 \times 0.3 \times 3.3 \text{ mm}^3$ ) are not able to describe accurately the overall structures. On the other hand, with the cubic voxel structure ( $0.12 \times 0.12 \times 0.12$  and  $0.3 \times 0.3 \times 0.3 \text{ mm}^3$ ), the global accuracy increases significantly. Similar observations and conclusions can be attained in case of coronal plane (Figure 5.8). Regarding the axial plane (Figure 5.9) a similar conclusion cannot be drawn given that, in this plane, the elongated shape of the voxels is “hidden”, i.e., in the axial plane is not able to distinguish between  $0.3 \times 0.3 \times 0.3 \text{ mm}^3$  and  $0.3 \times 0.3 \times 3.3 \text{ mm}^3$  voxel’s dimensions. Finally it is worth noting that in case of this last resolution, some structures are completely lost due to the coarse resolution along axial axis (in Figure 5.10 one can see that the endplate is not captured by 3D voxel-based geometry).

Table 5.2 shows a comparison between global (motion segment and IVD) and local (each sub-domain of the motion segment) volumes, determined from both the reference geometry and after segmentation for the three resolutions under analysis. The volumetric errors, in the case of the IVD for  $0.3 \times 0.3 \times 3.3 \text{ mm}^3$  voxel size, range between 3 and 7%, while in the case of the endplate is around of 113% due to the fact that the endplate is practically lost when voxel’s dimensions are too large. As referenced in section 5.1.2, voxel’s dimension greatly influences the outcome of the 3D model. For the other two case studies (Table 5.3 and Table 5.4) the error is practically null due to the similarity between the dimension of the voxel and the dimension of the anatomical regions being discretized.

### **5.3. Mesh Generation Procedure**

After 3D voxel-based geometrical reconstruction, the next step is the application of a specific FE mesh generation procedure. Several techniques for the FE mesh generation of anatomical structures have been developed and are proposed in the literature (see Table 1.1).

Based on the work of Labelle and Shewchuk (2007), a tetrahedral FE mesh was created keeping in mind the nature and smoothness of the boundaries of soft tissues. To use this grid-based algorithm, the first step is to superimpose a 3D grid structure (a body-centered lattice - BCC) over the 3D voxel-based model (Figure 5.11 in 2D). An octree subdivision can be introduced in the vicinity of volume boundaries.

The geometrical accuracy of the FE mesh depends on the size of the grid dimensions. Thus, the characteristic dimension of the isotropic grid shall be studied in detail in order to allow

the generation of a “good” FE mesh. Throughout this study four grid sizes were used: 0.25, 0.5, 1 and 2 mm (Table 5.5).

**Table 5.5 – Different parameters used in FE mesh generation.**

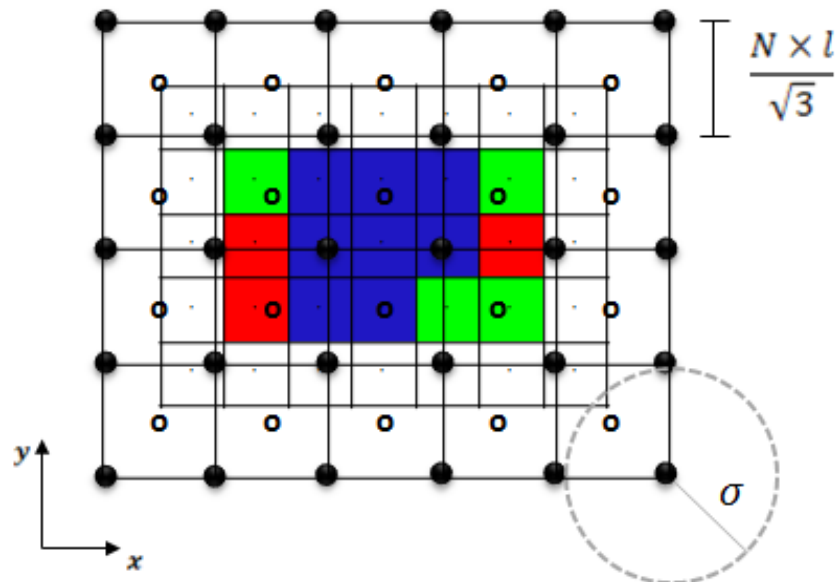
<b>Voxel's Dimension</b> [mm <sup>3</sup> ]	<b>Voxel Diagonal</b> [mm]	<b>Grid Size</b> [mm]	<b>N</b>	<b>σ1</b> <b>(0.5×N)</b>	<b>σ2</b> <b>(1.0×N)</b>	<b>σ3</b> <b>(2.0×N)</b>
<b>0.3x0.3x3.3</b>	3.33	0.25	0.13	0.07	0.13	0.26
		0.5	0.26	0.13	0.26	0.52
		1	0.52	0.26	0.52	1.04
		2	1.04	0.52	1.04	2.08
<b>0.12x0.12x0.12</b>	0.21	0.25	2.08	1.04	2.08	4.17
		0.5	4.17	2.08	4.17	8.33
		1	8.33	4.17	8.33	16.67
		2	16.67	8.33	16.67	33.33
<b>0.3x0.3x0.3</b>	0.52	0.25	0.83	0.42	0.83	1.67
		0.5	1.67	0.83	1.67	3.33
		1	3.33	1.67	3.33	6.67
		2	6.67	3.33	6.67	13.33

The FE mesh generation procedure requires two input parameters. The first one is N, which is associated with the definition of the grid size. Depending on the voxel's diagonal, it is possible to determine the value of N for each of the above mentioned grid sizes to be studied. Parameter N is a function of the required grid size and of the voxel diagonal *l*:

$$N = \frac{'Grid Size' \times \sqrt{3}}{l} \quad (5.10)$$

The second parameter required for the FE mesh generation is  $\sigma$ . This parameter defines the standard deviation of the gaussian distribution used for sampling. In other words, while N is the grid size and determines the size of the BCC lattice superposed on the voxelized data,  $\sigma$  defines the amount of neighbouring data that shall be taken into account for sampling the voxel data into the vertices and centre point of the grid's BCC lattice, i.e., the determination of the material ID to be assigned to each vertex and centre of the square in the grid. The weight to be assigned to each data decreases with distance in agreement with a Gaussian distribution, and the shape of Gaussian distribution depends on  $\sigma$ . When  $\sigma$  is very high, the area to be searched increases (the cut-off radius is  $2\sigma$ ), what usually introduces an additional smoothing of the boundaries, and consequently the loss of some anatomical geometrical features. On the other hand, when the value of  $\sigma$  is too small, the smoothing is less pronounced and, because the volume of data considered for sampling is small, sometimes the discrete voxel structure is wrongly captured. The values of

these two parameters ( $N$  and  $\sigma$ ) shall be carefully studied and defined in order to tune the FE mesh generation procedure for the case of a motion segment like the one proposed in this work.



**Figure 5.11 – Schematic of the mesh generation parameters.**

After the definition of the input parameters, the tetrahedral FE meshes are generated. The FE mesh generation procedure consists of four stages: sampling at grid points, computation of cutting points, warping of some grid points and, finally, the application, at the grid cell level, of the pre-defined stencils (geometric arrangement of a nodal group that relate to the point of interest by using a numerical approximation) for the generation of a uniform FE tetrahedral mesh. These four steps are briefly described below (and graphically shown in Figure 5.12):

*Sampling at grid points* – the scalar value for each vertex of the grid needs to be determined. Each vertex is associated with a mark: positive (inside), negative (outside), and zero (on the boundary). For interior grid cells, all vertices are labelled with ‘+’ mark. In case of multi-material domains, to each vertex is assigned the material ID of the domain in which the vertex shall be considered. Sampling algorithm is based on a Gaussian distribution centred on the vertex.

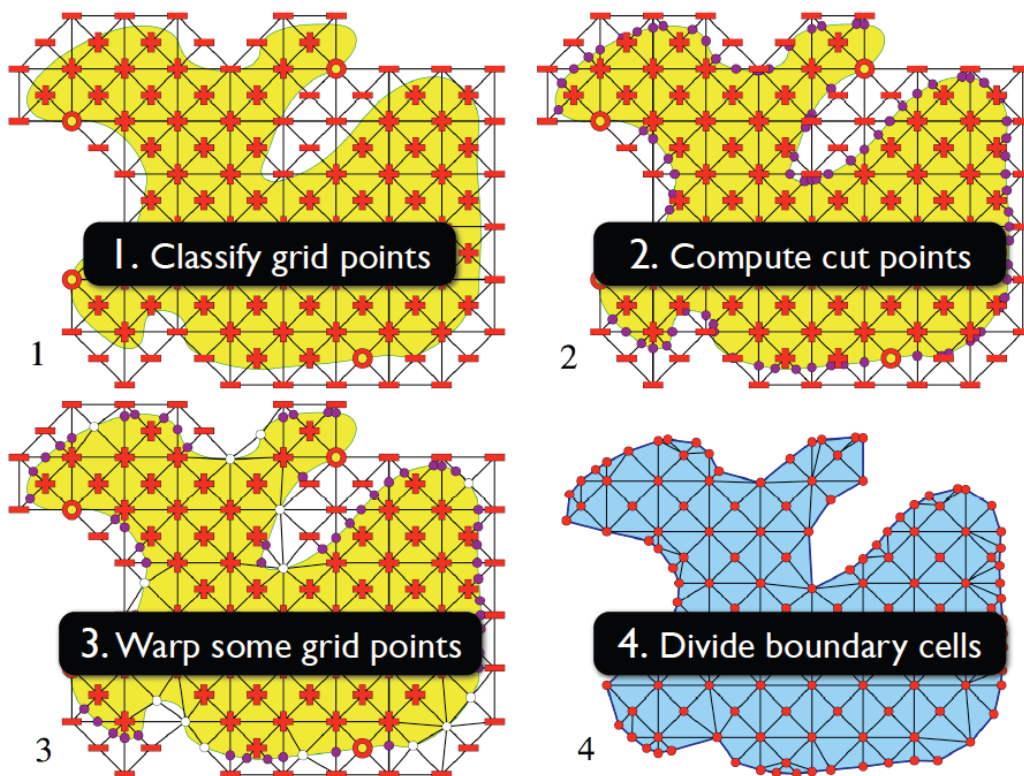
*Cutting points* – the computation of a cutting point is required when, for a given edge of the BCC grid, one point is positive and the other is negative (or in case of different material IDs assigned to the two points of an edge). In these cases it is necessary to compute the cutting point where the edge crosses the zero-surface or a given domain boundary.

*Warping of some grid points* – In some cases it may happens that a cutting point can exist very close to one point of the grid. In these cases, when a cutting point is too close to a given

vertex, one can assume that the cutting point violates the vertex and it is better to warp the grid by moving the vertex to a cut point.

*Divide grid cells* – For each BCC cell, and after sampling, cutting points evaluation and warping, it is necessary to generate the FE mesh. The technique is simply to use some predefined stencils to fill-in each grid cell with tetrahedra, while respecting the outside and internal boundaries previously identified. The choice of right stencil to be applied depends on the evaluation of signs and/or material IDs of the vertices of grid cell under evaluation. Exemplifying in 2D, there are cases in which the four vertices and the central point of the grid may generate more than four triangles with different materials.

Figure 5.12 shows the four different stages of the FE mesh generation process.



**Figure 5.12 – A two-dimensional illustration of the (three-dimensional) FE mesh generation algorithm.**

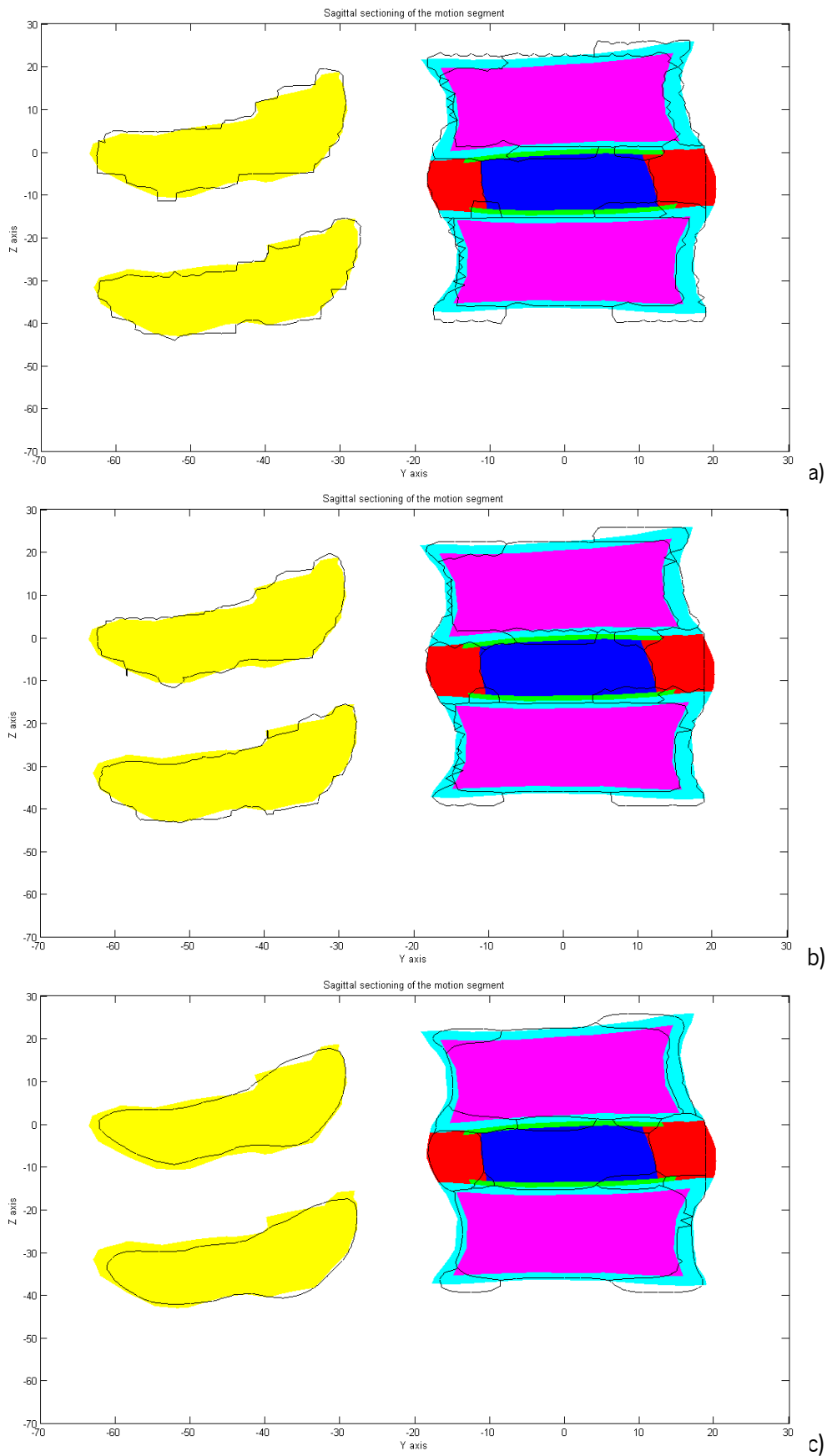
Finally, it should be noticed that the proposed algorithm does not guarantee the preservation of sharp features (edges and corners) presented in the input geometry. From the perspective of biological tissues, in which sharp features are anti-natural, this drawback is not significant. However, through a correct selection of parameters  $N$  and  $\sigma$ , one can optimize the FE mesh generation. In order to understand the role of parameter  $\sigma$  on the FE meshes generation, several values of  $\sigma$  were selected viz.,  $0.5 \times N$ ,  $1 \times N$  and  $2 \times N$ , as shown in Table 5.5. The logic

behind this choice is that the value of parameter  $\sigma$  must be coupled to the grid size, and thus in turn coupled to the value of  $N$ .

After defining FE meshing procedure, and after FE mesh generation, one will be able to statistically and geometrically compare the initial geometry with the one described by the FE meshes. This comparison shall allow understanding of the role of both the medical image resolution on the FE mesh generation and meshing parameters. Indeed, one aims to address some preliminary relevant results obtained with the proposed procedure. Thus, throughout next section the main results will be shown and discussed for the three resolution cases and selected input parameters.

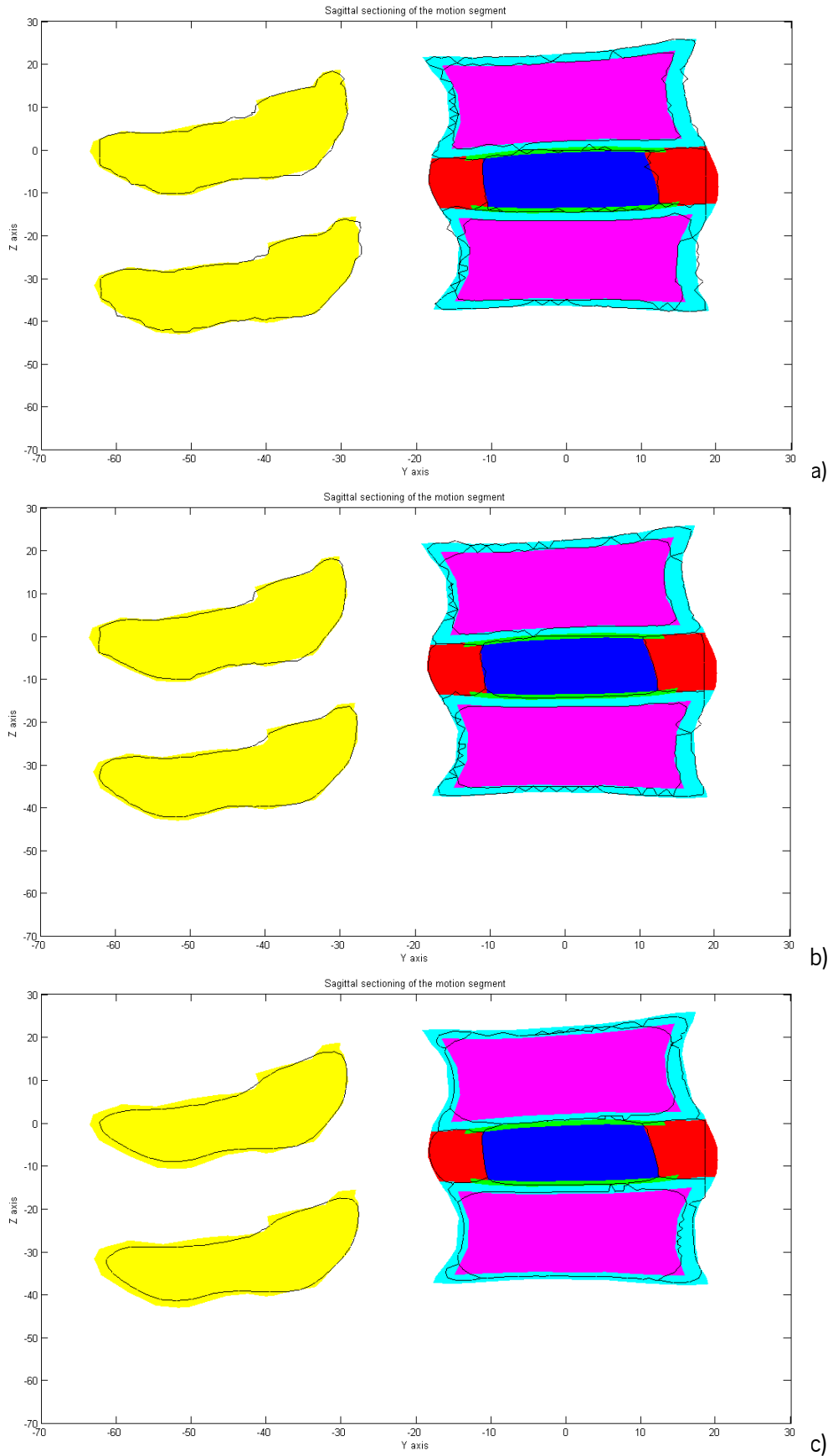
### **5.3.1. Analysis and Validation Tests**

Using the same aforesaid cross sections (introduced in Section 5.2.3) of the motion segment described by both voxel-based geometry and FE models, it is possible to compare these geometries with the one of reference, in order to understand the role of both grid size (parameter  $N$ ) and sampling (parameter  $\sigma$ ) on the FE mesh generation procedure. Figure 5.13 to Figure 5.21 shown the main results obtained for a sagittal plane cross section ( $X=2$ ) for the several FE meshes generated.

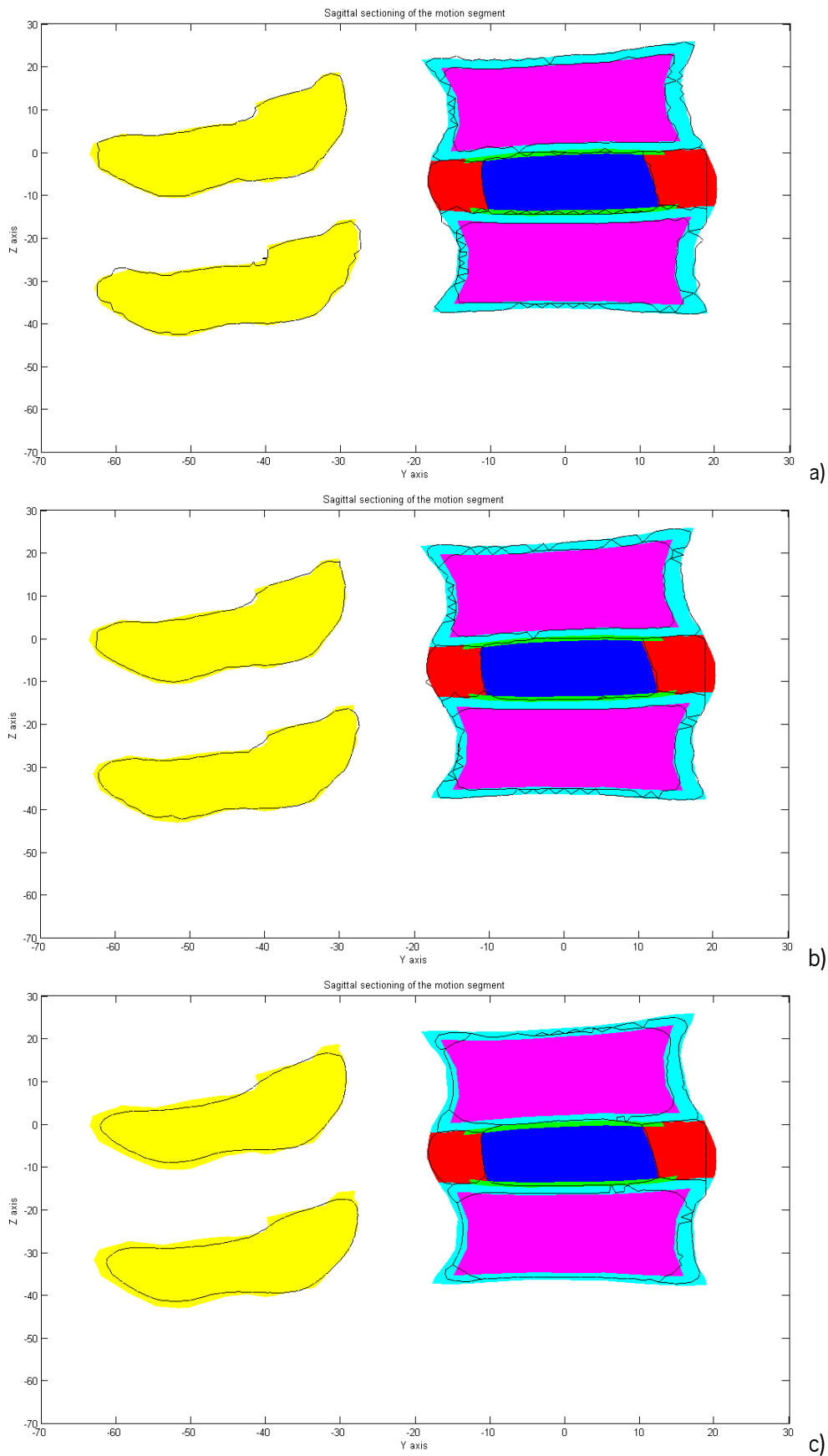


**Figure 5.13 – Sagittal cross section ( $X=2.0$  mm) of the initial geometry (coloured domains) and the contour of the FE mesh for the resolution of  $0.3 \times 0.3 \times 3.3$  mm<sup>3</sup>. The parameters used were a grid size of 2.0 mm (and N of 1.04) and  $\sigma$  of a) 0.52 b) 1.04 c) 2.08.**

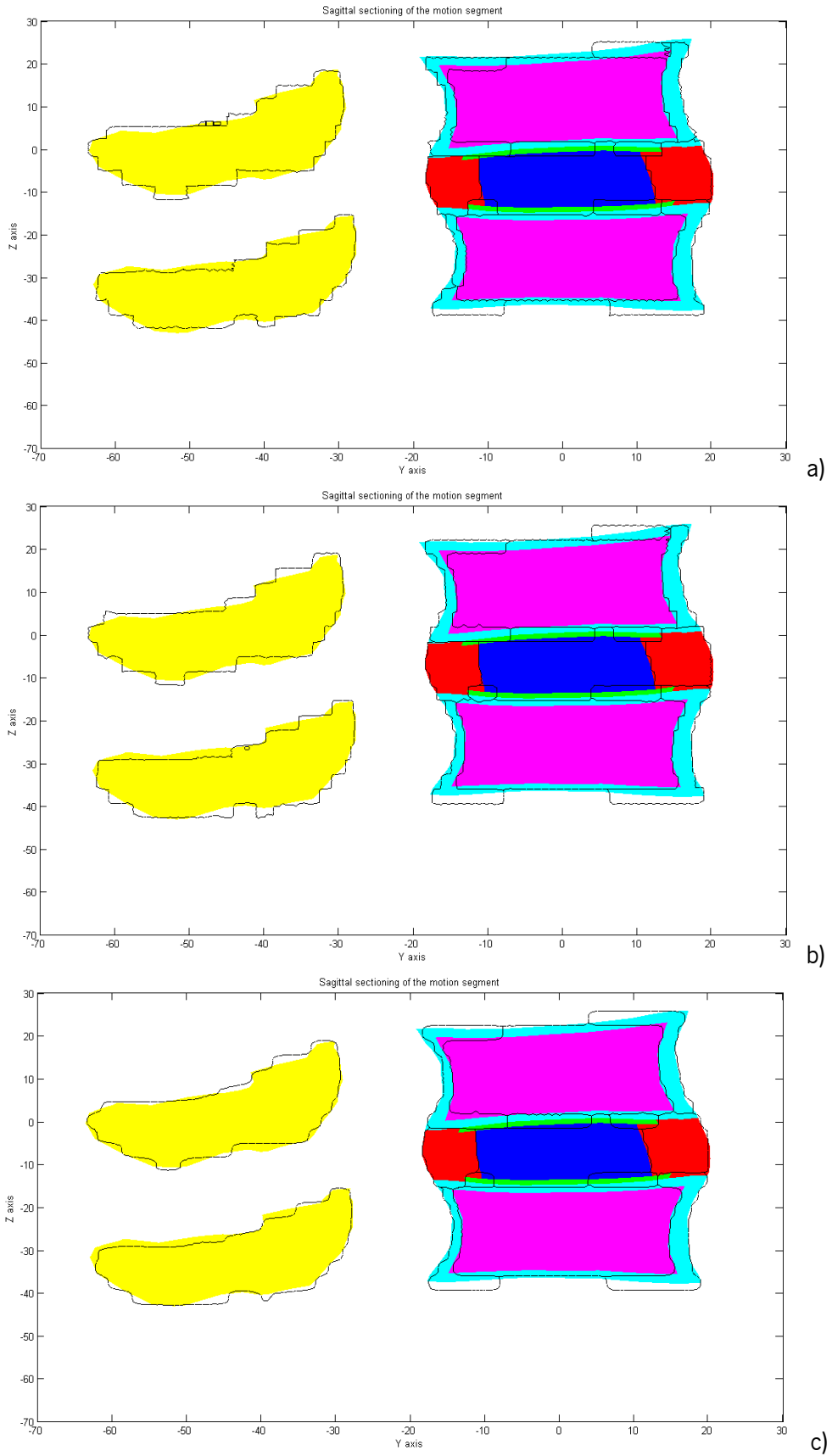




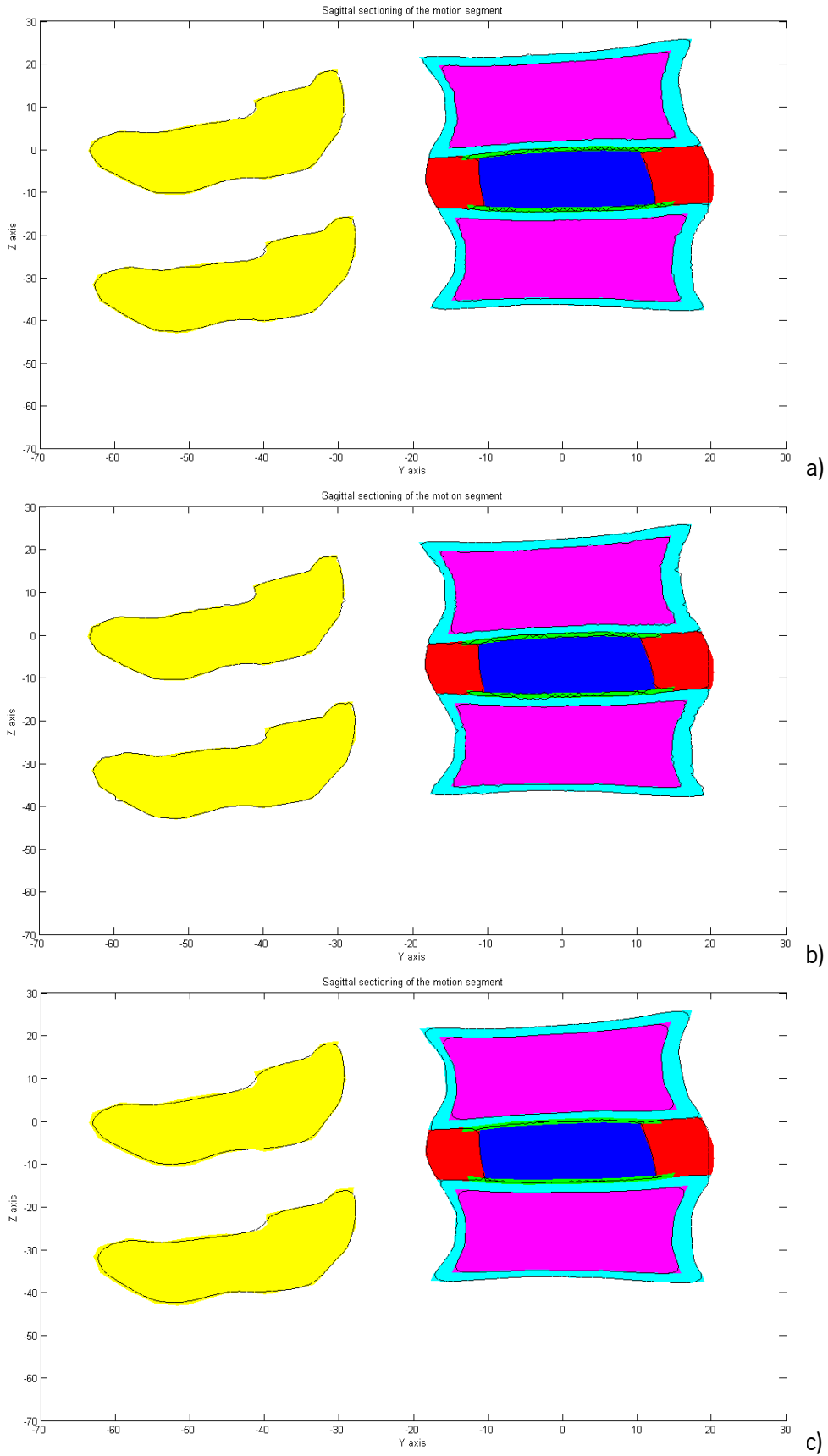
**Figure 5.14 - Sagittal cross section ( $X=2.0$  mm) of the initial geometry (coloured domains) and the contour of the FE mesh for the resolution of  $0.12 \times 0.12 \times 0.12$  mm<sup>3</sup>. The parameters used were a grid size of 2.0 mm (and N of 16.67) and  $\sigma$  of a) 8.33 b) 16.67 c) 33.33.**



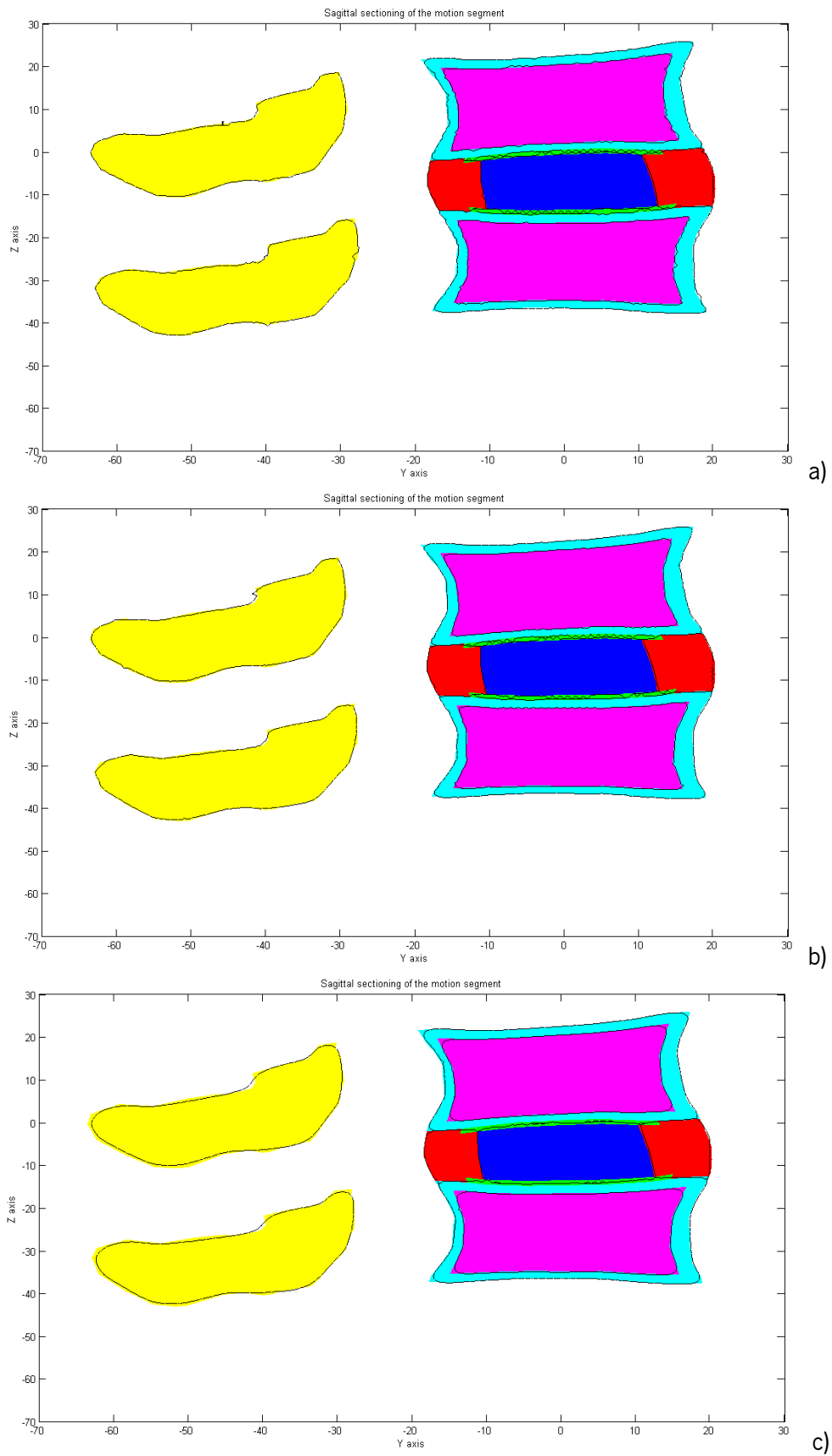
**Figure 5.15 – Sagittal cross section (X=2.0 mm) of the initial geometry (coloured domains) and the contour of the FE mesh for the resolution of 0.3x0.3x0.3 mm<sup>3</sup>. The parameters used were a grid size of 2.0 mm (and N of 6.67) and  $\sigma$  of a) 3.33 b) 6.67 c) 13.33.**



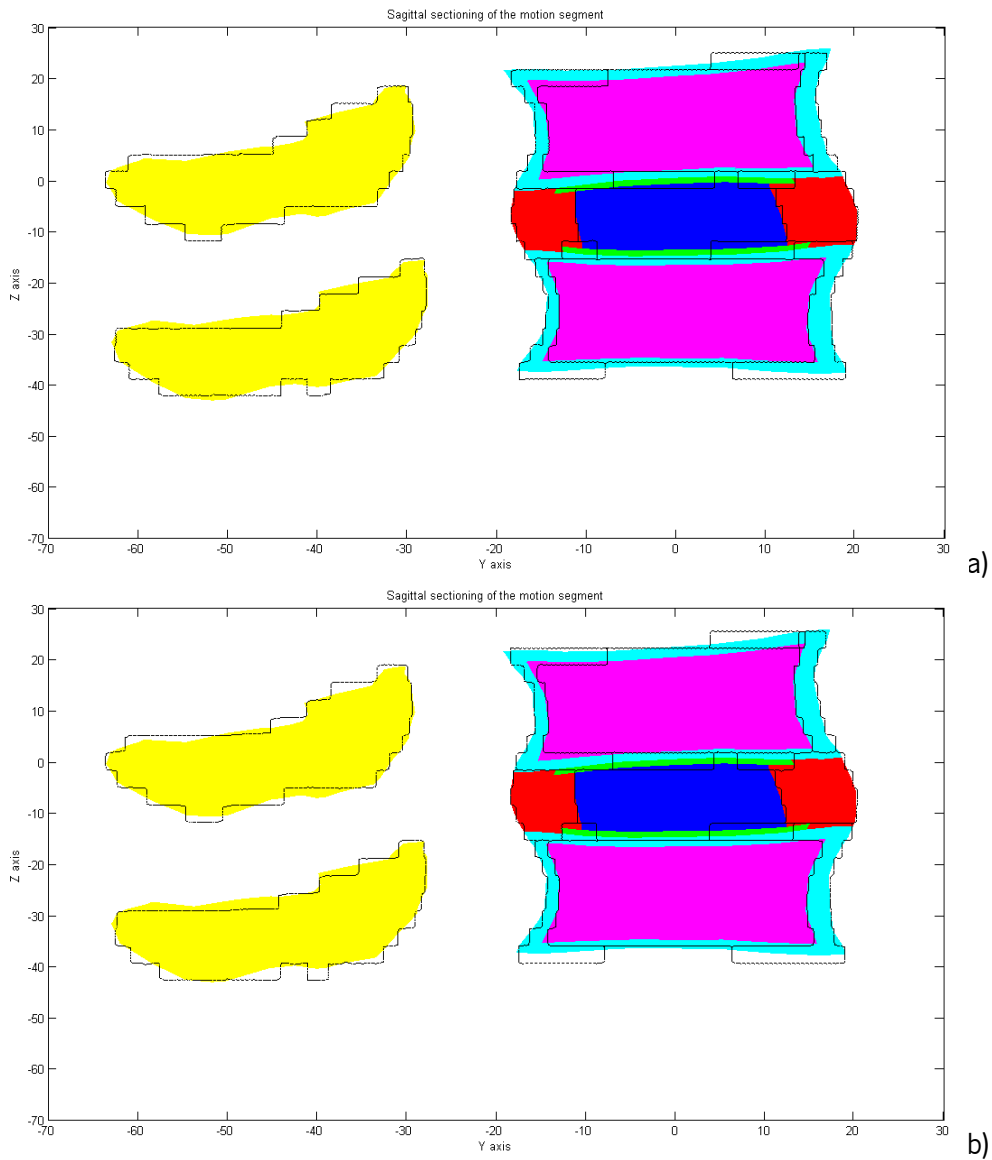
**Figure 5.16 – Sagittal cross section ( $X=2.0$  mm) of the initial geometry (coloured domains) and the contour of the FE mesh for the resolution of  $0.3 \times 0.3 \times 3.3$  mm<sup>3</sup>. The parameters used were a grid size of 1.0 mm (and N of 0.52) and  $\sigma$  of a) 0.26 b) 0.52 c) 1.04.**



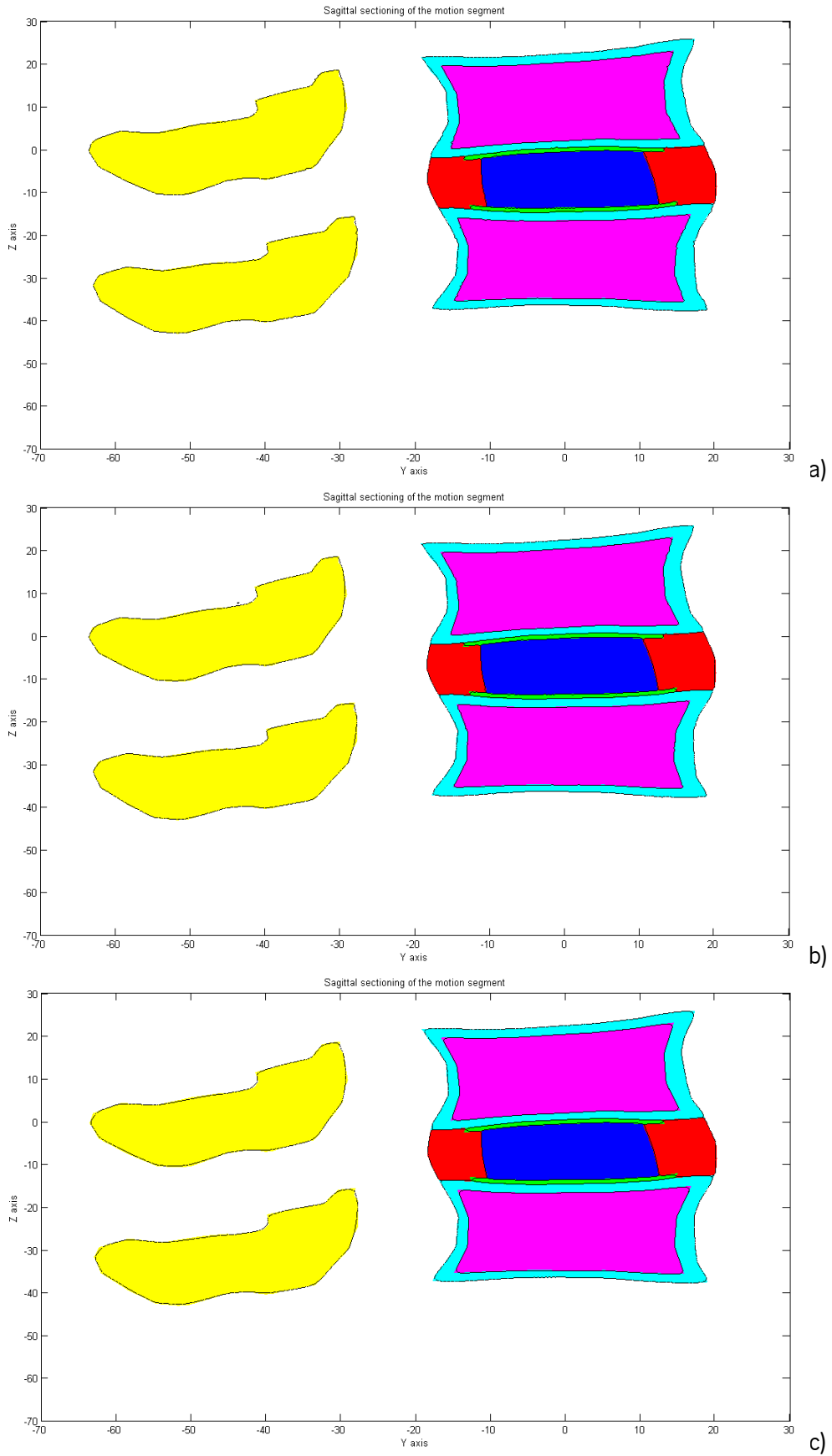
**Figure 5.17 - Sagittal cross section ( $X=2.0$  mm) of the initial geometry (coloured domains) and the contour of the FE mesh for the resolution of  $0.12 \times 0.12 \times 0.12$  mm<sup>3</sup>. The parameters used were a grid size of 1.0 mm (and N of 8.33) and  $\sigma$  of a) 4.17 b) 8.33 c) 16.67.**



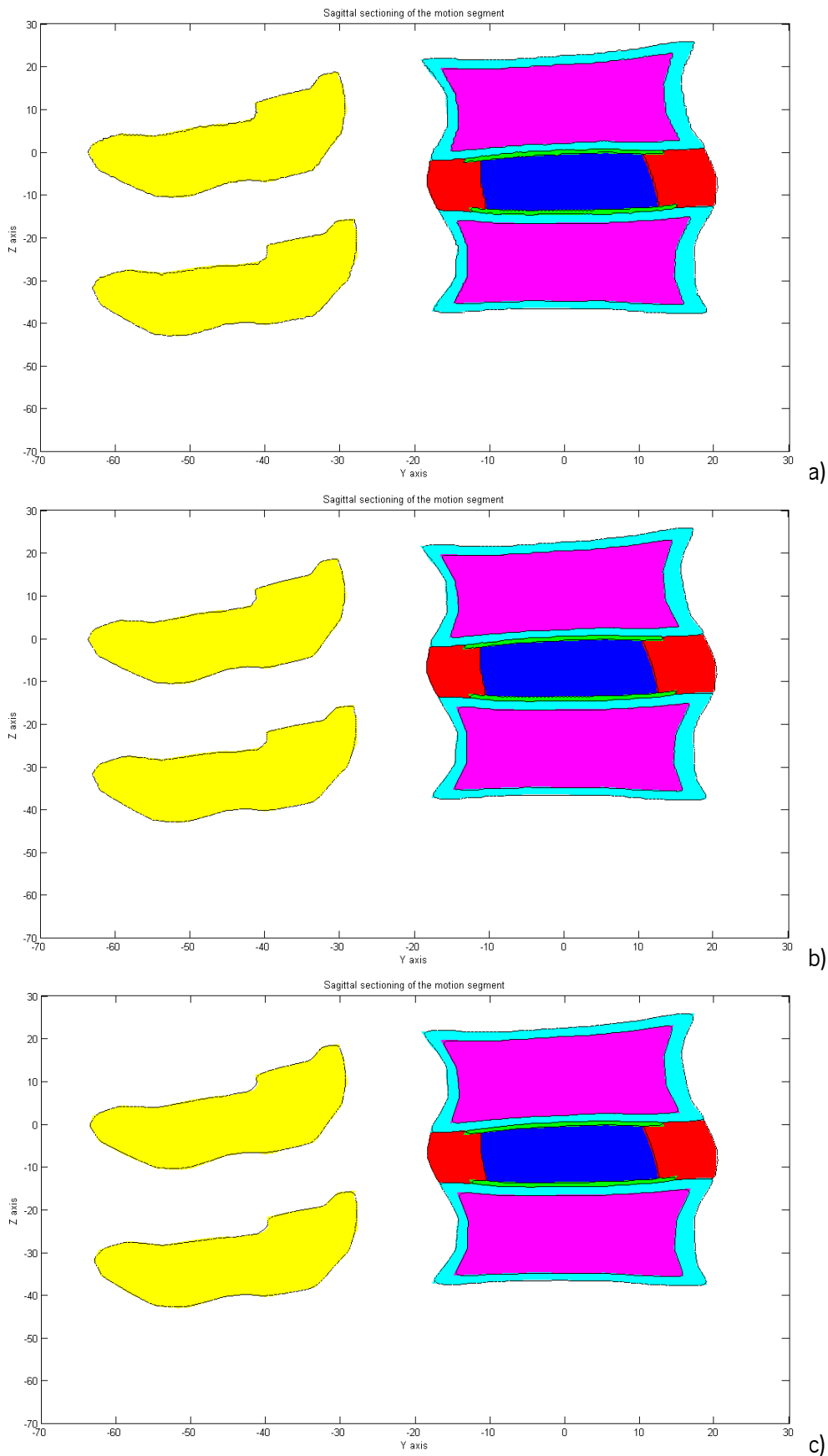
**Figure 5.18 – Sagittal cross section ( $X=2.0$  mm) of the initial geometry (coloured domains) and the contour of the FE mesh for the resolution of  $0.3 \times 0.3 \times 0.3$  mm<sup>3</sup>. The parameters used were a grid size of 1.0 mm (and N of 3.33) and  $\sigma$  of a) 1.67 b) 3.33 c) 6.67.**



**Figure 5.19 – Sagittal cross section ( $X=2.0$  mm) of the initial geometry (coloured domains) and the contour of the FE mesh for the resolution of  $0.3 \times 0.3 \times 0.3$  mm<sup>3</sup>. The parameters used were a grid size of 0.5 mm (and  $N$  of 0.26) and  $\sigma$  of a) 0.26 b) 0.52.**



**Figure 5.20 – Sagittal cross section (X=2.0 mm) of the initial geometry (coloured domains) and the contour of the FE mesh for the resolution of 0.12x0.12x0.12 mm<sup>3</sup>. The parameters used were a grid size of 0.5 mm (and N of 4.17) and  $\sigma$  of a) 2.08 b) 4.17 c) 8.33.**



**Figure 5.21 – Sagittal cross section ( $X=2.0$  mm) of the initial geometry (coloured domains) and the contour of the FE mesh for the resolution of  $0.3 \times 0.3 \times 0.3$  mm<sup>3</sup>. The parameters used were a grid size of  $0.5$  mm (and  $N$  of  $1.67$ ) and  $\sigma$  of a)  $0.83$  b)  $1.67$  c)  $3.33$ .**



Table 5.6, Table 5.7 and Table 5.8 show a summary of the global (full motion segment and IVD) and local (each structure or material) volumes on the FE meshes generated for the three different grid sizes and for each set of input parameters (as listed in Table 5.5). The volumetric error (initial *versus* final) for each global or local domain is calculated as:

$$Error (\%) = \frac{(Final Volume - Initial Volume)}{Initial Volume} \quad (5.11)$$

**Table 5.6 – Volumes of the different materials of the generated FE meshes with a voxel dimension of 0.3x0.3x3.3 mm<sup>3</sup>.**

Voxel's Dimension [mm <sup>3</sup> ]		0.3x0.3x3.3																									
Grid Dimension [mm]	0.25			0.5			1			2																	
N	0.13			0.26			0.52			1.04																	
σ	0.065	0.13	0.26	0.13	0.26	0.52	0.26	0.52	1.04	0.52	1.04	2.08															
Number of Nodes [x10E6]	17.3			2.3			2.3			0.31																	
Number of Elements [x10E6]	99.0			12.8			12.7			1.6																	
Volume [mm <sup>3</sup> ]																											
<b>Vertebrae</b>	41 508			41 591			42 168			41 408			42 235			42 060			41 941			41 671			39 144		
Error (%)	1%			1%			3%			1%			3%			2%			2%			1%			-5%		
<b>Cortical Bone</b>	23 996			23 953			24 384			24 046			24 506			24 491			23 573			23 341			21 431		
Error (%)	-5%			-5%			-3%			-4%			-3%			-3%			-6%			-7%			-15%		
<b>Cancellous Bone</b>	35 913			35 905			36 698			35 583			36 490			36 780			37 802			37 287			37 246		
Error (%)	5%			5%			7%			4%			6%			7%			10%			9%			8%		
<b>Ligaments</b>	563			549			389			78			25			0			2			0			0		
Error (%)	0%			-2%			-31%			-86%			-96%			0			-100%			0			0		
<b>Annulus Fibrosus</b>	10 873			10 863			10 873			10 854			10 810			10 824			10 641			10 707			10 720		
Error (%)	2%			2%			2%			2%			1%			1%			0%			0%			0%		
<b>Endplate</b>	3 461			3 469			3 429			3 443			3 456			3 352			3 161			3 270			2 622		
Error (%)	123%			123%			121%			122%			123%			116%			104%			111%			69%		
<b>Nucleus Pulposus</b>	7 925			7 923			7 915			7 923			7 892			7 880			7 910			7 857			7 931		
Error (%)	-3%			-3%			-3%			-3%			-3%			-3%			-3%			-4%			-3%		
<b>IVD</b>	22 259			22 256			22 217			22 220			22 158			22 056			21 712			21 834			21 274		
Error (%)	9%			9%			9%			9%			9%			8%			7%			7%			4%		
<b>Total</b>	124 240			124 254			125 856			123 335			12 5413			125 387			125 030			124 132			119 094		
Error (%)	2%			2%			4%			2%			3%			3%			3%			2%			-2%		

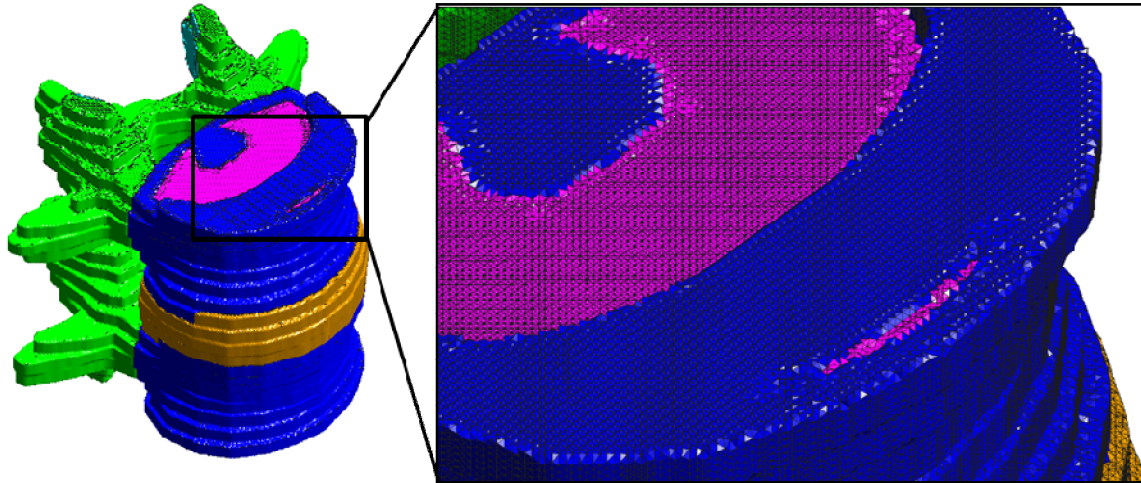
**Table 5.7 – Volumes of the different materials of the final FE mesh with a voxel dimension of 0.12x0.12x0.12 mm<sup>3</sup>.**

<b>Voxel's Dimension [mm<sup>3</sup>]</b>	<b>0.12x0.12x0.12</b>											
<b>Grid Dimension [mm]</b>	<b>0.25</b>			<b>0.5</b>			<b>1</b>			<b>2</b>		
<b>N</b>	2.08			4.17			8.33			16.67		
<b>σ</b>	1.04	2.08	4.17	2.08	4.17	8.33	4.17	8.33	16.67	8.33	16.67	33.33
<b>Number of Nodes [x10E6]</b>	16.6	16.6	16.6	2.1	2.2	2.2	0.3	0.3	0.3	0.04	0.04	0.04
<b>Number of Elements [x10E6]</b>	95.8	95.9	95.8	12.0	12.0	12.1	1.5	1.5	1.5	1.8	1.9	1.9
<b>Volume [mm<sup>3</sup>]</b>												
<b>Vertebrae</b>	41 258	41 237	41 195	41 231	41 176	41 100	41 299	41 195	40 648	40 584	40 137	38 072
Error (%)	0%	0%	0%	0%	0%	0%	1%	0%	-1%	-1%	-2%	-7%
<b>Cortical Bone</b>	25 277	25 276	25 285	25 283	25 314	25 373	25 298	25 611	26 039	23 833	23 610	19 378
Error (%)	1%	1%	1%	1%	1%	1%	1%	2%	4%	-5%	-6%	-23%
<b>Cancellous Bone</b>	34 465	34 451	34 419	34 449	34 404	34 313	34 448	34 343	34 043	35 256	35 213	36 122
Error (%)	0%	0%	0%	0%	0%	0%	0%	0%	-1%	3%	3%	5%
<b>Ligaments</b>	560	560	550	529	536	390	47	20	0	3	0	0
Error (%)	0%	0%	-2%	-6%	-4%	-30%	-92%	-96%	0	-99%	0	0
<b>Endplate</b>	1 549	1 551	1 543	1 500	1 525	1 458	1 026	793	30	213	1	0
Error (%)	0%	0%	-1%	-3%	-2%	-6%	-34%	-49%	-98%	-86%	-100%	0
<b>Annulus Fibrosus</b>	10 723	10 719	10 720	10 715	10 709	10 724	10 731	107 46	10 741	10 447	10 577	10 585
Error (%)	0%	0%	0%	0%	0%	0%	0%	1%	1%	-2%	-1%	-1%
<b>Nucleus Pulposus</b>	8 195	8 189	8 186	8 206	8 189	8 186	8 376	8 444	8 718	8 866	8 817	9 152
Error (%)	1%	0%	0%	1%	0%	0%	3%	4%	7%	9%	8%	12%
<b>IVD</b>	20 467	20 459	20 448	20 421	20 423	20 368	20 133	199 83	19 489	19 527	19 395	19 737
Error (%)	0%	0%	0%	0%	0%	0%	-1%	-2%	-4%	-4%	-5%	-3%
<b>Total</b>	122 027	121 983	121 898	121 913	121 853	121 543	121 225	121 152	120 219	119 203	118 356	113 309
Error (%)	0%	0%	0%	0%	0%	0%	0%	0%	-1%	-2%	-3%	-7%

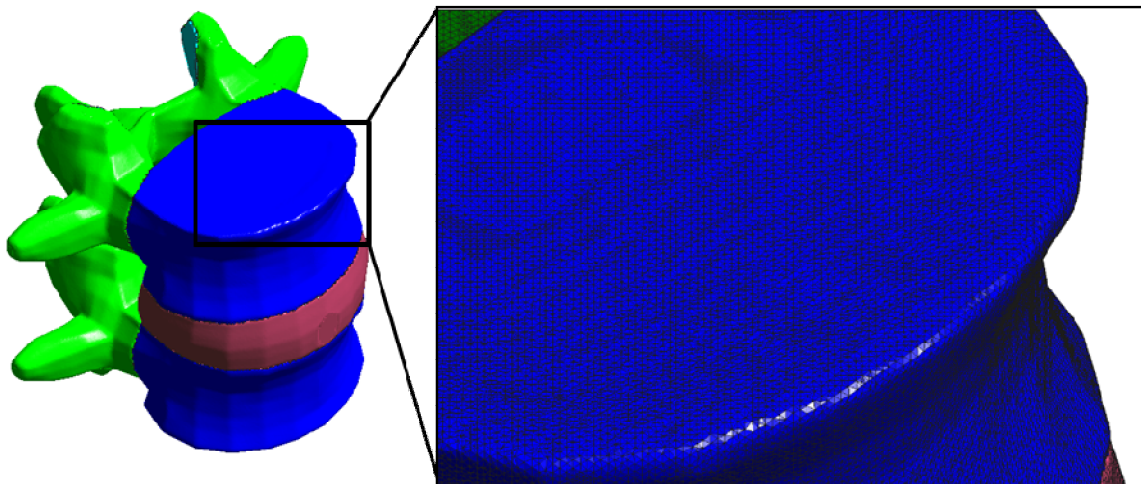
**Table 5.8 – Volumes of the different materials of the final FE mesh with a voxel dimension of 0.3x0.3x0.3 mm<sup>3</sup>.**

Voxel's Dimension [mm <sup>3</sup> ]		0.3x0.3x0.3										
Grid Dimension [mm]	0.25			0.5			1			2		
N	0.83			1.67			3.33			6.67		
σ	0.42	0.83	1.67	0.83	1.67	3.33	1.67	3.33	6.67	3.33	6.67	13.33
Number of Nodes [x10E6]	17.0			2.1	2.2	2.2	0.3	0.3	0.3	0.04	0.04	0.04
Number of Elements [x10E6]	97.6			12.0	12.1	12.1	1.5	1.5	1.5	0.2	0.2	0.2
Volume [mm <sup>3</sup> ]												
Vertebrae	41 511	41 455		41 508	41 437	41 351	41 600	41 453	40 865	40 747	40 365	38 238
Error (%)	1%	1%		1%	1%	1%	1%	1%	0%	-1%	-2%	-7%
Cortical Bone	25 470	25 468		25 496	25 480	25 554	25 665	25 806	26 186	24 058	23 667	19 488
Error (%)	1%	1%		1%	1%	2%	2%	3%	4%	-4%	-6%	-23%
Cancellous Bone	34 657	34 623		34 657	34 610	34 495	34 673	34 510	34 224	35 303	35 503	36 303
Error (%)	1%	1%		1%	1%	0%	1%	1%	0%	3%	3%	6%
Ligaments	561	552		534	541	376	64	23	0	2	0	0
Error (%)	0%	-2%		-5%	-4%	-33%	-89%	-96%	0	-100%	0	0
Endplate	1 556	1 548		1 527	1 545	1 442	867	795	29	255	5	0
Error (%)	0%	0%		-2%	0%	-7%	-44%	-49%	-98%	-84%	-100%	0
Annulus Fibrosus	10 797	10 798		10 807	10 797	10 806	10 844	10 851	10 836	10 619	10 728	10 678
Error (%)	1%	1%		1%	1%	1%	2%	2%	1%	-1%	0%	0%
Nucleus Pulposus	8 241	8 236		8 226	8 234	8 241	8 451	8 462	8 760	8 800	8 857	9 173
Error (%)	1%	1%		1%	1%	1%	4%	4%	7%	8%	9%	12%
IVD	20 594	20 582		20 560	20 576	20 489	20 162	20 108	19 625	19 674	19 589	19 850
Error (%)	1%	1%		1%	1%	1%	-1%	-1%	-4%	-3%	-4%	-3%
Total	122 793	122 679		122 755	122 644	122 265	122 164	121 899	120 900	119 784	119 124	113 879
Error (%)	1%	1%		1%	1%	1%	1%	0%	0%	-1%	-2%	-6%

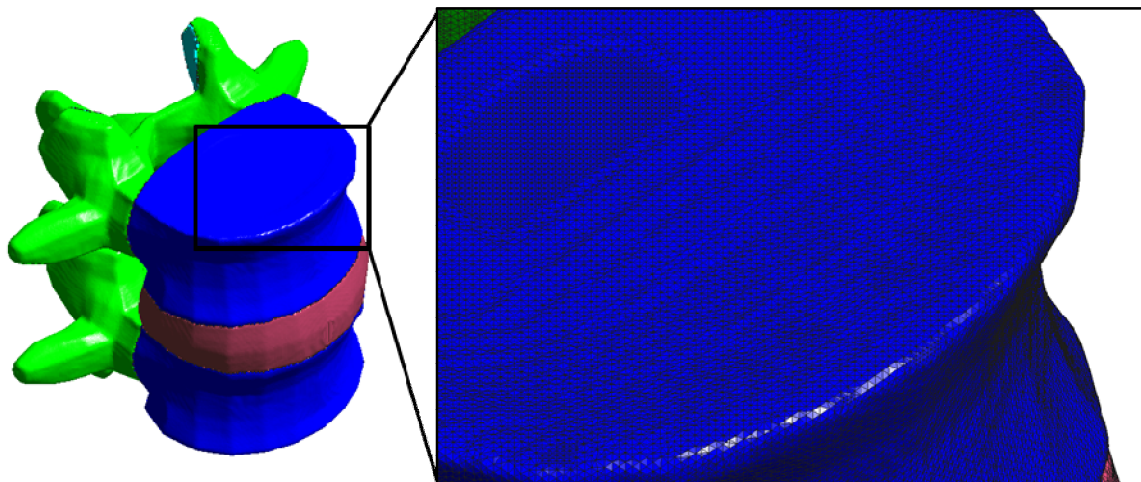
Using the software GID®, a pre and post processor for FE, one can plot the external boundary of the obtained FE meshes for the three different resolutions (while keeping constant the grid size of 0.5 and the largest  $\sigma$ ) – Figure 5.22 to Figure 5.24.



**Figure 5.22 – FE mesh obtained for the resolution of 0.3x0.3x3.3 mm<sup>3</sup>, grid size of 0.5 mm and  $\sigma$  value of 0.52.**



**Figure 5.23 - FE mesh obtained for the resolution of 0.12x0.12x0.12 mm<sup>3</sup>, grid size of 0.5 mm and  $\sigma$  value of 8.33.**



**Figure 5.24 - FE mesh obtained for the resolution of 0.3x0.3x0.3 mm<sup>3</sup>, grid size of 0.5 mm and  $\sigma$  value of 3.33.**

From the comparison between the boundaries of the initial domains, represented by different colours in the figures, and similar contours of the generated FE meshes, it is possible to observe (Figure 5.13 - Figure 5.21) that the sets of parameters chosen for the FE mesh generation had a very significant impact on the final geometrical results. These figures clearly show the influence of the parameter  $\sigma$  on the geometrical smoothing of both internal and external FE mesh boundaries. Increasing  $\sigma$  also increases the smoothing, thus allowing to obtain a less voxel-like geometry, and more alike real anatomical structures. The first conclusion to be drawn is, thus, that parameter  $\sigma$  must be preferably higher.

Another point to be noted is that the abovementioned meshes, in some regions have a saw tooth like shape (Figure 5.14 and Figure 5.15). This seems to be occurring mainly in case of large grid sizes, and mainly if grid size is of the same magnitude of the geometrical features of anatomical structures to be meshed. When one of the grid vertices, during the generation procedures, corresponds to one material and forward vertex corresponds to a different one, the result is a “zigzag” boundary like the ones that can be seen in some of the analysed cases. When the  $\sigma$  is too high this effect seems to disappear. In the case of voxel sizes of  $0.12 \times 0.12 \times 0.12$  and  $0.3 \times 0.3 \times 0.3$  mm<sup>3</sup>, the zigzag boundaries seem to have been eliminated. In these two cases, when defining the same grid sizes and if kept the same rationale for the determination of parameter  $\sigma$ , one can observe that the values of  $\sigma$  became very high. As seen before, the consequence is an increase of geometrical smoothing, which causes the loss of some tiny details of the biological structures, such as the endplate or the cortical bone (for instance, a grid size of 2 mm is larger than the thickness of aforesaid structures of the motion segment).

When the grid size decreases to 1 mm (dimension similar to the endplate thickness) it is possible to verify that the occurrence of zigzag boundaries also diminishes very much (Figure 5.17). However there are still some zigzag regions in the endplate, which will eventually disappear with the increase of the  $\sigma$  value. This will also influence some sharp edges of the motion segment, which will also be smoothed. However, it is true that such sharp features, having no physical meaning, are simply artefacts of the initial (reference) geometry.

As a conclusion, one avoid large amount of smoothing in order to restrain all the geometric features in the generated mesh. In the case of the grid size of 0.5 mm (half of the thickness of the endplate), there were no improvements in the final FE meshes obtained with a voxel size of  $0.3 \times 0.3 \times 0.3$  mm<sup>3</sup>, but it is observable that zigzag boundaries have disappeared, regardless of  $\sigma$

value. However, a better resolution of the voxel-based geometry always allows to obtain better results of the geometric definition of the anatomical structures by a FE mesh. Moreover, edges of the vertebrae suffer a slight smoothing and consequently a loss of some geometrical details (Figure 5.20).

Table 5.6, Table 5.7 and Table 5.8 show a summary of the global (full motion segment and IVD) and local (each structure or material) volumetric errors between the reference geometry and the generated FE mesh. It is obvious that, for the case of a voxel size of  $0.3 \times 0.3 \times 3 \text{ mm}^3$ , the volumetric errors were higher than those for other cases, and are more prominent in case of the endplate. It happens because large part of this structure is eliminated, as it can be seen in Figure 5.19. For the voxel size of  $0.12 \times 0.12 \times 0.12 \text{ mm}^3$ , with grid sizes of 0.25 and 0.5 mm (Table 5.3), the generated FE meshes has a volumetric error of the IVD very close to zero, when compared with the other grid sizes. Although these tables also present the results for grids with size of 0.25 mm, they were not discussed because in most cases the meshes were not successfully generated, mainly because algorithm terminates due to their large computational dimension. For a voxel size of  $0.12 \times 0.12 \times 0.12$  and  $0.3 \times 0.3 \times 0.3 \text{ mm}^3$ , the volumetric error of the IVD and of the total motion segment was highest for the grid size of 2.0 mm and lowest for the grid size of 0.5 mm. But for a voxel size of  $0.3 \times 0.3 \times 3 \text{ mm}^3$  it was the opposite.

Figure 5.22, Figure 5.23 and Figure 5.24 show the overall external FE mesh geometry of the motion segment. These figures show the non-simplified FE meshes obtained with a grid size of 0.5 mm, the largest  $\sigma$  value for each case and for all the three voxel sizes under analysis. In the first of these cases (voxel size of  $0.3 \times 0.3 \times 3 \text{ mm}^3$ ) one can easily observe: an unreal voxel-like shape; the loss of some structures; and some non-relevant geometrical details (such as the loss of cortical bone on the top). Since this FE mesh does not show an acceptable good geometrical accuracy, these FE mesh generation parameters were not considered satisfactory and were ignored for the next procedure. On the other hand, the other two cases shown presented good geometrical accuracy, and in spite of the non-negligible difference on voxel sizes, respectively  $0.12 \times 0.12 \times 0.12 \text{ mm}^3$  and  $0.3 \times 0.3 \times 0.3 \text{ mm}^3$ , no significant difference can be noticed. So, both were considered for the simplification process. Moreover, these two FE meshes did not present any loss of anatomical structures and only differ in their refinement, which is higher in the FE mesh generated from the voxel size data of  $0.12 \times 0.12 \times 0.12 \text{ mm}^3$  than in case of the voxel size data of  $0.3 \times 0.3 \times 0.3 \text{ mm}^3$ .

After the analysis of all the results obtained during the FE mesh generation procedure, the FE meshes obtained with the grid size of 0.5 mm and the higher  $\sigma$  value for the two voxel sizes of 0.12x0.12x0.12 and 0.3x0.3x0.3 mm<sup>3</sup>, were chosen as the best ones. These two FE meshed were selected for the following step, i.e., the FE mesh simplification, as they show good geometrical accuracy, and almost insignificant volumetric errors for all materials/structures.





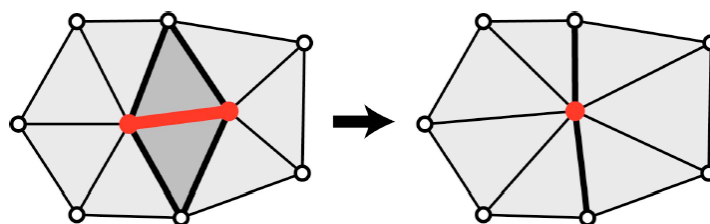
---

## Chapter 6. Finite Element Mesh Simplification

---

Generally, the FE meshes produced by the procedure introduced in Chapter 5 is highly refined and dense, and, consequently, computationally very expensive. Therefore, after the preliminary FE mesh generation, one needs to decrease its size by diminishing the total number of nodes and elements, but keeping the geometrical mesh quality and accuracy. This procedure can be designated as FE mesh simplification.

The FE mesh simplification is the process of reducing the number of tetrahedra in the mesh while keeping the overall shape, volume and boundaries preserved. FE meshes are simplified by edge contraction, in order to generate finite elements with a better geometrical shape, and decreasing the mesh refinement. In this method, using a cost function, local simplification operators are applied iteratively, which contract the edges (red line in Figure 6.1) of the elements taking into account the quality of the shape of the elements and their geometric error. The optimum location of the new node (red point in Figure 6.1) depends primarily on the angles formed by adjacent elements when the edge is contracted. Sometimes, it is not possible to contract some edges in order to preserve the mesh topology. However, an optimization strategy allows to contract other edges in order to simplify the mesh thus not affecting this topology.



**Figure 6.1 – FE mesh simplification by edge contraction.**

Since the FE mesh quality can significantly influence the performance and the accuracy of the FE solvers, two factors must be considered: the shape quality of the elements and the uniformity of their sizes. A very flat or thin element in a triangular mesh may increase the error in

the solution. Therefore, there is a need to make the adjacent angles similar or in the same proportion, thus eliminating the angles near 0° or 180°.

Hence, a good simplification method should allow a least geometric error, a good shape quality of the elements and decrease in the number of finite elements and nodes.

In this study, a simplification procedure was studied and applied to the FE mesh previously generated. This simplification algorithm needs a set of parameters that control and scan the simplification process. Table 6.1 briefly describes these parameters (command line options).

**Table 6.1 – Description of the different refinement criteria of the mesh simplification procedures.**

<b>Refinement Criteria</b>	<b>Description</b>
<b>-t0.05</b>	Set the element quality threshold to 0.05. This element quality is measured by the so-called scaled Jacobian, a positive real number that ranges from 0.0 to 1. The Jacobian of a perfect tetrahedron is set to 1.0 and of a completely 'flat' tetrahedron is 0.0. This parameter can be omitted and the default value is 0.1.
<b>-g</b>	This parameter switches on the preservation of boundary geometry. Boundary edges are not allowed to be contracted, unless they are lying on planar boundary surfaces. It can be omitted and the default case is the "geometry not preserved".
<b>-b</b>	Keep boundary non-simplified. If switched on, the edges belonging to an internal or external boundary cannot be contracted. This parameter can be omitted and the default case is "boundary can be simplified".
<b>-s</b>	Specify maximum edge length by a sizing field. This option performs absolute sizing and can be omitted. To use this option, input file must be a VTK with sizing field data. This parameter will be explained in more detail in the next section.
<b>-r</b>	Specify maximum edge length by relative sizing field. This option performs relative sizing and it can be omitted. To use this option, input file must be a VTK with sizing field data. This parameter will be explained in more detail in the next section.
<b>100000</b>	Set the desired number of elements to 100000. This parameter is mandatory because it works as a target to stop the simplification process. An option to define this parameter is the next parameter.
<b>0.1</b>	Set the desired simplification ratio to 0.1. (simplification ratio) = (number of elements in simplified FE mesh)/(number of elements in original FE mesh).

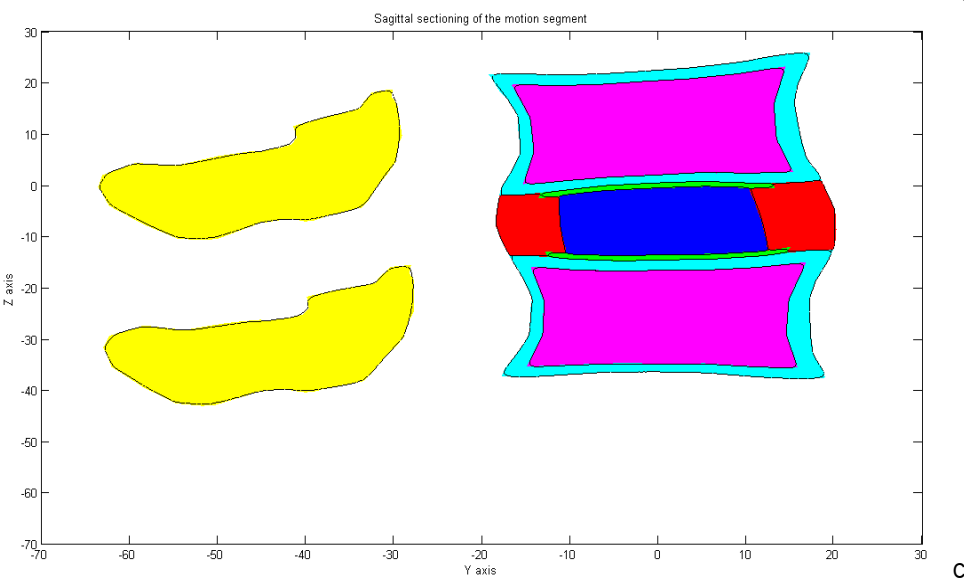
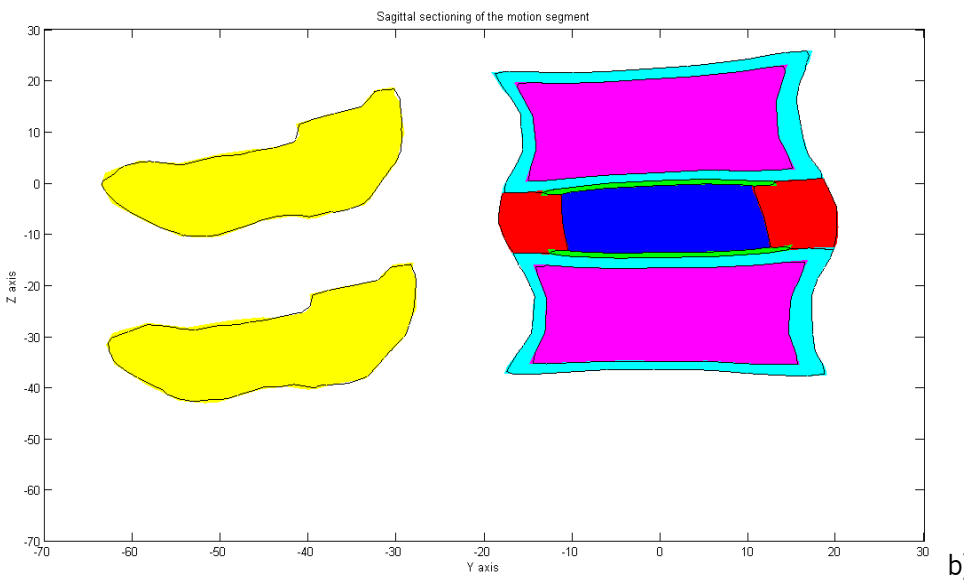
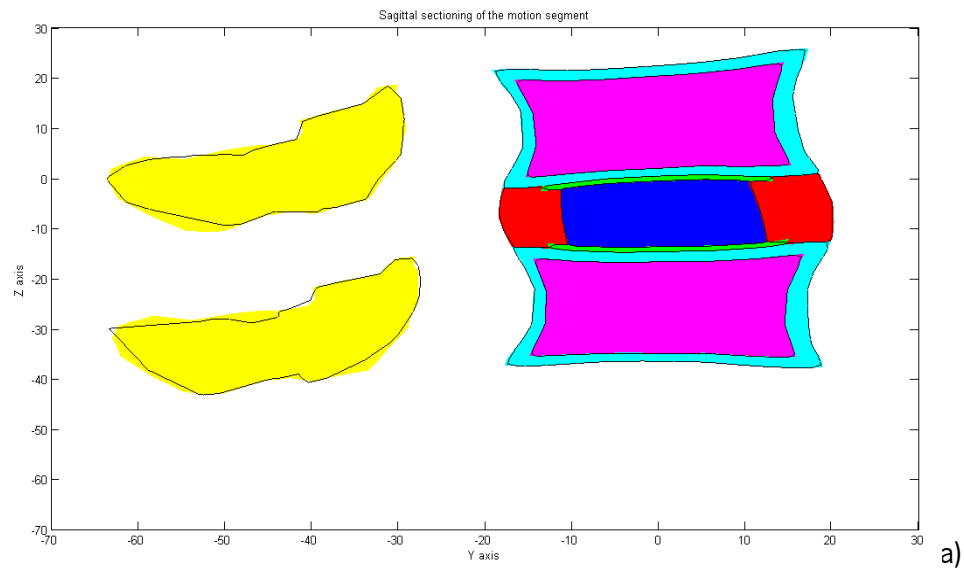
For the analysis of the simplification process only two FE meshes were considered. These two FE meshes are based on a grid size of 0.5, with the largest  $\sigma$ , for the two voxel sizes of 0.12x0.12x0.12 and 0.3x0.3x0.3 mm<sup>3</sup>.

Three different simplification procedures were drawn and carried out on the abovementioned FE mesh. First, considering the default parameters of the simplification algorithm, the target number of elements was set to 100 000 finite elements; on second try the same target number coupled with parameter  $-t0.05$ ; and in the third case parameter  $-g$  was added to the previous condition in order to understand the effect of this parameter in the FE mesh simplification procedure. These three simplification cases studied are summarised in Table 6.2.

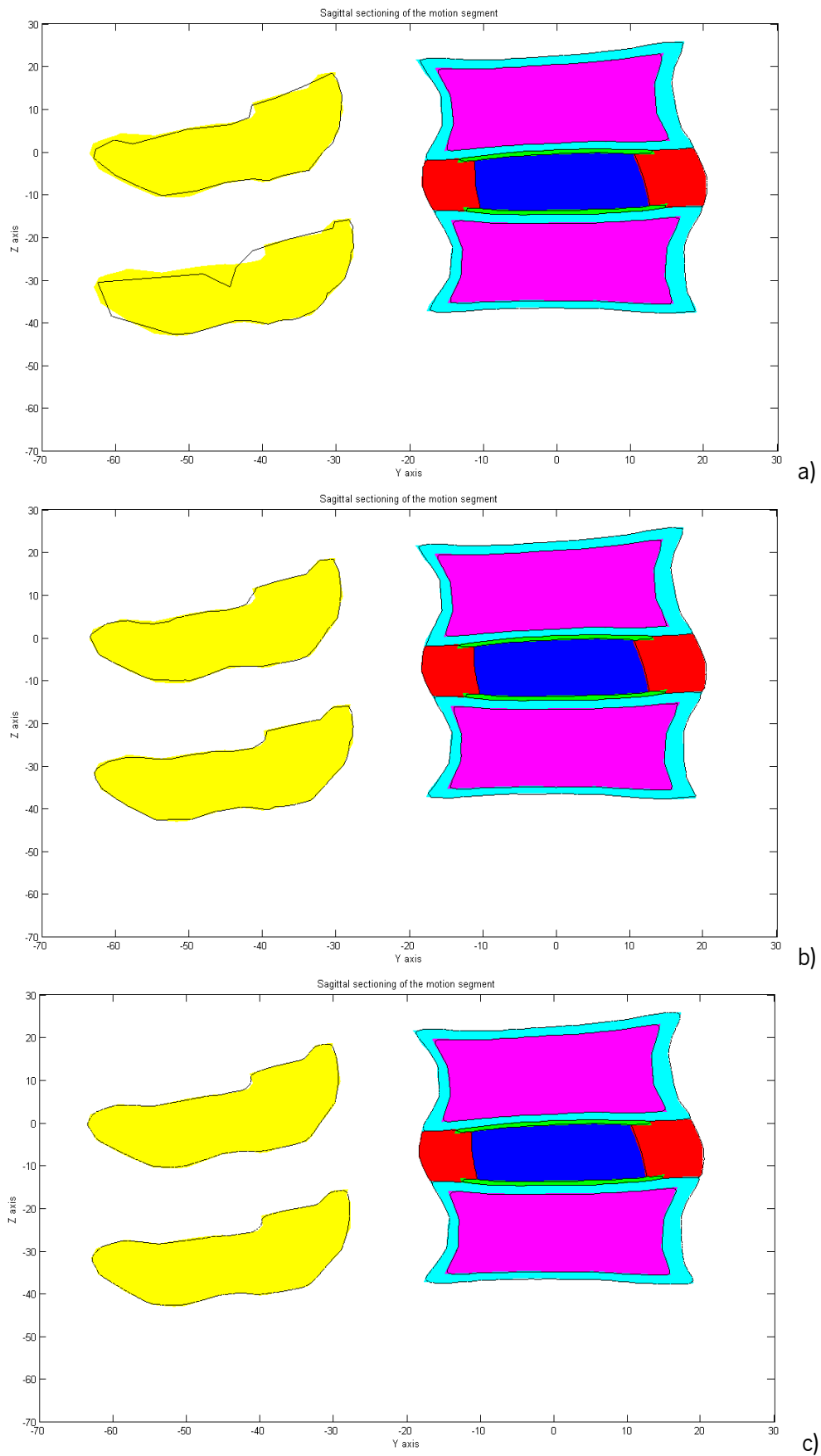
**Table 6.2 – Simplification case studies.**

<b>Simplification Test</b>	<b>Simplification parameter used</b>
<b>Simp1</b>	100 000
<b>Simp2</b>	$[-t0.05]$ 100 000
<b>Simp3</b>	$[-t0.05]$ $[-g]$ 100 000

The simplification procedure is time consuming, taking around 2-3 hours for each case. In order to compare and evaluate the geometrical accuracy of the simplified FE meshes, several sagittal cross sections were determined and plotted. Figure 6.2 and Figure 6.3 show a comparison between the initial geometrical domains and boundaries (coloured areas) and the boundary contours of each simplified FE mesh.



**Figure 6.2 - Sagittal sectioning ( $X=2$ ) of the FE mesh based on the resolution of  $0.12 \times 0.12 \times 0.12 \text{ mm}^3$  for a) simplification 1: 100 000; b) simplification 2:  $[-t0.05]$  100 000; c) simplification 3:  $[-t0.05]$   $[-g]$  100 000.**



**Figure 6.3 - Sagittal sectioning (X=2) of the FE mesh based on the resolution of 0.3x0.3x0.3 mm<sup>3</sup> for a) simplification 1: 100 000; b) simplification 2: [-t0.05] 100 000; c) simplification 3: [-t0.05] [-g] 100 000.**

It is observable that, in both cases, the first simplification procedure results in a loss of vertebral arches geometrical accuracy, whereas for the remaining simplification cases it does not happen. Comparing the number of nodes, number of elements and minimum and maximum dihedral angles of the tetrahedral FE mesh, it is possible to observe that the largest simplification is attained with the second set of parameters, and that only in these cases the simplification processed stopped due to the fact that the target number of elements has been reached. The main statistical data of the simplified FE meshes is shown on Table 6.3.

**Table 6.3 – Number of nodes and elements and the dihedral angles for different simplification tests.**

Case	Voxel size [mm <sup>3</sup> ], N and $\sigma$	Simplification Tests	Tetrahedral FE mesh		Dihedral Angles [°]	
			Nodes	Elements	Min	Max
<b>1</b>	0.12x0.12x0.12 N=4.17 $\sigma$ =8.33	Original	2 156 473	12 065 741	2.99	174.77
		Simp1	21 790	123 180	5.71	167.92
		<b>Simp2</b>	17 444	<b>99 997</b>	3.46	174.11
		Simp3	111 618	496 823	3.37	174.16
<b>2</b>	0.3x0.3x0.3 N=1.67 $\sigma$ =3.33	Original	2 167 854	12 132 306	4.46	173.67
		Simp1	26 600	151 741	4.79	167.84
		<b>Simp2</b>	17 469	<b>99 998</b>	3.16	173.93
		Simp3	155 325	712 969	3.17	174.17

At this point of the simplification process, the FE mesh simplification algorithm was carried out equally over all the domains of the initial FE mesh, i.e., the FE density is expected to be similar, for instance at both vertebrae and IVD. However, our paramount goal is to generate a good quality FE mesh of the IVD, and for normal mechanical loadings applied to a motion segment, the vertebrae shall behave almost as an incompressible medium, and only the IVD will show non-negligible strains. In this case, it is acceptable (and desirable) to attain a problem-functional FE mesh, in which the mesh refinement shall be larger on the IVD than at the vertebrae.

In order to deepen this question, and looking to the data on Table 6.3, it was decided to restrict the next study to only two meshes, namely the ones obtained from the second simplification case (labelled Simp2). These two meshes present the smallest number of nodes and had reached a simplification equal to the desired number of elements (100 000). Regarding the values of the angles of the simplified elements it is possible to observe that, in both cases, the smallest angle is close to 3° and the greatest to 174°. These elements are defined as unhealthy elements because their dihedral angles are very close to 0° and 180°.

## 6.1. Absolute/relative edge sizing

For many applications of image rendering and engineering, the need for accuracy is greater near the surface of the domain. Generally, the smaller elements are located at internal and external boundaries, while larger elements are located inside the FE mesh.

However, this is not always acceptable. There may be situations where this accuracy may be required simultaneously in structures outside and inside the FE mesh. This section will discuss an absolute or relative edge sizing, with the objective of creating smaller elements in the IVD region and larger elements in other structures of the motion segment. The goal is to reduce drastically the number of elements in the final FE mesh and consequently to reduce the computation time required for the FE analysis.

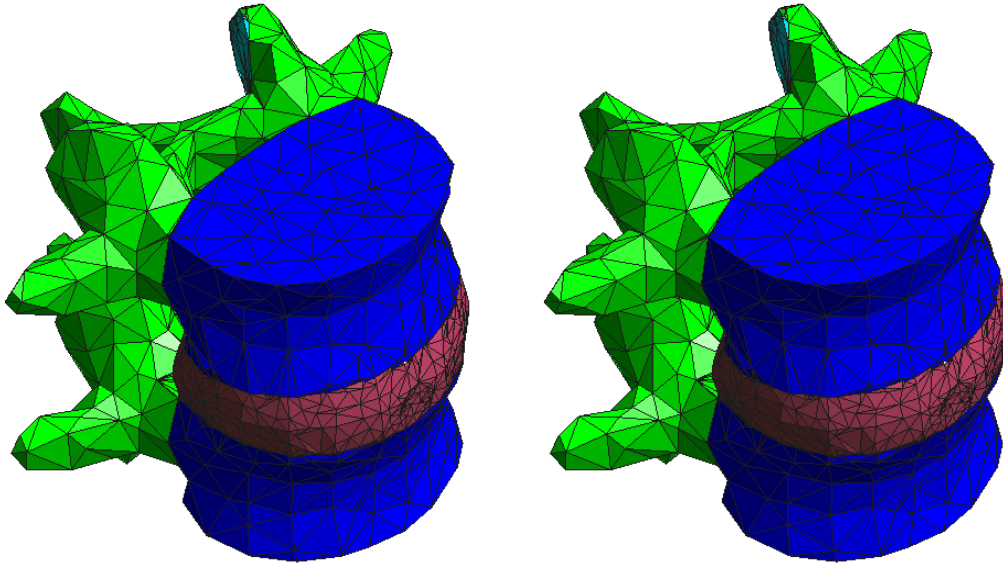
This new algorithm was implemented to study the influence of the two aforesaid parameters  $-s$  and  $-r$  (see Table 6.1). Two meshes (chosen from the second simplification strategy) were converted into a VTK format, and a sizing field added, in order to be used as input file for the simplification process. The sizing field, which can be absolute or relative, is the maximum edge length of the elements.

Initially, a study of the  $-s$  parameter was performed. The values specified by the user for the edge sizing field (defined at each node), inside and outside the IVD region are presented in Table 6.4.

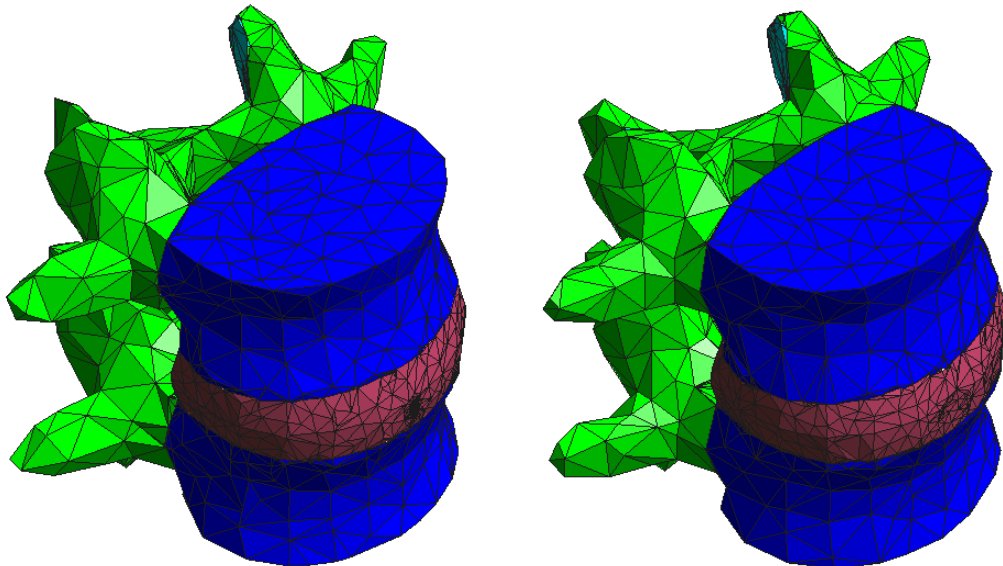
**Table 6.4 – Sizing tests performed with absolute parameter.**

Sizing Tests	Specified max edge	Specified max edge	Absolute Parameter
	length inside the IVD [mm]	length outside the IVD [mm]	
<b>1</b>	0.5	10.0	-s
<b>2</b>	1.0	10.0	

The 3D final FE meshes obtained for the two different absolute sizing field tests of the two FE meshes studied are shown in Figure 6.4 and Figure 6.5.



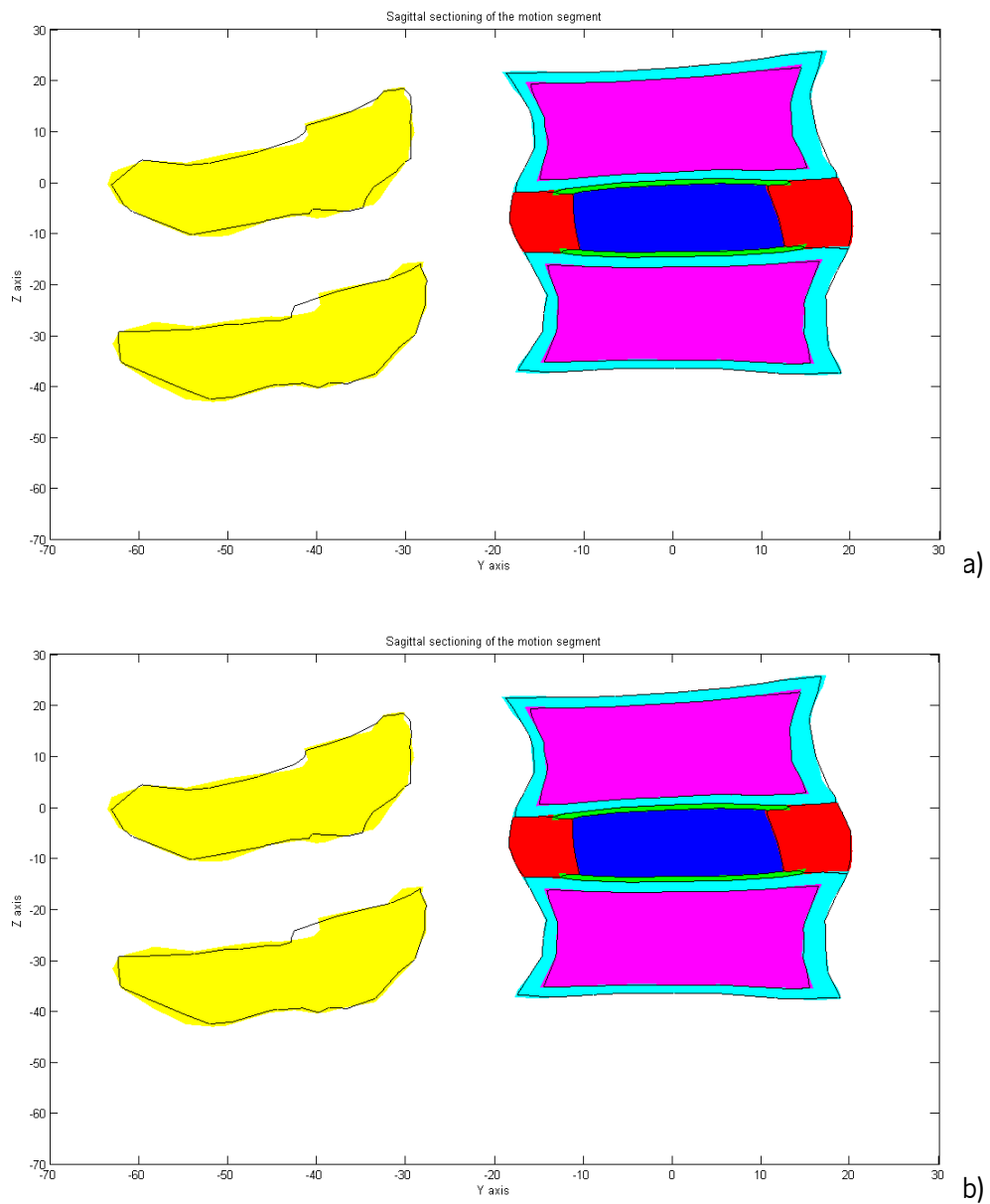
**Figure 6.4 - FE mesh obtained based on simplification 2 from voxel size of  $0.12 \times 0.12 \times 0.12 \text{ mm}^3$  with sizing parameters of (left) 0.5 and 10 (right) 1.0 and 10 for max edge length inside the IVD and max edge length outside the IVD, respectively.**



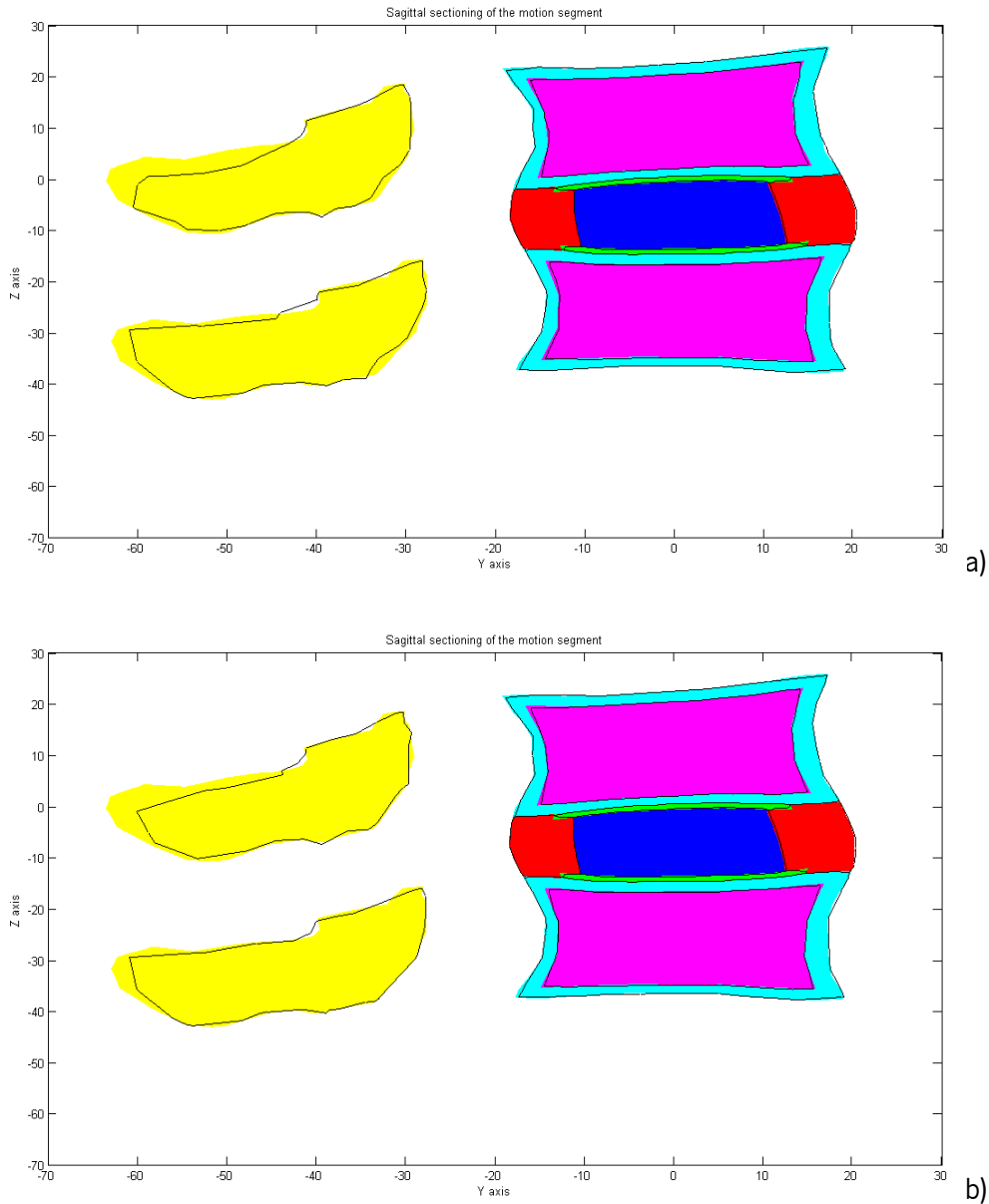
**Figure 6.5 - FE mesh obtained based on simplification 2 from voxel size of  $0.3 \times 0.3 \times 0.3 \text{ mm}^3$  with sizing parameters of (left) 0.5 and 10 (right) 1.0 and 10 for max edge length inside the IVD and max edge length outside the IVD, respectively.**

The sagittal cross sections of the initial geometry and of the simplified FE mesh for the two different tests of the two meshes studied are shown in Figure 6.6 and Figure 6.7. Through this procedure it is possible to analyze the changes in the geometrical contours of the final FE mesh boundaries.





**Figure 6.6 - Sagittal sectioning ( $X=2$ ) of the FE mesh based on simplification 2 from voxel size of  $0.12 \times 0.12 \times 0.12$  mm<sup>3</sup> for a) 0.5 and 10 b) 1.0 and 10 of the edge length in IVD and edge length outside of the IVD, respectively.**



**Figure 6.7 –Sagittal sectioning (X=2) of the FE mesh based on simplification 2 from voxel size of 0.3x0.3x0.3 mm3 for a) 0.5 and 10 b) 1.0 and 10 of the edge length.**

Table 6.5 shows the final number of elements, number of nodes and maximum and minimum dihedral angles of the four different cases under analysis.

**Table 6.5 - Number of elements and nodes and the dihedral angles for different simplification tests with two different edges length.**

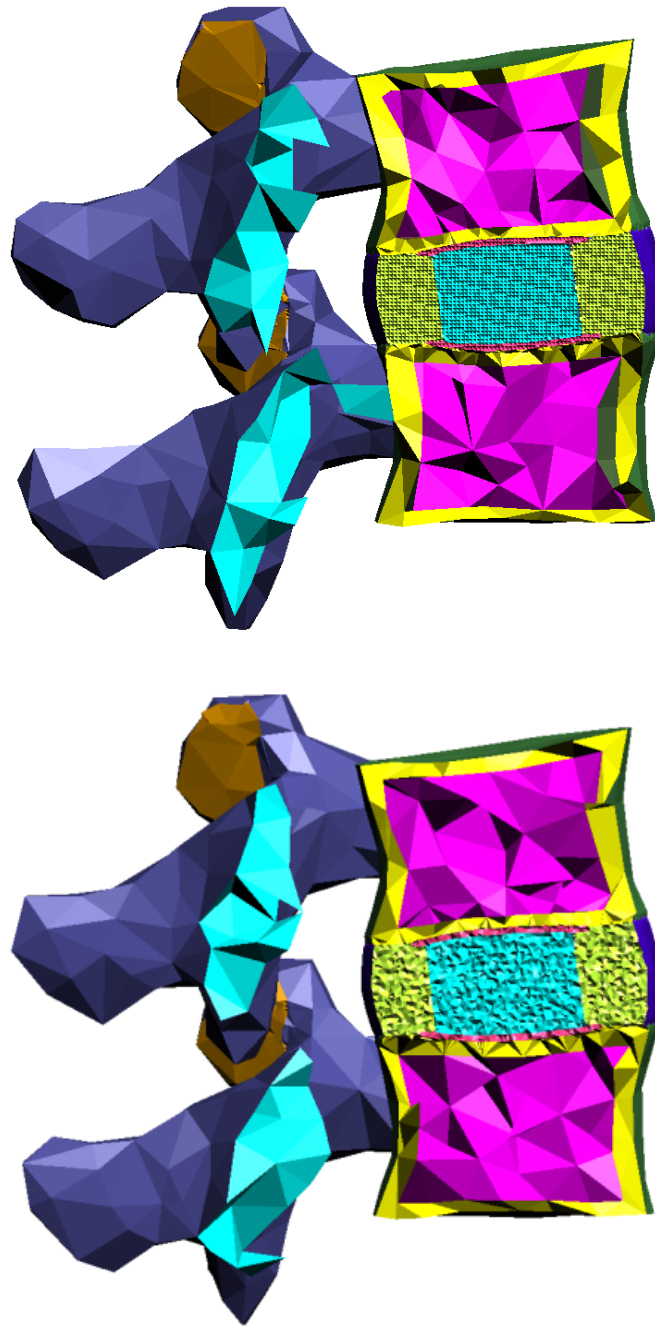
Tests	Edges Length	Nodes	Elements	Dihedral Angles (°)	
		Number	Number	Min	Max
<b>Simp2 (0.12x0.12x0.12)</b>	Original	17 444	99 997	3.46	174.11
	0.5 and 10.0	6 417	36 371	0.80	178.67
	1.0 and 10.0	6 417	36 371	0.80	178.67
<b>Simp2 (0.3x0.3x0.3)</b>	Original	17 100	100 000	3.35	173.68
	0.5 and 10.0	6 733	38 162	0.71	178.65
	1.0 and 10.0	6 733	36 371	0.71	178.65

Through Figure 6.4 and Figure 6.5 it is possible to see that there is a noticeable difference in the overall elements size between the IVD and the other regions of the motion segment. The geometrical accuracy is well visible in both these figures and in the sagittal cross sections (Figure 6.6 and Figure 6.7). However, simply by the analysis of these figures it is not possible to conclude anything concerning the number of elements located in each region of the FE mesh. Table 6.5 presents a resume of the number of elements, number of nodes and maximum and minimum dihedral angles of the final simplified FE meshes. The first mesh studied (0.12x0.12x0.12 mm<sup>3</sup>) presents a small number of nodes and elements with no difference between the two values chosen for sizing. In the case of the second mesh studied (0.3x0.3x0.3 mm<sup>3</sup>), there is a slightly higher number of nodes and elements than on the other mesh. The dihedral angles range between 0.7° and 178° (very probably only a few pathological cases that shall be eliminated from the FE mesh).

To test the behaviour of the -r parameter, a new procedure was adapted with a non-simplified FE mesh with the same parameters (maximum edge length inside and outside of the IVD) used above (for -s parameter tests). Table 6.6 presents the edge sizing data, for IVD and for the regions outside the IVD, chosen for the study of -r parameter. The target relative dimensions are also shown in the table.

**Table 6.6 – Sizing tests performed with relative parameter for a non-simplified mesh.**

Sizing Tests	Specified max	Specified max	Relative Parameter
	edge length inside the IVD	edge length outside the IVD	
	[mm]	[mm]	
<b>1</b>	0.5	10.0	(1:20)
<b>2</b>	1.0	10.0	-r (1:10)



**Figure 6.8 – Meshes from simplification with relative sizing of 1:20 (upper mesh) and 1:10 (lower mesh).**

Figure 6.8 shows the 3D FE meshes obtained for two different relative sizing tests. A very refined mesh in the IVD can be seen, simultaneously with a very coarse one on the remaining structures of the motion segment. One shall definitely conclude about the merits of this simplification procedure, which can be used to obtain computationally very effective and simple FE meshes with a fully customized definition of the required refinement for the several structures of a given motion segment.

---

## Chapter 7. Conclusion

---

The initial step of medical imaging processing of a real goat motion segment was found to be very troublesome. Firstly, several segmentation methods used in MR and micro-MR medical images of a goat motion segment proved to be inadequate for the imaging segmentation, and thus for an accurate 3D geometrical reconstruction of the motion segment in general, and the intervertebral disc in particular. The low image resolution in one case, and the poor definition of the motion segment sub-structures in the other, did not allow the use of an automatic segmentation procedure, and led to a non-rigorous and time expensive and very user-dependent segmentation process. At the end of this preliminary stage, two 3D voxel-based models of the goat motion segment were effectively obtained, but with a high level of geometrical uncertainty and thus a geometrical inaccuracy that was not compatible with the essential requirements for the FE mesh generation procedure.

Therefore, a new virtual segmentation procedure based on an initial and well-defined geometry of a motion segment was developed and implemented. This new algorithm allowed to obtain virtually a set of 2D segmented medical images, and to reconstruct a voxel-based 3D model with a user-defined resolution (or voxel's dimensions, i.e., in-plane pixel size and slice spacing). The three different voxel sizes studied allowed to conclude that the resolution of the medical images influences mostly the geometrical accuracy of the reconstructed 3D models. Images with higher resolutions allowed building models with higher geometrical accuracy.

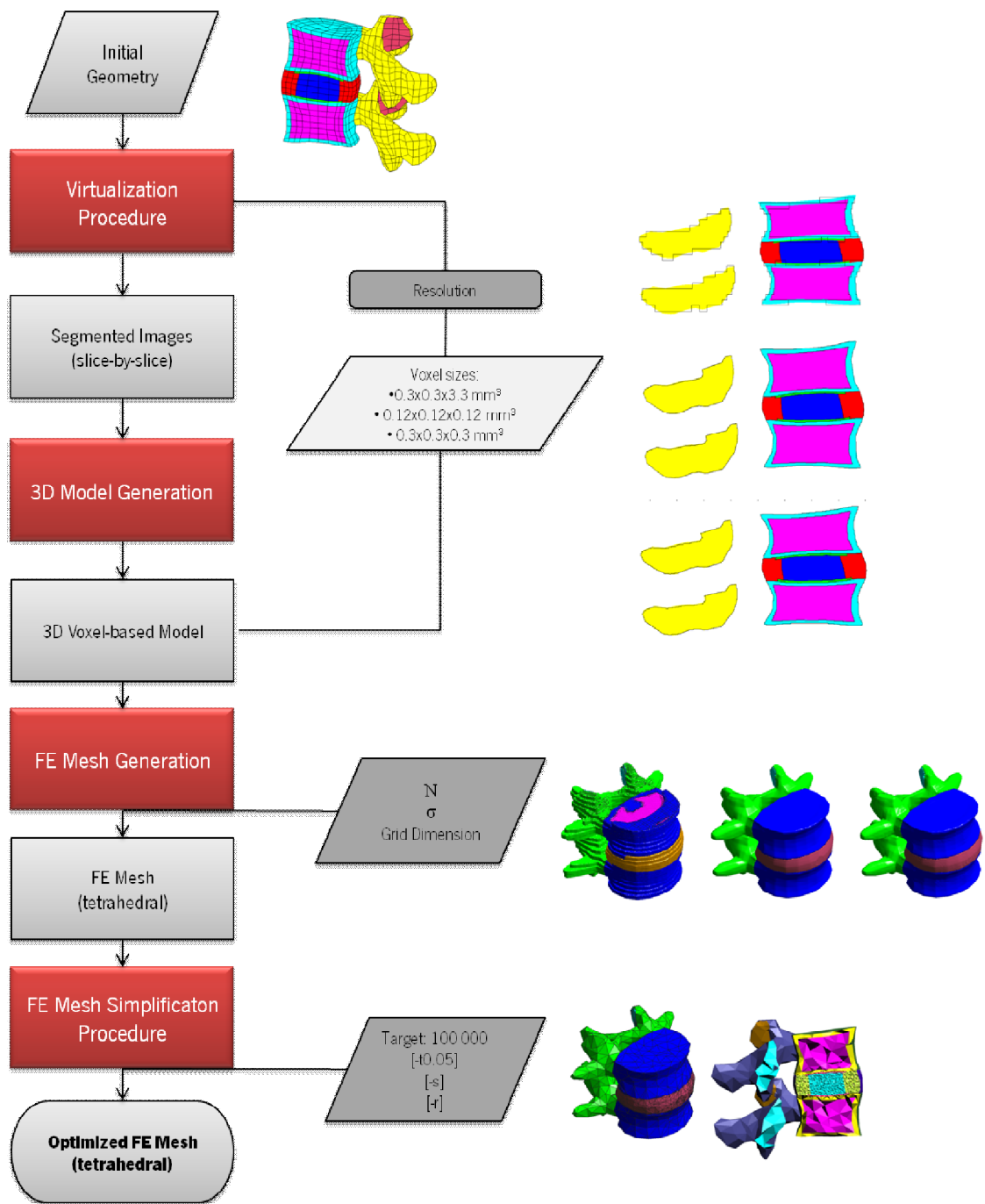
The 3D voxel-based geometric models obtained from the well-defined initial geometry were used for the study of the FE mesh generation procedure. For each one of the three most-relevant selected case studies, twelve FE meshes were generated based on different FE mesh generation parameters, namely grid size,  $N$  and  $\sigma$  parameters. Throughout the FE mesh generation process, one was able to conclude that the grid size of 0.5 mm was the best compromise between the FE mesh generation computational effort and the global geometrical accuracy. In more details one verified that with a grid size of 0.5 mm, even the smallest structure - like the endplate - was

geometrically correctly and accurately described by the FE meshes. Therefore, one can state that the choice of the grid's size depends essentially on the size of the smallest structure/region that shall be geometrically captured by the FE mesh. As parameter  $N$  defines the grid size as a function of the diagonal of the voxel, it was found that in some cases the voxel size was not compatible with the FE mesh generation software (normally in the case of very low values of  $N$ ).

Although carefully defined, it is uncertain whether parameter  $\sigma$  have or not a positive or negative influence on the final result. Depending on both voxel size and the grid size, parameter  $\sigma$  can contribute to improve the definition of some anatomical details and, simultaneously, contribute to eliminate some less relevant geometrical details. With this work, it was possible to conclude that a choice of a value of parameter  $\sigma$  around twice the value of  $N$  (i.e., twice the grid size), allows to generate a well-defined geometry and to smooth structural features like sharp edges that do not resemble real geometries.

The FE mesh simplification procedure also allowed demonstrating the possibility to completely master the simplification process by defining a non-uniform and user-definable sizing field. For example, the definition of a higher FE mesh refinement in regions of interest (like the IVD) can be easily obtained using the proposed FE mesh simplification algorithm. Essentially, an absolute (-s) or a relative (-r) sizing field allows to manipulate edges' sizes, and thus FE sizes, in different regions/structures of the global FE mesh. It is a powerful tool to decrease the size (number of nodes and number of elements) of the FE meshes, keeping simultaneously geometrical accuracy and FE mesh quality.

Finally, this work allowed to conclude that following the proposed algorithm (summarised on Figure 7.1) it is possible to describe, with a reasonable geometrical accuracy and by a good quality FE mesh, the bio-structures of a motion segment in order to develop computational studies by finite element analysis of the biomechanical behaviour of the Human spine.



**Figure 7.1 - Proposed FE mesh generation procedure developed in this study.**





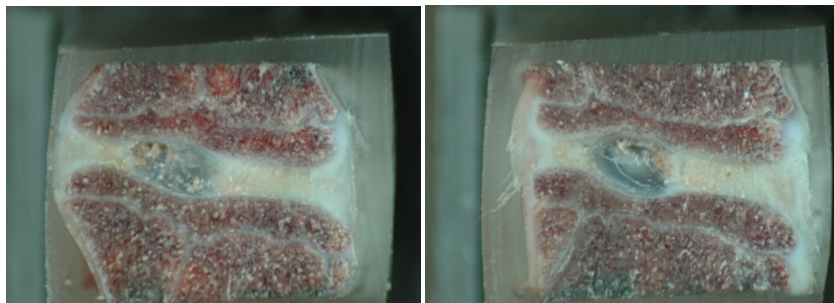
---

## Chapter 8. Future Work

---

At the end of this work, one could point out two main difficulties that were faced during the development. The first one was related with the unclear definition, by medical imaging data, of the 'real' boundaries and 'real' geometries of the structures under analysis; the second one was the 'apparent' incompatibility between elongated voxels and the FE mesh generation procedures evaluated. Therefore, two main research vectors could be pointed out as future work.

Firstly, the development of a *post-mortem* destructive characterization procedure of the goat lumbar motion segment (two vertebrae and one intervertebral disc), based on a destructive serial-sectioning technique, for a more objective geometrical/anatomical characterization of a motion segment. In fact, an image acquisition procedure associated with the aforesaid destructive geometrical characterization technique should allow to obtain a more accurate 3D geometrical reconstruction and, thus, the generation of a more geometrically accurate 3D FE mesh of the aforesaid bio-structures. In fact, the RGB (red, green and blue) images shall contribute to a better and easier definition of the internal boundaries, and thus to contribute to improve our understanding about imaging processing and 3D reconstruction of more accurately geometrical models. Ideally, the goat motion segment to be destructively characterized should also be, *a priori*, characterized by any non-destructive medical imaging technique.



**Figure 8.1 – Characterization of the porcine lumbar motion segment using a destructive serial-sectioning technique.**

Secondly, the numerical experimentation developed during this work, and particularly the analysis of the voxel's dimensions, clearly shown that very elongated voxels strongly limits the application of the proposed numerical algorithms for FE mesh generation and simplification. Another possible forthcoming research activity around this topic might be to change the procedure in order to consider an intermediate step between 3D voxel-based geometrical data and the FE mesh generation procedure, aiming to eliminate the strong stepwise discretization along axial axis. A possible strategy could be to identify the stepwise boundary, to describe them with polyhedral surfaces and finally to smooth this polyhedral surface with an adequate technique. The adoption of this approach could allow to obtain a better 3D geometrical reconstruction by FE elements even from a poor medical imaging resolution data.

Finally, a parametric-based FE mesh generation tool could also be developed for the most relevant motion segment to be studied. Therefore, one could work on the development of an algorithm that would allow to adapt a previously generated FE mesh to the "measures" of a given patient. Such "measures" could be obtained by classical low resolution *in-vivo* medical imaging techniques, such as X-ray, CT or MRI.

## References

- Adams, M. A., M. Stefanakis, *et al.* (2010). "Healing of a painful intervertebral disc should not be confused with reversing disc degeneration: Implications for physical therapies for discogenic back pain." Clinical biomechanics (Bristol, Avon) **25**(10): 961-971.
- Adams, R. and L. Bischof (1994). "Seeded region growing." IEEE Transactions on Pattern Analysis and Machine Intelligence (TPAMI) **16**(6): 641-647.
- Bankman, I. N. (2000). Handbook of medical imaging: processing and analysis. Baltimore, MD, USA, Academic Press.
- Bao, C. and Q. Meng (2010). "Study on Mechanical Characteristics of Lumbar Spine for Snatch Action in Weight Lifting Based on Finite Element Method." International Journal of Sports Science and Engineering **04**(1): 048-005.
- Barroso, E. M., C. Garbe, *et al.* (2011). Métodos de segmentação para modelação 3D do ouvido a partir de imagens. Congresso de Métodos Numéricos em Engenharia. Coimbra.
- Bibby, S. R. S., D. A. Jones, *et al.* (2001). "The pathophysiology of the intervertebral disc." Joint Bone Spine **68**(6): 537-542.
- Bonny, J. M., M. Gaviria, *et al.* (2004). "Nuclear magnetic resonance microimaging of mouse spinal cord in vivo." Neurobiology of Disease **15**(3): 474-482.
- Butler, P., A. W. M. Mitchell, *et al.* (2007). Applied radiological anatomy for medical students. Cambridge, United Kingdom., Cambridge University Press.
- Caselles, V., R. Kimmel, *et al.* (1997). "Geodesic active contours." International journal of computer vision **22**(1): 61-79.
- Daavittila, I. (2007). Genetic risk factors for lumbar intervertebral disc disease characterized by sciatica. Acta Universitatis Ouluensis D Medica. Oulu, University of Oulu. **500**.
- Dougherty, G. (2009). Digital image processing for medical applications. Cambridge, United Kingdom, Cambridge University Press
- Ebraheim, N. A., A. Hassan, *et al.* (2004). "Functional anatomy of the lumbar spine." Seminars in Pain Medicine **2**(3): 131-137.
- Fujiwara, A., K. Tamai, *et al.* (1999). "The relationship between facet joint osteoarthritis and disc degeneration of the lumbar spine: an MRI study." European Spine Journal **8**(5): 396-401.
- Haughton, V. (2006). "Medical Imaging of Intervertebral Disc Degeneration." The Journal of Bone and Joint Surgery **88 - A**(2).

- Henke, W. T., Ian (2007). Handbook of Paleoanthropology: Principles, Methods and Approaches. New York, Springer-Verlag Berlin and Heidelberg GmbH & Co. K.
- Higgins, C. B. and A. de Roos (2006). MRI and CT of the cardiovascular system. Philadelphia, PA, USA, Lippincott Williams & Wilkins.
- Hitchon, P. W., S. S. Rengachary, *et al.* (1995). Techniques in spinal fusion and stabilization. New York, New York, Thieme.
- Holdsworth, D. W. and M. M. Thornton (2002). "Micro-CT in small animal and specimen imaging." Trends in Biotechnology **20**(8): S34-S39.
- Hounsfield, G. N. (1973). "Computerized transverse axial scanning (tomography): Part 1. Description of system." British Journal of Radiology **46**(552): 1016.
- Iida, T., K. Abumi, *et al.* (2002). "Effects of aging and spinal degeneration on mechanical properties of lumbar supraspinous and interspinous ligaments." The Spine Journal **2**(2): 95-100.
- Jensen, G. M. (1980). "Biomechanics of the Lumbar Intervertebral Disk: A Review." Physical Therapy **60**(6): 765-773.
- Jongeneelen, C. J. M. (2006). Biomechanics in the Intervertebral Disc. Department of Biomedical Engineering. Eindhoven, The Netherlands, Eindhoven University of Technology.
- Kakol, W., T. Lodygowski, *et al.* (2003). "Are we able to support medical diagnosis or rehabilitation of human vertebra by numerical simulation." Computer Methods in Mechanics.
- Krämer, J. (2008). Intervertebral disk diseases: Causes, diagnosis, treatment and prophylaxis. Stuttgart, Germany, Thieme Medical Pub.
- Lakare, S. (2000). "3D segmentation techniques for medical volumes." Neural Networks: 1-23.
- Li, H. and Z. Wang (2006). "Intervertebral disc biomechanical analysis using the finite element modeling based on medical images." Computerized medical imaging and graphics **30**(6-7): 363-370.
- Liu, X. S., X. H. Zhang, *et al.* (2010). "Accuracy of high-resolution in vivo micro magnetic resonance imaging for measurements of microstructural and mechanical properties of human distal tibial bone." Journal of Bone and Mineral Research **25**(9): 2039-2050.
- Ma, Z., J. M. R. S. Tavares, *et al.* (2010). "A review of algorithms for medical image segmentation and their applications to the female pelvic cavity." Computer Methods in Biomechanics and Biomedical Engineering **13**(2): 235-246.
- Majumdar, S. and H. Genant (1997). "High resolution magnetic resonance imaging of trabecular structure." European radiology **7**(2): 51.

- McInerney, T. and D. Terzopoulos (1996). "Deformable models in medical image analysis: a survey." Medical Image Analysis **1**(2): 91-108.
- Meng, Q. and C. Bao (2009). "Study on Lumbar Vertebrae Biomechanical Characteristics for Speed Skating Athlete Based on Finite Element Method." International Journal of Sports Science and Engineering **03**(03): 169-117.
- Naegel, B. (2007). "Using mathematical morphology for the anatomical labeling of vertebrae from 3D CT-scan images." Computerized medical imaging and graphics : the official journal of the Computerized Medical Imaging Society **31**(3): 141-156.
- Natarajan, R., J. Williams, *et al.* (2007). "Poro-elastic finite element model to predict the failure progression in a lumbar disc due to cyclic loading." Computers & Structures **85**(11-14): 1142-1151.
- Natarajan, R. N., J. R. Williams, *et al.* (2003). "Finite element model of a lumbar spinal motion segment to predict circadian variation in stature." Computers & Structures **81**(8-11): 835-842.
- Niosi, C. A. and T. R. Oxland (2004). "Degenerative mechanics of the lumbar spine." Spine Journal **4**(6 Suppl): 202S-208S.
- Pal, N. R. and S. K. Pal (1993). "A review on image segmentation techniques." Pattern Recognition **26**(9): 1277-1294.
- Pham, D. L., C. Xu, *et al.* (1998). A Survey of Current Methods in Medical Image Segmentation. T. R. JHU. Baltimore.
- Postacchini, F. (1999). Lumbar disc herniation. New York, Springer Verlag Wien.
- Raj, P. P. (2008). "Intervertebral Disc: Anatomy-Physiology-Pathophysiology-Treatment." Pain Practice **8**(1): 18-44.
- Rannou, F., M. Corvol, *et al.* (2001). "Disk degeneration and disk herniation: the contribution of mechanical stress." Joint Bone Spine **68**(6): 543-546.
- Reid, J. E., J. R. Meakin, *et al.* (2002). "Sheep lumbar intervertebral discs as models for human discs." Clinical Biomechanics **17**(4): 312-314.
- Renner, S. M., R. N. Natarajan, *et al.* (2007). "Novel model to analyze the effect of a large compressive follower pre-load on range of motions in a lumbar spine." Journal of biomechanics **40**(6): 1326-1332.
- Ritman, E. L. (2004). "Micro-computed tomography-current status and developments." Annual Review of Biomedical Engineering **6**: 185-208.
- Schmidt, H., A. Kettler, *et al.* (2007). "Intradiscal pressure, shear strain, and fiber strain in the intervertebral disc under combined loading." Spine **32**(7): 748.

- Shankar, H., J. A. Scarlett, *et al.* (2009). "Anatomy and pathophysiology of intervertebral disc disease." Techniques in Regional Anesthesia and Pain Management **13**(2): 67-75.
- Smit, T. (2002). "The use of a quadruped as an in vivo model for the study of the spine - biomechanical considerations." European Spine Journal(2): 137-144.
- Strolka, I., A. Accardo, *et al.* (2003). "Segmentation of magnetic resonance microimages of trabecular bone: classifiers and markov random field model." Measurement in Biomedicine **3**.
- Suetens, P. (2009). Fundamentals of Medical Imaging, Cambridge University Press.
- Swider, P., A. Pédrone, *et al.* (2010). "Substructuring and poroelastic modelling of the intervertebral disc." Journal of biomechanics **43**(7): 1287-1291.
- Tyndyka, M. A., V. Barron, *et al.* (2007). "Generation of a finite element model of the thoracolumbar spine." Acta Bioengineering and Biomechanics **9**(1): 35-46.
- Uffen, M. P., M. R. Krijnen, *et al.* (2008). "Tissue identification with micro-magnetic resonance imaging in a caprine spinal fusion model." European Spine Journal **17**(8): 1006-1011.
- Urban, J. P. and S. Roberts (2003). "Degeneration of the intervertebral disc." Arthritis Research & Therapy **5**(3): 120-130.
- Urban, J. P. G., S. Roberts, *et al.* (2000). "The Nucleus of the Intervertebral Disc from Development to Degeneration." American Zoologist **40**(1): 53-061.
- Wills, B. P. D., R. A. Mohr, *et al.* (2007). "Current Status of Imaging of the Intervertebral Disc." Seminars in Spine Surgery **19**(2): 58-64.
- Wong, C., P. M. Gehrchen, *et al.* (2003). "Nonlinear finite-element analysis and biomechanical evaluation of the lumbar spine." IEEE Transactions on Medical Imaging **22**(6): 742-746.
- Zeng, G. L. (2010). Medical Image Reconstruction: A Conceptual Tutorial, Springer.
- Zhong, Z. C., S. H. Wei, *et al.* (2006). "Finite element analysis of the lumbar spine with a new cage using a topology optimization method." Medical Engineering & Physics **28**(1): 90-98.

# Appendix A

## A.1. Newton-Raphson Method

The Newton-Raphson method is based on the principle that if the initial trial solution of the root of non-linear function  $f(x) = 0$  is  $x_i$ , then if one draws the tangent to the curve at  $f(x_i)$ , the point  $x_{i+1}$  where the tangent crosses the  $x$ -axis is an improved estimate of the root (Figure A.1).

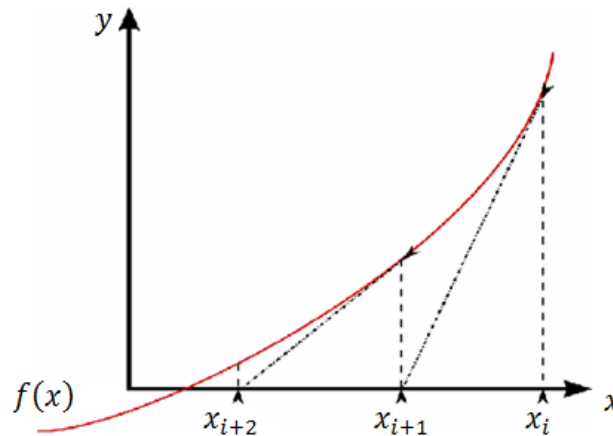


Figure A.1 - A geometric interpretation of the Newton-Raphson method.

Using the definition of the slope of a function, at  $x = x_i$

$$\begin{aligned} f'(x_i) &= \tan\theta \\ &= \frac{f(x_i) - 0}{x_i - x_{i+1}} \end{aligned} \tag{A.1}$$

One is able to determine a new approximation for the root of the function, given by

$$x_{i+1} = x_i - \frac{f(x_i)}{f'(x_i)} \tag{A.2}$$

Equation (A.2) is called the Newton-Raphson formula for solving nonlinear equations of the form  $f(x) = 0$ . So starting with an initial trial solution of  $x_i$ , one can obtain a new trial solution,  $x_{i+1}$ , by using Equation (A.1). One can iteratively repeat this process until one finds the root within

a desirable tolerance. However, the Newton-Raphson method can also be derived from Taylor series. For a general function  $f(x)$ , the Taylor series is

$$f(x) = f(x_i) + f'(x)|_{x_i}(x - x_i) + \frac{f''(x)|_{x_i}}{2!} (x - x_i)^2 + \dots \quad (\text{A.3})$$

As an approximation, taking only the first two terms of the right hand side,

$$f(x) \approx f(x_i) + f'(x)|_{x_i}(x - x_i) \quad (\text{A.4})$$

and if we are seeking the point where  $f(x) = 0$  we suppose that,

$$f(x) = 0 \quad (\text{A.5})$$

$$0 \approx f(x_i) + f'(x)|_{x_i}(x - x_i) \quad (\text{A.6})$$

one can arrive to an expression similar to (A.2):

$$x = x_i - \frac{f(x_i)}{f'(x)} \quad (\text{A.7})$$

In this study, the function  $f(x)$  is defined as  $\mathbf{R}(\xi, \eta, \zeta)$ , given that one has three unknowns:

$$\mathbf{R}(\xi, \eta, \zeta) = \mathbf{x} - \mathbf{x}\mathbf{n}(\xi, \eta, \zeta) = \mathbf{0} \quad (\text{A.8})$$

the Taylor series is

$$\mathbf{R}(\xi_{n+1}, \eta_{n+1}, \zeta_{n+1}) \approx \mathbf{R}(\xi_n, \eta_n, \zeta_n) + \left. \frac{\partial \mathbf{R}(\xi, \eta, \zeta)}{\partial(\xi, \eta, \zeta)} \right|_{(\xi_n, \eta_n, \zeta_n)} \Delta(\xi, \eta, \zeta) \quad (\text{A.9})$$

As

$$\Delta(\xi, \eta, \zeta) = (\xi_{n+1}, \eta_{n+1}, \zeta_{n+1}) - (\xi_n, \eta_n, \zeta_n) \quad (\text{A.10})$$

and if we assume,

$$\mathbf{R}(\xi_{n+1}, \eta_{n+1}, \zeta_{n+1}) = \mathbf{0} \quad (\text{A.11})$$

$$\mathbf{R}(\xi_n, \eta_n, \zeta_n) + \left. \frac{\partial \mathbf{R}(\xi, \eta, \zeta)}{\partial(\xi, \eta, \zeta)} \right|_{(\xi_n, \eta_n, \zeta_n)} [(\xi_{n+1}, \eta_{n+1}, \zeta_{n+1}) - (\xi_n, \eta_n, \zeta_n)] = \mathbf{0} \quad (\text{A.12})$$



$$\left. \frac{\partial \mathbf{R}(\xi, \eta, \zeta)}{\partial(\xi, \eta, \zeta)} \right|_{(\xi_n, \eta_n, \zeta_n)} [(\xi_{n+1}, \eta_{n+1}, \zeta_{n+1}) - (\xi_n, \eta_n, \zeta_n)] = -\mathbf{R}(\xi_n, \eta_n, \zeta_n) \quad (\text{A.13})$$

$$(\xi_{n+1}, \eta_{n+1}, \zeta_{n+1}) - (\xi_n, \eta_n, \zeta_n) = - \left[ \left. \frac{\partial \mathbf{R}(\xi, \eta, \zeta)}{\partial(\xi, \eta, \zeta)} \right|_{(\xi_n, \eta_n, \zeta_n)} \right]^{-1} \mathbf{R}(\xi_n, \eta_n, \zeta_n) \quad (\text{A.14})$$

which gives

$$(\xi_{n+1}, \eta_{n+1}, \zeta_{n+1}) = (\xi_n, \eta_n, \zeta_n) - \left[ \left. \frac{\partial \mathbf{R}(\xi, \eta, \zeta)}{\partial(\xi, \eta, \zeta)} \right|_{(\xi_n, \eta_n, \zeta_n)} \right]^{-1} \mathbf{R}(\xi_n, \eta_n, \zeta_n) \quad (\text{A.15})$$

Here,  $(\xi_n, \eta_n, \zeta_n)$  is the current trial solution,  $\mathbf{R}(\xi_n, \eta_n, \zeta_n)$  represents the value of the function at  $(\xi_n, \eta_n, \zeta_n)$ , and  $\left. \frac{\partial \mathbf{R}(\xi, \eta, \zeta)}{\partial(\xi, \eta, \zeta)} \right|_{(\xi_n, \eta_n, \zeta_n)}$  is the derivative (slope) at calculated  $(\xi_n, \eta_n, \zeta_n)$ .

$(\xi_{n+1}, \eta_{n+1}, \zeta_{n+1})$  represents the trial solution for the next iteration that it is required.